OCS Study
MMS 2006-050

Simulation of a Subsurface Oil Spill by a Marine Hydrocarbon Seep

Final Technical Summary

Final Study Report

MMS
U.S. Department of the Interior
Minerals Management Service
Pacific OCS Region

OCS Study
MMS 2006-050

Simulation of a Subsurface Oil Spill by a Marine Hydrocarbon Seep

Final Technical Summary

Final Study Report

Authors

Ira Leifer
Jordan Clark
Bruce Luyendyk
Principal Investigators

Prepared under MMS Cooperative
Agreement No. 14-35-01-00-CA-31063
by
Coastal Marine Institute
Marine Science Institute
University of California
Santa Barbara, CA 93106-6150

U.S. Department of the Interior
Minerals Management Service
Pacific OCS Region

Camarillo
September 2006

Disclaimer

This report has been reviewed by the Pacific Outer Continental Shelf Region, Minerals Management Service, U.S. Department of the Interior and approved for publication. The opinions, findings, conclusions, or recommendations in this report are those of the author, and do not necessarily reflect the views and policies of the Minerals Management Service. Mention of trade names or commercial products does not constitute an endorsement or recommendation for use. This report has not been edited for conformity with Minerals Management Service editorial standards.

Availability of Report

Extra copies of the report may be obtained from:

U.S. Dept. of the Interior
Minerals Management Service
Pacific OCS Region
770 Paseo Camarillo
Camarillo, CA 93010
Phone: 805-389-7621

A PDF file of this report is available at:
http://www.coastalresearchcenter.ucsb.edu/CMI/

Suggested Citation

The suggested citation for this report is:

Leifer, I., J. Clark, and B. Luyendyk. Simulation of a Subsurface Oil Spill by a Marine Hydrocarbon Seep. MMS OCS Study 2006-050. Coastal Research Center, Marine Science Institute, University of California, Santa Barbara, California. MMS Cooperative Agreement Number 14-35-01-00-CA-31063. 81 pages.

Table of Contents

Figures

Tables

FINAL TECHNICAL SUMMARY

STUDY TITLE: Simulation of a Subsurface Oil Spill by a Marine Hydrocarbon Seep

REPORT TITLE: Simulation of a Subsurface Oil Spill by a Marine Hydrocarbon Seep

CONTRACT NUMBER(S): 14-35-01-00-CA-31063; Task # 17611

SPONSORING REGION: Pacific

APPLICABLE PLANNING AREAS: Southern California

FISCAL YEAR(S) OF PROJECT FUNDING: FY 00/01

COMPLETION DATE OF REPORT: September 2006

COST(S): FY 00/01 - $110,935; FY 01/02 - no cost

CUMULATIVE PROJECT COST: $110,935

PROJECT MANAGER: Russell J. Schmitt

AFFILIATION: University of California, Santa Barbara

ADDRESS: Coastal Research Center, Marine Science Institute, University of California, Santa Barbara, CA 93106-6150

PRINCIPAL INVESTIGATORS: [1]Ira Leifer, [2]Jordan Clark, and [3]Bruce Luyendyk

ADDRESSES: [1]Marine Science Institute, University of California, Santa Barbara, CA 93106-6150; [2]Ecology, Evolution, and Marine Biology, University of California, Santa Barbara, CA 93106-9610, [3]Institute for Crustal Studies, University of California, Santa Barbara, CA 93106

KEY WORDS: hydrocarbon seeps, oil spills, buoyant oil and gas flow, bubble plume, Coal Oil Point Seep Field, surfacing location, dissolved methane

OBJECTIVES: To understand the roll of gas bubbles and gas bubble plumes in transporting oil from the seabed to the seasurface, thereby improving predictions of the fate (i.e., surfacing location) of oil (and gas) from an underwater pipeline leak

SIGNIFICANT CONCLUSIONS: Several discoveries resulted from this project. The bubble plumes from seeps were found to modify their environment by raising the dissolved methane levels in the water and creating upwelling flows. These enhance bubble survival and thus decreases the vertical distance they can transport oil, minimizing its surfacing footprint. Bubble distributions from natural seeps were measured (first ever) and were either broad distributions, or narrow and about 2000-3000 µm radius. Oil was found to form small gassy droplets in both cases, although the mechanism was different. It was also discovered that the trajectories of the gassy oil droplets were different from the oily bubbles.

STUDY PRODUCTS:

Publications:

Boles, J.R., J.F. Clark, I. Leifer, and L. Washburn. 2001. Temporal variation in natural methane seep rate due to tides, Coal Oil Point area, California. *J. Geophys. Res.* **106C11**, 27077-27086.

Leifer, I., and J. Clark. 2002. Modeling trace gases in hydrocarbon seep bubbles. Application to marine hydrocarbon seeps in the Santa Barbara Channel, *Russian Geology and Geophysics* {Original - *Geologiya I Geofizika*} **43(7)**: 613-621.

Leifer, I., J. Clark, and R. Chen. 2000. Modifications of the local environment by a natural marine hydrocarbon seep, *Geophys. Res. Lett.* **27(22)**: 3711-3714.

Leifer, I., G. De Leeuw, and L.H. Cohen. 2003. Optical measurement of bubbles: System, design and application. *J. Atm. Ocean. Tech.* **20(9)**: 1317-1332.

Leifer, I., and A.G. Judd. 2002. Oceanic methane layers: A bubble deposition mechanism from marine hydrocarbon seepage. *Terra Nova* **16**: 471-425.

Leifer, I., and I. MacDonald. 2003. Dynamics of the gas flux from shallow gas hydrate deposits: Interaction between oily hydrate bubbles and the oceanic environment. *Earth Plan. Sci. Lett.* **210(3/4)**: 411-424.

Leifer I., and R. Patro. 2002. The bubble mechanism for transport of methane from the shallow sea bed to the surface: A review and sensitivity study. *Cont. Shelf Res.* **22**: 2409-2428.

MacDonald, I.R., I. Leifer, R. Sassen, P. Stine, R. Mitchell, and N. Guinasso Jr., 2002. Transfer of hydrocarbons from natural seeps to the water column and atmosphere, *Geofluids* **2**: 95-107.

Roy, L.A., S. Steinert, S.M. Bay, D. Greenstein, Y. Sapozhnikova, O. Bawardi, I. Leifer, and D. Schlenk, 2003. Biochemical effects of petroleum exposure in hornyhead turbot (*Pleuronichthys verticalis*) exposed to a gradient of sediments collected from a natural petroleum seep in CA, USA. *Aquatic Toxicology* **65(2)**: 159-169.

Presentations:

Conferences and Workshops

Bergmann, S., M. LaMontagne, I. Leifer, and P. Holden. Assessment of the effect of marine oil seeps on sediment bacterial diversity and community structure by PCR-TRFLP. *American Society of Microbiologists General Meeting*, Salt Lake City, Utah, May 19-23, 2002.

Leifer, I., Bubble transport to the sea surface of seep methane. *USGS Workshop on Naturally Occurring Fossil Methane Seepage as a Factor in Global Climate Change*, Portland, Oregon, May 2-4, 2001.

Leifer, I., J. Boles, J. Clark, P. Holden, M. LaMontagne, B. Luyendyk, C. Olman, and L. Washburn. Predicting the fate of oil in the marine environment from the seabed to surface oil slicks and beyond. *California and the World Oceans '02*, Santa Barbara, CA, Oct. 27-30, 2002.

Leifer, I., J. Clark, B. Chen, L. Washburn, B. Luyendyk, and T. Egland. Observations of gas bubbles from the Coal Oil Point marine hydrocarbon seeps in the Santa Barbara Channel. *Shallow Gas Group 6th International Conference, Gas in Marine Sediments*, St. Petersburg, Russia, Sept. 5-9, 2000.

Leifer, I., J. Clark, and B. Luyendyk. From the Seabed to the Sea Surface: Measurments and implications of hydrocarbon seepage in the Santa Barbara Channel (abstract), AAPG HEDBERG CONFERENCE "Near-Surface Hydrocarbon Migration: Mechanisms and Seepage Rates" April 7-10, 2002, Vancouver, BC, Canada, Search and Discovery, Article #90006, 2002.

Leifer I., and A. Judd. Seep bubble layer deposition due to sharp bubble dissolution. *XI European Union of Geosciences*, Strasbourg, France, 8-12, April, 2001.

Lorenson, T., W. Ussler III, J. Dougherty, C. Paull, S. Mitra, R. Keaten, K. Kvenvolden, and I. Leifer. Dissolved methane concentrations adjacent to natural oil and gas seeps off Pt. Conception, California. *AGU San Francisco*, 8-11 Dec. 2002.

Seminars

1. MMS Camarillo, CA, May 16, 2002. Marine hydrocarbon seeps: A natural laboratory for studying processes related to petroleum exploration, spill mitigation, and ecological adaptation
2. Woods Hole Oceanographic Institute, Woods Hole, MA. Sep. 2002. The contribution to marine hydrocarbon seepage from catastrophic seepage events.
3. Venoco Inc., Carpenteria, CA. Aug. 2002. The Shane Seep blowout and our understanding of the role of marine hydrocarbon seeps to the global environment
4. California State Lands Commission, Long Beach, CA. Oct. 2001. The unique environment of marine hydrocarbon seeps.

Educational Products:

1) Narrated Video - Surveying Shane Seep, 16 minutes
2) www.bubbleology.com website most recently receiving 14500 hits per month (see www.bubbleology.com/stats) presents some of the research including allowing manuscripts to be downloaded.

FINAL STUDY REPORT

I. INTRODUCTION

I-1. Project Goals

The project "Simulation of a sub-surface oil spill by a marine hydrocarbon seep" proposed to understand by in-situ measurements the mechanism by which oil travels from a source at the sea floor to the sea surface. Currently, numerical models of the behavior of the buoyant oil and gas flow arising from a leak must make numerous untested assumptions. To address these shortcomings, field studies were undertaken to identify areas of uncertainty and improve our understanding of this process.

Motivation for this study arises from the fact that oil and gas typically are emitted together both at seeps or from an underwater spill, since the two phases are actually part of a spectrum stretching from the lightest hydrocarbon, methane, to much larger n-alkanes, and other oil components (too numerous to list, many unidentified). And when emitted together, the (surface active) oil travels on bubble surfaces, thereby rising much faster than if traveling as oil droplets. As a result, the bubble's buoyancy changes the oil's fate and its surfacing footprint is greatly reduced.

Thus the primary justification for this research is that improved prediction of surfacing location of an underwater oil spill means better preparedness with regards to positioning oil spill cleanup equipment. And as oil exploration moves to deeper and deeper waters, the importance of better understanding bubble, bubble plume, and oily bubble processes becomes of increasing importance.

To address these issues, we undertook to measure the fluid dynamics, gas chemistry, and bubble distributions of an active area of seepage in the Coal Oil Point Seep Field. The Seep Field is located just a few kilometers from the UCSB campus, and is one of the better characterized seep fields in the world, and among the largest in magnitude. Within the seep field, a very active and diver accessible seep was chosen to provide greater flexibility in the measurements and more rapid turn-around in the development of techniques. Since diver accessible seeps are by their nature shallow, measurements were also performed in the Gulf of Mexico (in Collaboration with Texas A&M) at seepage from a hydrate mound in water 550 m deep. These observations showed numerous similarities with processes at the shallower seeps.

I-2. Methodological Approach

The project goal was to understand the fate of oil and gas escaping from the seabed from natural seeps to understand better the underlying processes, which are shared with an undersea oil spill. The starting point was numerical sensitivity studies (Leifer and Patro, 2002) which indicated a sensitivity to many parameters that were largely, or completely unknown in the literature, and for which measurement techniques had not been developed or described in the literature. Thus our basic approach was to develop techniques for measuring the parameters needed to initialize and run a numerical model, and also to improve the numerical model to consider new data on new processes necessary for successful simulations.

I-3. Summary of Accomplishments

An advantage of embarking upon a project to do what has not been done before is that success often engenders numerous discoveries of great interest to the community, including many that unanticipated. A highlight of some of the most interesting discoveries and accomplishments:

1. Discovery that strong upwelling flows do exist in marine hydrocarbon seep bubble streams both in the Santa Barbara Channel (Leifer *et al.*, 2000a) and the Gulf of Mexico (Leifer and MacDonald, 2003).

2. Discovery that the fluid in marine hydrocarbon seep bubble streams becomes enhanced or even saturated with gas (Leifer *et al.*, 2000).

3. Confirmation of numerical study predictions (Leifer and Patro, 2002) that dissolved gas concentrations and upwelling flows are important to the fate of the bubbles, increasing bubble survivability and thus the flux of hydrocarbons to the sea-surface (Leifer *et al.*, 2000a).

4. Confirmation that the bubble transport mechanism is critical to predicting the surfacing footprint of a hydrocarbon seep, which is enormously smaller and closer to the location of the seepage than if the oil rises as a pure oil droplet (Leifer and Boles, 2005a).

5. Discovery that oil coating on bubbles enhances bubble survivability and thus the transport of hydrocarbons to the sea surface (MacDonald and Leifer, 2002).

6. Discovery that the seep system is extremely dynamic with ejections and “blowouts” occurring frequently. These events make seeps an even better natural laboratory for studying undersea oil spill processes (Leifer *et al.*, 2004).

7. Discovery that the bubble distribution of hydrocarbon seeps (in the SB Channel and the Gulf of Mexico) are primarily of bubbles larger than 2-mm diameter, and that smaller bubbles (to 0.5 mm diameter) are produced by vents with bubble tearing and breakup, but do not contribute appreciably towards the total mass transfer. Also, the first published bubble distributions for a marine hydrocarbon seep (Leifer and MacDonald, 2003).

8. Discovery that bubble gas composition fractionates (Leifer and Clark, 2003; Clark et al., 2003) as the bubbles rise, as predicted by Leifer and Patro (2002).

9. Discovery that optical bubble measurements (and measurements calibrated with optical means) during the last century have a bias due to off-axis rays (Leifer *et al.*, 2003a).

10. Discovery that bubble dissolution can lead to the formation of methane layers (Leifer and Judd, 2002). These layers have the potential to trap (temporarily) oil transported on bubble surface from either a seep, or an undersea oil spill.

11. First quantitative observations of "catastrophic seepage" including plume processes during which emissions increase enormously. Numerical studies showed that during catastrophic seepage virtually all of the methane reaches the atmosphere (Leifer *et al.*, 2005b)

12. Development (and first use) of an air pollution plume monitoring approach to studying seep emissions (Leifer *et al.*, 2005b).

13. First field-validated bubble plume model of seepage (Leifer and Clark, 2002).

14. Production of educational video ("Surveying Shane Seep") on the importance of these processes to the fate of seeps, and the impact on natural fauna and flora that interact and with the seeps. Conservatively, the video has been seen by thousands of viewers.

15. Maintenance of the www.bubbleology.com website that disseminates seep and bubble process information, publications, and various movie clips. The website currently receives circa 17,000 hits per month from circa 1000 unique users in circa 50 countries (see www.bubbleology.com/stats). Due to www.bubbleology.com, roughly 3 specific requests are received per month for advice/help on bubble and seep research in diverse countries (many developing). Several have led to long-term collaborations.

I-4. Study Area

Studies were conducted in the Coal Oil Point (COP) Seep Field, located a few kilometers from the University of California, Santa Barbara in the Santa Barbara Channel, offshore California. The COP Seep Field is one of the largest known areas of active marine seepage in the world, and arguably the best studied. Seepage spans a wide range of magnitudes and oil to gas ratios. Furthermore, much of the seepage is diver accessible. All these features make it an *ideal natural laboratory* for the study of hydrocarbon processes in the ocean.

I-4-1. Coal Oil Point Seep Field

The COP Seep Field is shown in Figure I-1. Several studies have quantified seep area (e.g., Allen et al. 1970; Fischer and Stevenson 1973; Fischer 1978) and emission fluxes (e.g., Hornafius *et al*. 1999; Quigley *et al*. 1999; Clark *et al*. 2000) using sonar techniques, ocean geochemistry, and direct gas capture. Fischer and Stevenson (1973) noted changes in hydrocarbon seeps on decadal time scales in the field with significant decrease in seepage area between 1946 and 1973. On the basis of on a comparison of sonar data and oil company seep maps, they attributed this drop to offshore production. During the last seven years, the UCSB seep group has mapped the seeps in the area using sonar images and quantified seepage flux from sonar and direct gas capture using a flux buoy (Washburn *et al*. 2001). Results indicate that ~1.5 x 10^5 m^3 dy^{-1} (4.5 x 10^{10} g yr^{-1}) of seep gas is emitted to the atmosphere from ~3 km^2 of sea floor (Hornafius *et al.* 1999) with roughly an equal amount dissolved into the coastal ocean (Clark *et al.* 2000). The seeps also release about 80 barrels dy^{-1} - 5x10^6 liters yr^{-1} (Clester *et al.* 1996) with oil slicks a common channel feature (Leifer *et al.* 2005b) and it has been noted that oil emissions vary with tides (Mikolaj and Ampaya 1973).

Seep locations are controlled by anticlines and lie along three depth trends. The inner trend is ~20-m deep and includes Shane Seep and IV Super Seep. A second trend at ~ 40 m deep includes the Horseshoe seeps and COP Seeps. The deepest trend (~70 m depth) includes the La Goleta Seeps and Seep Tent Seeps as well as Platform Holly.

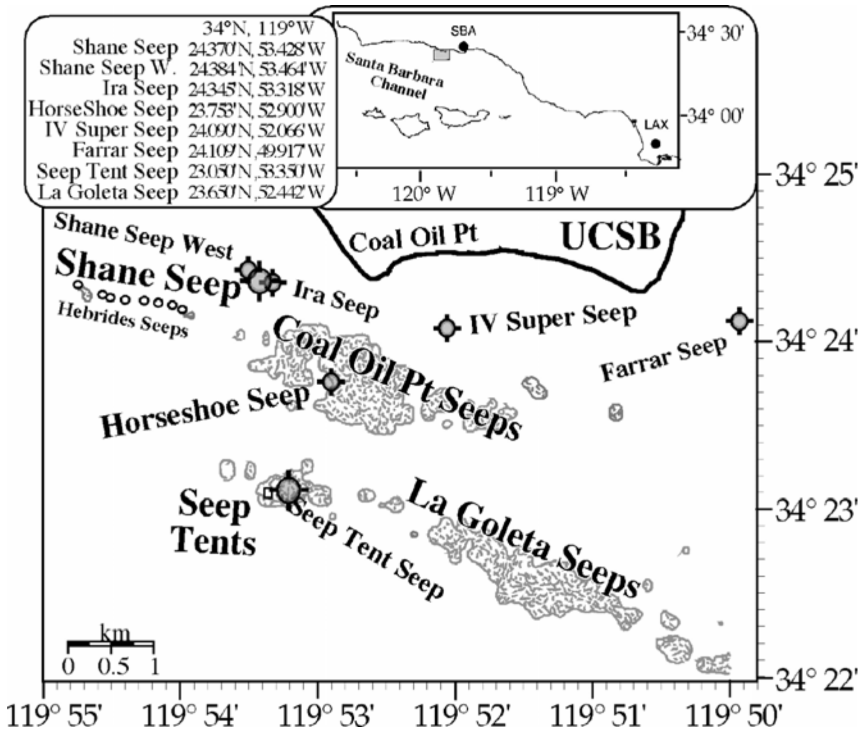

	34°N, 119°W
Shane Seep	24.370'N, 53.428'W
Shane Seep W.	24.384'N, 53.464'W
Ira Seep	24.345'N, 53.318'W
HorseShoe Seep	23.753'N, 52.900'W
IV Super Seep	24.090'N, 52.066'W
Farrar Seep	24.109'N, 49.917'W
Seep Tent Seep	23.050'N, 53.350'W
La Goleta Seep	23.650'N, 52.442'W

Figure I-1. The Coal Oil Point Seep Field, Santa Barbara Channel off the coast of Santa Barbara, California. Upper panel shows the overall channel including the Santa Barbara and Los Angeles airports. Gray areas in lower panel indicate regions of high bubble density as indicated by sonar returns (Hornafius *et al.* 1999). Inshore seeps i.e., (Shane Seep, Ira Seep, IV Super Seep, and Farrar Seep) were too shallow for the sonar survey. Seep names are informal and GPS coordinates locations are provided on figure. Table coordinates referenced to 34° N, 119° W.

I-4-2. Shane Seep Area

One of the most intense seep areas in the COP Seep Field is in Shane Seep (34° 24.37' N, 119° 53.41' W), located in 22 m deep water – i.e., diver accessible. For example, Washburn *et al.* (2004) recorded the highest single flux measurement for the COP Seep Field at Shane Seep. Seabed surveys, described in detail below showed that seepage at Shane Seep consisted of numerous (order 10^3-10^4) small vents that emit streams of similarly sized bubbles rising in lines over an area approximately 30 m by 20 m. (600 m2). These *minor vents* surround hydrocarbon volcanoes (the number has changed over the years) with one or more *major vents*. The volcanoes are termed hydrocarbon because they consist primarily of tar and sand. Minor vents produce bubbles that are nearly mono-disperse in size, while major vents produce a broad size spectrum of bubbles. Major vents also have significantly greater gas flux minor vents.

Bubbles rise in several intense plumes to the sea surface, each plume corresponding to a hydrocarbon volcano. These bubble plumes drive strong upwards water flows, called the upwelling flow. The strong upwelling flow generates strong outward flows at the surface. Bubbles burst at the surface, leaving very fine slicks that the outwelling flow rapidly advects. Furthermore, the flow is unsteady, both pulsing and shifting spatially. The central plumes are surrounded by a much wider and more diffuse bubble plume. Surveys over the years have also shown significant changes in seabed morphology.

For all these aspects, our approach has been to intensively study Shane Seep and its interaction with the environment, although other seeps in the field have been investigated.

II. METHODOLOGY

II-1. Seabed Morphology

Most of the research studies were conducted at Shane Seep, one of the most active, and concentrated seep areas in the seep field. In the process of studying seepage phenomena at Shane Seep, we documented numerous changes in magnitude, extent, and seabed features within the seep. The most active vents were located within hydrocarbon volcanoes several meters across, which were documented to vary spatially over the years of the study. Furthermore, these changes appeared associated with large, transient gas emissions, and are proposed related to tar flux (Leifer and Boles, 2005a).

To understand the transient seep behavior, and its effects on seabed morphology (or alternatively, how to infer the dynamic nature of seep emissions based on seabed morphology) a project of seabed mapping was undertaken, described in Leifer *et al.* (2004).

For the last three years, (2000-2003), SCUBA divers have periodically visited Shane Seep (34° 24.37’ N, 119° 53.41’ W) in the Coal Oil Point (COP) Seep Field and conducted both video surveys and measurement surveys to document the changes in seabed morphology with time. Measurement surveys were done with a fiberglass meter tape. Since Shane Seep is in an area of otherwise unremarkable sandy seabed, North-South and East-West steel-link transect cables (2.5 cm links, 60 feet long) were laid down late October, 2001. Previously, sand anchors and yellow transect lines were used; however, they often disappeared between surveys, possibly due to dragging boat anchors and/or fishermen’s nets. The transect was centered on a position 3.5 meters WNW of two prominent hydrocarbon volcanoes. The volcanoes are termed hydrocarbon (HC) volcanoes to denote that the volcano walls are a combination of tar and sand rather than mud (La Montagne *et al*. 2004). Every meter along the chain, 30-centimeter lengths of yellow, polypropylene rope were tied at one end to the chain. Polypropylene rope is buoyant and the free ends remained visible even in places where the chain became buried. A

250-kg mooring anchor was placed at the intersection of the transect chains and connected by line to a spar buoy ~2 m above the seabed. The line continued to the sea surface and a small buoy. Each HC volcano had an associated major vent, and one meter lengths of rebar were hammered halfway into the sediment nearby. Closed cell foam numbers, 15-cm high, were pushed onto the rebar and secured above and below by plastic wire ties. At the four cardinal points and 4 intermediate directions (i.e., NE) at a distance of 10 m from the transect center, rebars also were hammered into the sediment. Wire ties were attached, with ends sticking out at the rebar top and held in place by expanded polypropylene rope. A code was used, where counterclockwise from North, 1, 2, 3, and 4 plastic cable ties were used, with and additional half length plastic cable ties to indicate intermediate directions (i.e., 1 and 1/2 for NE). Video surveys were conducted along circular lines at a given radius from the center. This was accomplished by having the videographer hold one end of a tape measure, while a second diver held the other end at the mooring point. The videographer maintained the video camera at a constant angle and zoom (wide-angle) setting. Divers also used tape measures to measure precisely the distance to the main morphological features, including their height above the sea floor, wall height and caldera width.

II-2. Seep Bubble Measurements

For the purposes of predicting the fate of gas bubbles, and hence oil transported by gas bubbles, the bubble size distribution is critical, small bubbles tend to dissolve, while large bubbles may be able to reach the surface with most of their original gas content. Bubble rise speed, and the strength of the upwelling flow also are size dependent, as is the amount of carried on the bubbles. As a result, the fate of the oil arrives depends upon the bubble size. Thus one of the main tasks of this research was to measure the bubble distribution, of particular importance since seep bubble distributions were entirely absent in the literature. To do so, we developed a bubble measurement system optimized for marine seeps.

II-2-1. Overview of Bubble Measurement Systems

The following summary is from Leifer *et al.* (2003b), written during this project. This section summarizes the various methods used to measure bubbles for bubbles generated from breaking waves at the water surface. Since this research project produced the first quantitative measurements of the bubble distribution from hydrocarbon seeps, design of the bubble measurement system was based on system considerations from measurements of bubbles from breaking waves at the sea-surface. Design considerations specific for seep bubbles from Leifer and MacDonald (2003) are also presented.

Breaking-wave bubble measurement systems – Design Considerations

Different approaches have been used to measure bubbles, from acoustics to optical (laser and video/photo). Each technique has advantages and disadvantages, and is effective over different size ranges and bubble density regimes. Laser techniques are non-invasive and use a laser beam that has its illumination blocked when a bubble crosses the narrow measurement volume (Hwang *et al.* 1990), or multiple beams whose intersection defines the measurement volume and the bubble size is determined by its interaction with the laser interference pattern (Baldy and Bourguel 1987; Asher and Farley 1995). Laser systems have problems when multiple bubbles enter the beam(s), ie., high bubble density results in coincidence, and with large ($r >$ 1000 µm, where r is radius) bubbles whose mean shape is ellipsoidal but variable due to shape oscillations. The shape of large bubbles may cause aliasing wherein large bubbles are sized as smaller bubbles (Asher and Farley 1995). Since bubble concentration typically decreases with r^{-2} to r^{-4}, (e.g., Haines and Johnson 1995), aliasing only significantly (under) biases large bubble concentrations. Acoustic approaches include resonance, pulse propagation, or multifrequency backscatter. Acoustic methods have high rejection of non-bubble particles, e.g., 10^{-9} for acoustic resonators (Vagle and Farmer 1998), and can non-invasively map large regions of the water column, allowing investigations into bubble plume distributions (Thorpe 1982; Medwin and Breitz 1989). However, acoustical methods have difficulties, in common with laser methods, with non-spherical (i.e., $r > 500$ µm in a turbulence flow, where r is radius) bubbles and at high bubble concentrations. Optical methods (photographic and video) are able to measure at high bubble densities and over a wide r range including very large bubbles (the optics determines the size range). Optical approaches use either a constrained measurement volume (e.g., Monahan *et al*. 1994; Wang and Monahan 1994), or an unconfined measurement volume (Walsh and Mulhearn 1987; Haines and Johnson 1995; Johnson and Cook, 1979; Jähne and Geiβler 1994; Deane and Stokes 1999). Optical systems are generally invasive since for clarity in turbid water, or for high bubble concentrations, the measurement volume must be near the system's viewing port. However, invasive systems may significantly disturb the bubbly flow.

Bubbles are typically backlit, although side and front lighting (discussed below) have been used. The collected images are analyzed and the number (or probability) of bubbles of each size class determined. The bubble concentration distribution, based on the measurement volume, can be calculated from the probability distribution. The measurement volume for constrained systems varies only with the effect of bubbles touching the image edge (i.e., a large bubble must be further from the edge than a small one to avoid its images being partially cut). In contrast, one of the major disadvantages of an unconstrained optical BMS is the difficulty in determining their measurement volume, since the depth of field varies with bubble size, optics, and the analysis method. Furthermore, the measurement volume may vary with illumination and water clarity.

In unconstrained systems, apparent bubble size varies with analysis technique (e.g., the threshold level, image preprocessing, etc.) and distance to the bubble unless telecentric lenses are used (only feasible for longer focal lengths and thus higher magnification). Johnson and Cooke (1979) used three forward pointing strobes. Bubbles were "in focus" when the three spots did not overlap, and the measurement volume was a simple function of r up to the large r limit of ~300 µm. Walsh and Mulhearn (1987) used a similar approach and found that the spot location on the bubble is complicated by optical effects due to refraction and reflection on the curved bubble surface, and estimated a sizing error of ~10%. Haines and Johnson (1995) side illuminated bubbles in a 5-cm thick slab. For bubbles in this slab, the size error was determined by moving a bubble attached to a wire along the camera axis, and was found to be ~10% across the 5 cm slab for a $r = 250$-µm bubble.

Constrained systems also may have the problem of evolution of the size distribution between entry into the device and reaching the measurement volume since bubble rise velocity increases with r. If this distance is short, segregation is negligible. An extreme example is a bubble tube where bubbles enter and rise through a clear tube above the water surface for imaging. The entry distribution can be calculated using the bubble rise velocity (Bowyer 1992).

Seep Bubble Measurement Systems - Design considerations

The intent of bubble visualization was to record a video sequence showing the bubbles next to a calibrated scale of known size and to provide sufficient illumination to distinctly render each bubble (i.e., no motion blur) in the individual video frames. Bubble visualization requires the depth of field to be sufficient to maintain good focus for bubbles in the plume. However, bubble-sizing errors can become significant if the bubble plume occupies too large a cross-section of the camera's depth of field because the accuracy of size estimation depends upon distance between the size reference and the measured bubble. For broad plumes, baffles can be used to block off all the bubbles outside of a slab. Imaging a bubble with distinct edges requires a shutter speed sufficiently fast to freeze bubble motion. For auto-iris video cameras, this requires sufficient illumination to force the shutter speed. Three illumination schemes were attempted in the present observations. With front illumination, the principal light sources were quartz flood lamps mounted in the same plane as the camera. For side illumination, a collimated light source was placed perpendicular to the camera's point of view and immediately adjacent to the bubble plume. For back illumination, lamps placed behind the camera plane were reflected back into the bubbles by a white panel placed immediately behind the bubble plume.

Of the three illumination techniques, the auto-iris shutter speed of the video camera was too slow (due to insufficient illumination) and bubbles appear as streaks. Back illumination provided the best results, with in-focus bubbles showing as dark outlines with bright centers. With back illumination, the white panel had markings to indicate size scale. Side illumination with the collimated light source provided images that were the most difficult to analyze. Bubbles appeared as half moons with the dark side edge extremely difficult to distinguish, and required hand analysis. Although for spherical bubbles it was easy to estimate the far edge, for the irregular shapes of most of the larger seep bubbles, this was difficult, thereby increasing the sizing uncertainty. Bolts on the collimated light source were used for size scale. Front illumination provided two difficulties, it was almost impossible to determine if a bubble was in focus, and secondly, bubble edges were less distinct. Size comparison for bubbles that initially were front-illuminated, and then back-illuminated (by rising above the panel top) showed that front illumination underestimated bubble size. Front illumination worked best with a black background.

II-2-2. Seep Bubble Measurement System

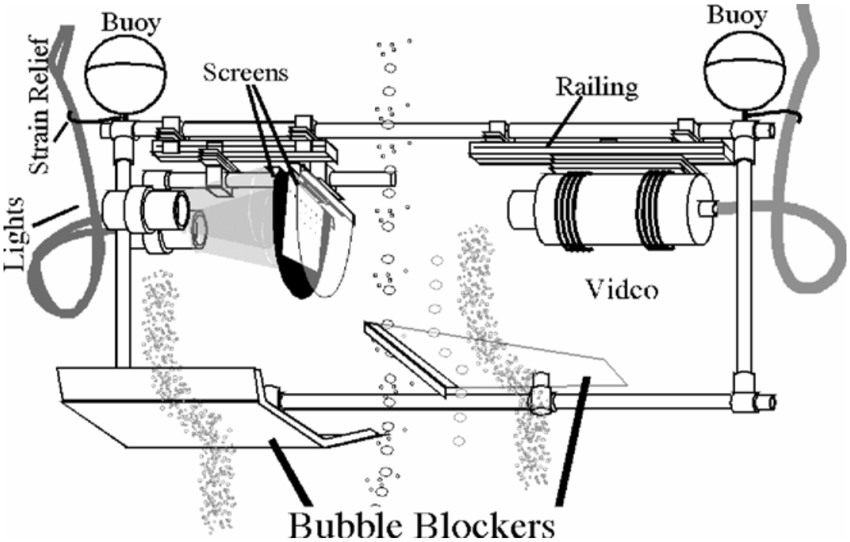

Figure II-1. Schematic of video-based, Bubble Measurement System (BMS), open configuration.

Bubble measurement systems and analysis approaches are reviewed in Leifer *et al.* (2003b). The video-BMS has several key components, shown schematically in Figure II-1 and in underwater images in Figure II-2. Bubbles are backlit by two 300-W, wide dispersion, underwater lights (ML3010**,** DeepSea Power and Light, CA), shining on a translucent screen. The back of the measurement volume is defined by a clear screen mounted in front of the translucent screen which has a series of size scale markings at the bottom of the video camera's field of view. Backlighting causes each bubble to appear, ideally, as a dark ring surrounded by a central bright spot, allowing, at least in principle, computer analysis, whereas side-lighting produces half moons that require manual outlining (Leifer and MacDonald, 2003). When a bubble is too close to the backlighting screen, off-axis rays obscure the bubble's edges, decreasing contrast and biasing bubble size towards a potentially significant underestimate (Leifer *et al.*, 2003a).

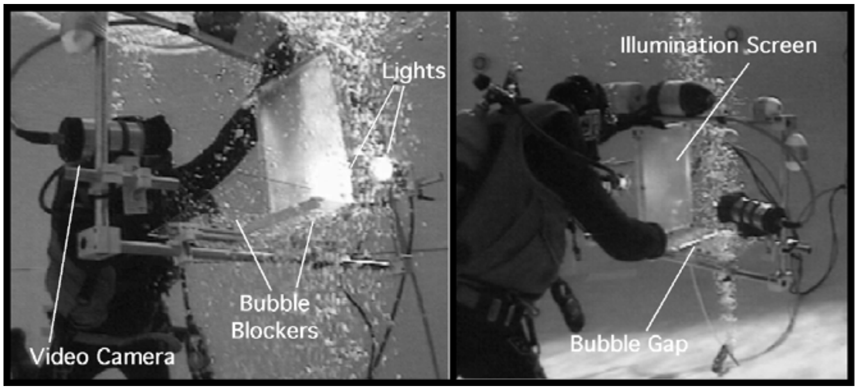

Figure II-2. Pool test of the seep Bubble Measurement System in open configuration.

To ensure the bubbles are at a known distance, where the resolution can be related to the screen scale markings, bubble blockers are positioned underneath the spaces between the camera and the measurement volume and between the lights and the clear screen. Parallax errors are minimized (and can be calibrated for) with long focal length - i.e., high zoom - settings. The underwater video camera (SuperCam 6500, DeepSea Power and Light, CA) allows complete remote control, including most importantly shutter speed, which is set high enough to prevent bubble blurring. All components are mounted on aluminum optical railing and/or tubing for easy repositioning. Teflon-lined railing sleds are locked into place with bolts tapped into the sleds. All bolts are graphite particle lubricated to prevent seizing after recovery. Light and video cables are secured to the frame (and boat) with strain reliefs. The whole system is slightly negatively buoyant, with the buoys maintaining a vertical orientation. Cables and a buoy line are taped together into a neutrally buoyant cable bundle. Video is recorded by an onboard Mini-digital video (DV) video recorder (Sony Video Walkman, Sony, Japan) and displayed on a flat screen monitor. A diver communication system maintains contact with the SCUBA equipped diver positioning the BMS, although it can also be mounted on a remotely operated vehicle (ROV). Either a custom-built camera controller (Speed Vision, CA) or a laptop controls the camera settings.

Video clips are acquired directly by Firewire (IEEE-1594) at 60 *fields* per second at full digital video DV resolution (720 x 240 pixels) and analyzed using routines written in NIH Image (NIH Image 2000). The routines (see Leifer *et al.* 2003b; Leifer and MacDonald 2003) extract the fields to 60 *frames* per second, remove background intensity variations, and remove pixelation noise. Images are thresholded and all bubbles analyzed in each frame. For each bubble, the position, major and minor axes, angle, and area are recorded as well as the frame number. From the major (r_a) and minor (r_b) axes, the equivalent spherical radius is calculated (Sam *et al.*, 1996)

$$r = (r_a r_a r_b)^{1/3} \tag{1}$$

Statistically significant fractions of the bubbles are tracked between frames to determine the velocity function, V(r). The measurement series are analyzed further with Matlab scripts (Mathworks, MA). Sequences associated with tracked bubble are identified and the mean trajectory angle calculated with a least-squares, linear-regression analysis. A polynomial, least-squares, linear-regression analysis of all tracked bubbles is used to calculate V(r), which includes the effects of buoyant rise, turbulence, and bubble-induced upwelling flows. All bubbles are r and time, t, segregated and then histogrammed. The histogram segregation bin widths are chosen so a statistically significant number of bubbles are counted in bins near the distribution peaks. Size bins are spaced logarithmically. Normalization of the histogram by the radius increment and depth interval yields the bubble size layer population distribution, Ψ, which is the total number of bubbles in each size class per meter of depth. Ψ is what sonar observes and can be combined with V(r) to calculate the bubble size emission population distribution, Φ. In this way, multiple counting of bubbles as they rise across the field of view is accounted for. If the bubble stream is larger than the blockers, the population is scaled to the entire stream based on overview video, or the blockers can be repositioned. Finally, distributions are fit with a least-squares, linear regression analysis over selected r by a function of the form:

$$\Phi(r,t) = k(t)r^{-S(t)} \tag{2}$$

where F is Φ or Ψ, k is a constant, and S is a power law exponent. The fit is performed on

$$\log(F) = -S \log(r) + \log(k) \qquad (3)$$

For surface measurements, the BMS is reconfigured in a closed mode, shown in Figure II-3. Measuring bubbles at the sea surface is more challenging than at the seabed for several reasons. For computer identification, the bubble need to be back illuminated, thus at the sea surface, the lights are competing with sunlight. Thus the primary goal of the closed configuration is to block out the sunlight. Currents at the sea surface can be large (to 1 m/s are common), and these currents have a tendency to move bubbles rapidly towards the camera, or cause highly turbulent fluid flows around the screen, preventing accurate measurement of the vertical velocity (for flux calculations). As bubbles get closer to the camera, their apparent size increases, while as they move towards the illumination screen their contrast with the background decreases, sometimes to the point of invisibility. Thus, a second function of the closed BMS is to isolate the fluid in the measurement volume from motions associated with currents or motions of the boat.

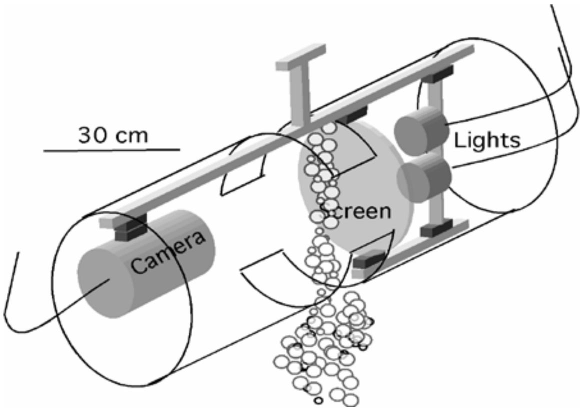

Figure II-3. Schematic of closed seep Bubble Measurement System (BMS).

The BMS design allows quick conversion between open and closed orientation. The major components of the bubble measurement system (camera, lights, and screen) are mounted on sleds that slide on optical rails. These sleds are held in place by bolts tapped through the sleds that are tightened to lock the sled in place. The components can be slid out from the open BMS framework and slid onto a railing in the closed BMS framework, which is a heavy (7-mm walls) 30-cm diameter PVC tube with a gas for bubbles to enter. Buoys are attached to the BMS system to maintain the orientation and keep the BMS approximately 30 cm below the sea surface (if too shallow, the BMS will form bubbles at the sea surface). Two PVC pipes are attached to the BMS to maintain orientation, and the cables are connected to strain reliefs. The closed system also has a clear screen at the camera side of the measurement volume that fits very tightly to the walls, preventing any water motions along the BMS axis.

II-2-3. Bubble Measurement System Calibration – Blurring

Given sufficient illumination, current video cameras allow selection of shutter speeds sufficiently fast to prevent bubble blurring. However, if illumination is limited, a choice must be made between aperture size (i.e., depth of field) and shutter speed (blurring). The decision depends upon the bubble distribution and bubble dynamics of interest. For example, in a constrained system, the DOF need only be the distance between windows, while in an unconstrained system, where the goal is visualization of bubble plumes; a large DOF may be required. The effect of bubble blurring depends upon the bubble's velocity (pixels per second) and size (pixels). While in the laboratory, it is easy to design a BMS with sufficient illumination; at sea (shipboard or submersible/ROV, etc.) power may be a limiting factor. Furthermore, the illumination required depends upon the size of the FOV. For example, a small FOV is required to study small bubbles, and thus light easily can be focused to evenly and intensely illuminate the small FOV. In contrast, a large FOV requires significantly more illumination power.

Blurring smears the bubble image but the result may be complex. For blurring of ~1 pixel or less, blurring can increase sharpness. Consider a bubble whose edge is half in two pixels. Smearing the bubble in one direction can place more of the edge in one pixel, creating a sharper edge. Alternatively, if the edge is almost entirely in one bubble, blurring spreads the intensity across two pixels, decreasing sharpness.

Also, since blurring occurs along only one direction, blurring affects only one axis. Examples are shown in Figures II-4a and II-4d for a 670-µm bubble. These two images were taken for shutter speeds of 1/20,000 s and 1/500 s, respectively. Furthermore, since bubble motion is on average - due to buoyancy - vertical, blurring occurs mostly along the minor rather than the major axis (Equation 1). Additional complexities arise in the relationship between blurring and apparent size since non-blurred bubbles exhibit intensity gradients at their edges (e.g., Figure II-4b) and bubble size is determined by thresholding. Finally, to determine an acceptable level of blurring, blurring induced errors should be compared with other errors and natural variability.

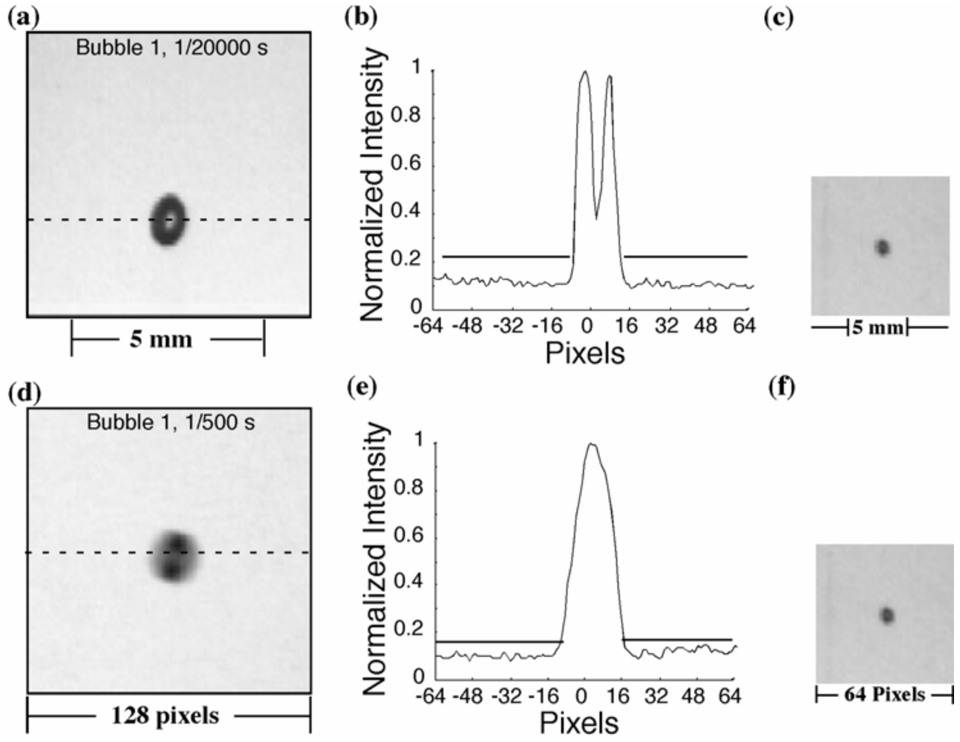

Figure II-4. Images of bubbles of 670 µm bubbles for 1/20000 s (a) and 1/500 s (b) shutter speeds. Intensity profiles (c,d) for (a,b), respectively for dashed lines in (a,b). Also shown are 670 µm bubbles at lower magnification for 1/10000 (c) and 1/500 s (f) shutter speeds. Size scales located under images.

To understand the effect of bubble blurring upon apparent bubble size, a series of bubble-blur calibration experiments were conducted in a glass tank at the University of California, Santa Barbara. A schematic is shown in Figure II-5. A regulated airflow was fed through one of two drawn capillary tubes to generate single bubble streams of bubbles (Leifer *et al.*, 2000b). Bubbles were imaged with a high speed video camera (Kodak, Ektapro, 1000 FPS) for shutter speeds ranging from 1/60 to 1/20000 s. Backlighting was provided by a 1000 W spotlight with 2° dispersion illuminating a translucent plastic screen located behind the tank. Illumination was controlled by a variac and varied to allow consistent background intensity for an aperture of F8, except at the fastest shutter speeds ($\leq$ 1/10000 s) where the aperture was F5.6. A 55-mm telecentric lens (Computar, Japan) was used, thereby minimizing errors due to uncertainty in the distance to the bubble. From the highest shutter speeds, capillaries one and two produced r = 670 and 2240-µm bubbles, respectively. Bubble sizes were consistent during each run. Image sequences were digitized at a resolution of 720 X 480 pixels, cubic spline interpolated to double resolution and thresholded 10 intensity units above the local background (determined by a 10 pixel wide ring around each bubble). Major and minor axes (and angle) were determined from a least squares fit of an ellipse to the bubble outline.

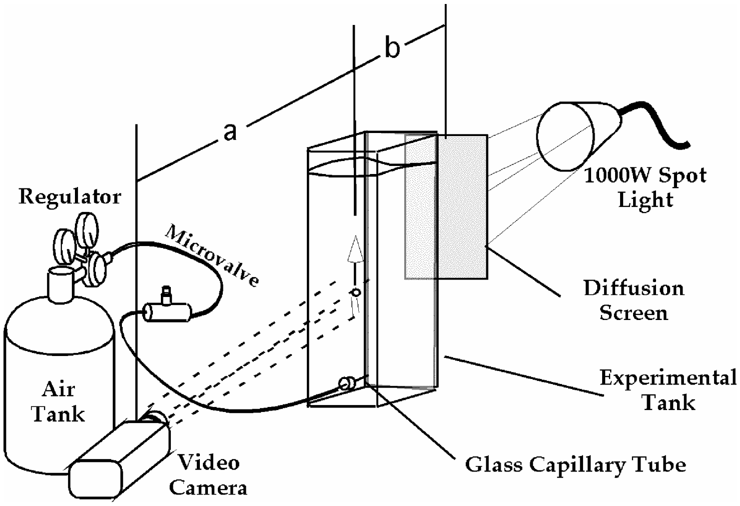

Figure II-5. Schematic of bubble blur calibration experiment.

For the three runs, the measured bubble radii versus shutter speeds are shown in Figure II-6. Errors bars are one standard deviation. For 670-µm radius bubbles and the narrow field of view (Run #1), blurring has negligible effect for shutter speeds greater than 1/1000 s (6.2 pixels blur, ~ 50% of *r*). At slower shutter speeds, the error grows rapidly. For the same bubbles but with a wide field of view (Run #2) bubbles were ~5 pixels in radius and thus sizing errors are larger. In fact, the size overestimate in Run #2 is ~1 pixel. The lower resolution decreases the effect of blurring with increasing shutter speed, only becoming significant for speeds of 1/250 s where the blur is ~7 pixels (140%). For the larger, 2240 mm oscillating bubble (Run #3), several effects combined to make bubble blurring less significant. The greater size (in pixels), slower velocity, and greater eccentricity decrease the error due to blurring, particularly with respect to the greater uncertainty in bubble size due to oscillations.

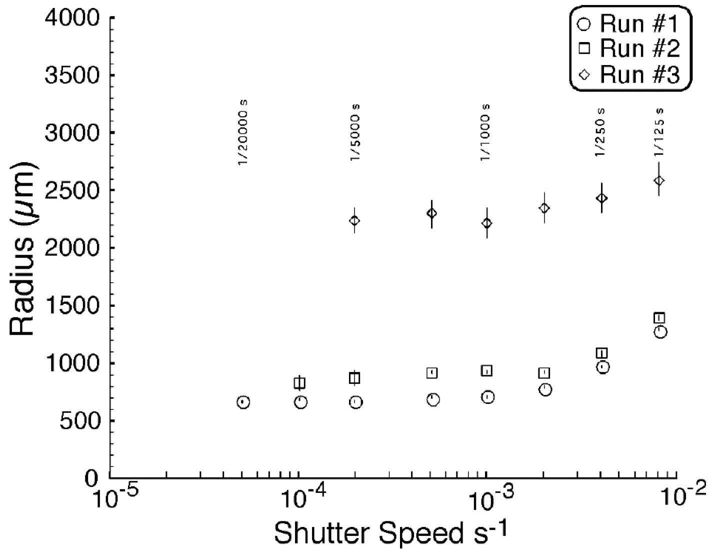

Figure II-6. Bubble radius versus shutter speed for experimental runs showing increase in apparent bubble size due to blurring. Run 2 is for the same bubble as Run #1, but with a wider field of view.

In summary, bubble blurring of less than a pixel is always negligible; however, greater bubble blurring is typically tolerable, particularly for bubbles large enough to show a white central spot (~10 pixels). For bubbles smaller than 10 pixels, bubble blurring is generally less important compared to errors associated with pixilation.

II-2-4. Bubble Measurement System Calibration – Off-axis Rays

While performing some highly accurate measurements of bubble hydrodynamics (Leifer *et al*. 2000b), the authors were forced to address potential error sources, including: *Where is the actual as opposed to apparent bubble edge?* This question partially arises from the fact that the edge of a bubble image is not a step function in intensity and as a result, different intensity threshold levels yield different bubble sizes. Thus, determination of the appropriate threshold level is critical to correctly measure bubble size. Calibration experiments were conducted with respect to bubble size was measured both optically and non-optically using the displaced mass method, reported in (Leifer *et al.*, 2003b). A stream of bubbles was optically imaged with a video system and counted by their disruption of a laser beam. The bubbles also were collected and the bubble-displaced water "weighed." In the displaced mass method, a balance outside the tank is connected by a lever arm balanced on a knife-edge to a sealed, inverted, funnel in the tank. As water is displaced from the funnel, buoyancy decreases the downward pull from the funnel, causing an increase in mass on the balance. Using a balance allows measurement of much smaller displaced volumes without the uncertainty of the precise location of the meniscus and thus the displaced volume. From the gas volume and the number of bubbles, the size can be calculated, thereby allowing a non-optical calibration of bubble size. The experimental set-up is shown in Figure II-7 below.

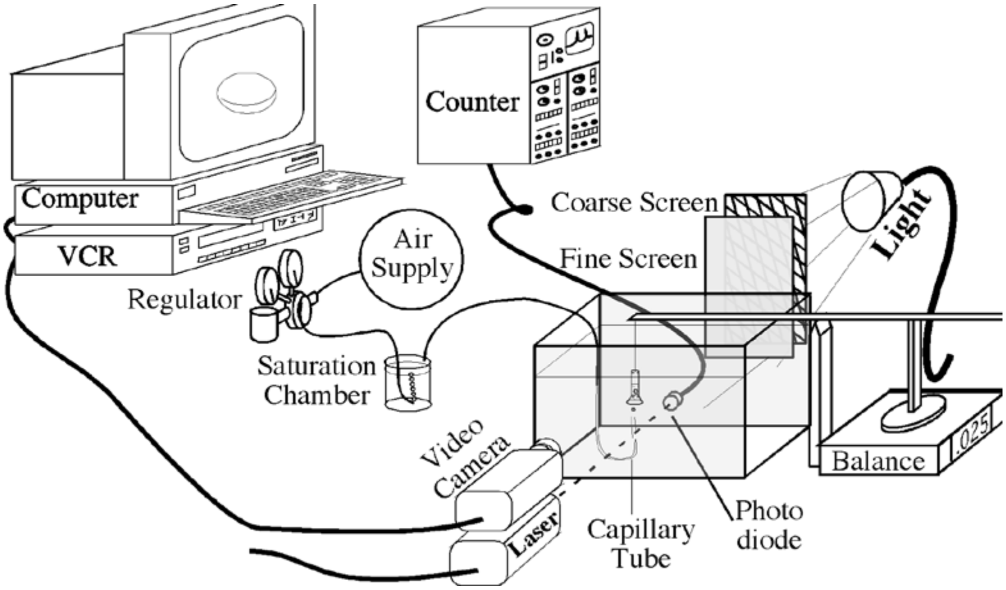

Figure II-7. Schematic of experimental set-up.

The air supply was regulated to provide a constant stream of bubbles. Water vapor can cause bubble size to rapidly grow after release. To prevent this, the air was presaturated. Bubble size can also change due to gas (air) exchange with the water. Thus, the tank was vigorously bubbled with large bubbles prior to each experiment to ensure that the tank water was close to equilibrium with air. For the bubbles studied, since the surface tension force (La Place pressure) was negligible, (Leifer and Patro, 2002) the dissolved air in the tank water should be in equilibrium with atmospheric plus 1/2 the hydrostatic pressure for the tank water height.

The equivalent spherical bubble radius, i.e., the radius the bubble would have if it was a sphere, was calculated using two different approaches. The displaced-mass effective bubble radius, r_M, was calculated by using the collected gas volume, calculated from the measured mass, M, and the water density, ρ, and the volume of a sphere, and is:

$$r_M = \left(\frac{3M/\rho}{4\pi N}\right)^{1/3} \tag{4}$$

where N is the number of bubbles counted, ρ was calculated from a polynomial fit to tabulated values of ρ from the CRC (1995; p. F-5) as described in Leifer *et al*. (2000). The collected volume was corrected for the difference in hydrostatic pressure between the depth of the collection funnel and the imaging depth. Since r depends upon the threshold intensity, the background intensity local to the bubble was determined, and images were thresholded 10, 15, 20, and 25 units above (darker) than the local background intensity. Image intensity varies between 0 and 255 and was adjusted so that the images spanned most of this range. The local background rather than the overall intensity background was used because of intensity variations across the images which although small (typically < 10) were a potential error source. The local background was determined from the median intensity in a 10 pixel wide ring surrounding each bubble.

An example bubble image is shown in Figure II-8. For this experiment, r_M = 748 μm from a bubble mass of 7.87 x10^{-5} g water displaced per bubble. The halo ring surrounds the bubble in Figure II-8a, was ~3 pixels wide, and appears as a ring-like depression surrounding the bubble in the surface plot shown in Figure II-8b.

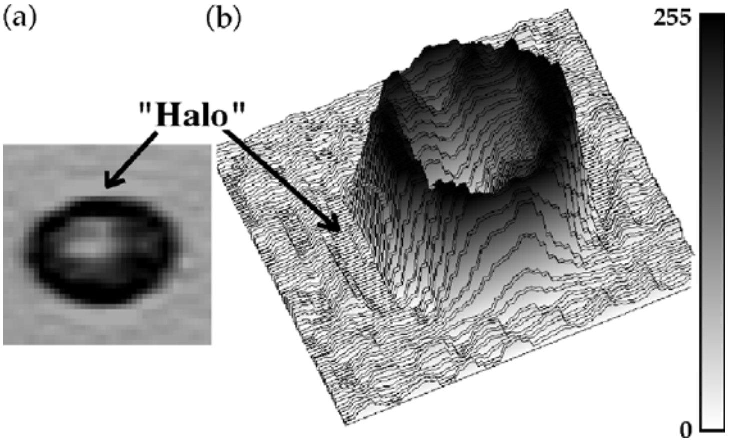

Figure II-8. Enlarged bubble image (200%) (a) and surface intensity plot (b) of a 748-μm radius bubble with intensity scale.

A histogram of r_O for images thresholded 25 units above the background is shown in Figure II-9a. For this figure, a series of 1100 frames comprising ~800 bubbles was analyzed. The dominant peak represented an elliptical mode in the bubble shape oscillation, while the smaller peak represented a spherical mode. Both peaks were very narrow (half width ~5 µm) and separated by just 10 µm.

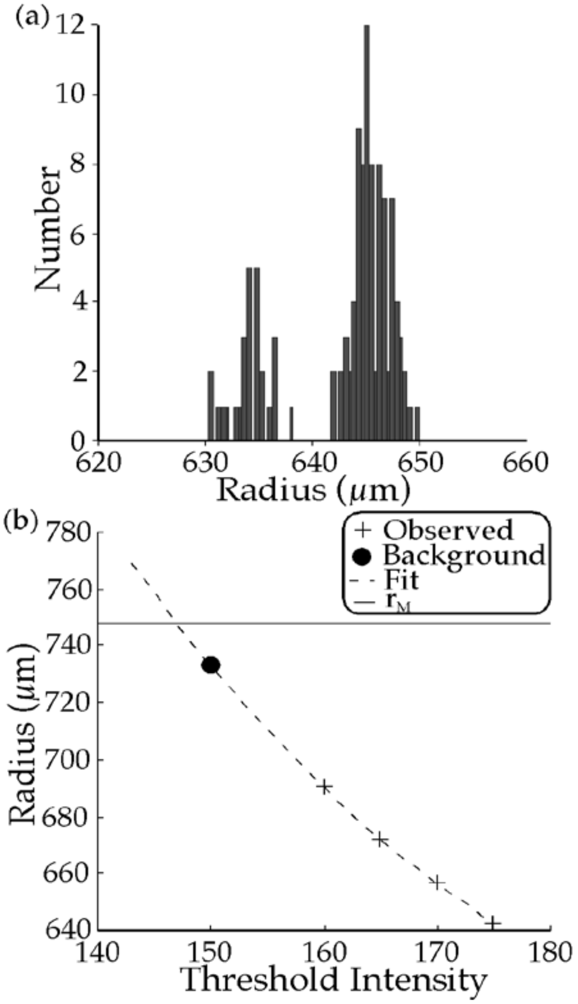

Figure II-9. Size histogram for bubbles in Figure II-8, thresholded 25 units above the local background intensity (a). Optically determined radius, r_O, versus threshold intensity (b). Also shown is a quadratic fit, r_O with extrapolation to background, and mass-derived radius, r_M. Data key on figure.

The median values for r_O at different intensities are shown in Figure II-9b and clearly show a decreasing trend in r_O with increasing threshold intensity. A quadratic curve of r_O with intensity was determined by a least-squares, linear-regression analysis, and is also shown in Figure II-9b. The extrapolation of this curve to the background intensity is shown by a circle. The horizontal dashed line shows the value of r_M. Thus, the actual bubble edge is at a threshold value of 147, i.e., below the background intensity. In fact, the bubble edge is hidden in the "halo" ring, which renders the method of bubble size determination by simple thresholding unrealistic or at best problematical. The size bias also varies depending upon the chosen threshold. For example, if thresholded just 5 intensity units above the background (implying good image quality) yields r too small by 5%.

Based on a series of simple experiments, it was concluded that the major uncertainty in bubble sizing was due to reflection. The “halo”, while important for explaining internal reflections does not produce an external bright ring. A similar experiment was conducted by Vigneault, Panneton & Raghavan (1992). In their experiment, bubbles were produced from a drawn capillary tube also supplied by a carefully regulated air supply. The value of r_O for a threshold slightly above the background was compared with the flow rate derived r. They showed very good agreement between the two methods. However, since they did not pre-saturate the air, they most likely underestimated the flow rate derived r due to bubble growth from water vapor (i.e., bubbles were larger by the time they rose to the level of the video camera, ~2%). They also did not correct for hydrostatic pressure. Had corrections for water vapor and hydrostatic pressure been made, they also would have found that the correct threshold was slightly below the local background intensity.

It was found that the shape of the backlighting screen determined the “halo” shape. Specifically, rotating a rectangular screen changed the orientation of the halo, suggesting that off-axis light rays were responsible. A schematic of the geometry is shown in Figure II-10, where radial symmetry about the camera axis was assumed for simplicity. For backlit bubbles, the screen required to provide even illumination is typically significantly larger than the bubble.

As a result, light emitted from above (or below) the bubble can be reflected off the front bubble face towards the camera, thereby appearing to originate at the bubble’s edge, obscuring the actual edge. The angles of interest are shallow enough that the bubble can be considered a perfectly reflecting sphere.

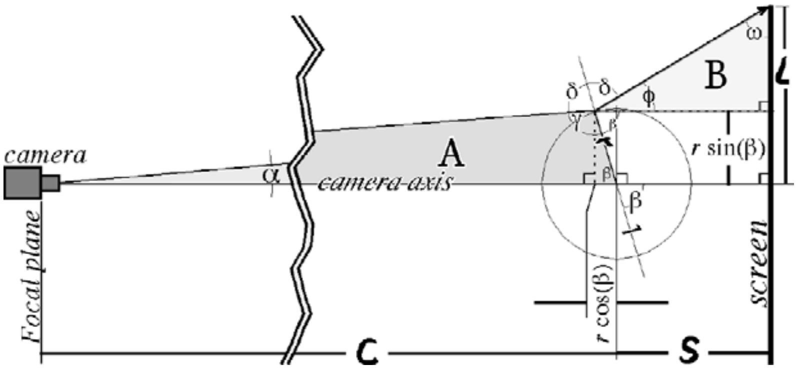

Figure II-10. Schematic of bubble edge halo-ring caused by off axis light reflections. Light source from back illuminated screen to the right. See text for details.

If the distance from the camera backplane to the bubble axis, C, and the distance from the bubble to the screen, S, are known, then for different angles within the camera’s field of view, the lighting screen location for origin of the reflected light, L, can be calculated and is:

$$L = r\sin(\beta) + \frac{S + r\cos(\beta)}{\tan(\alpha - 2\beta - \pi/2)} \tag{5}$$

with β given by

$$\beta = \pi - \sin^{-1}\{\frac{C}{r}\sin(\alpha)\}\,. \tag{6}$$

The derivation of (5) is found in Leifer *et al*. (2003b) Alternatively, for a specified screen radius, L_S, the fraction of the bubble image that is front illuminated (i.e., not dark) can be calculated.

A calculation of L using (5) is shown in Figure II-11 for $r = 10^{-3}$ m, $C = 1$ m over a range of S. Values of L are shown versus fraction of the maximum bubble angle, α_M, which for small angle is simply:

$$\alpha_M = \tan(r/C) \tag{7}$$

and for this case was 10^{-3} radians. For L_S=20 cm (dashed line) and S varying from 1.0 m to 0.1 m, the forward reflection calculation predicts a ring that appears from ~0.5% to ~15% from the bubble edge, respectively. Since α was small, L was largely insensitive to C or r, unless C was very small (on the order of a few centimeters).

For the experiment shown in Figure II-11, C, S, and L_S were ~75 cm, ~25 cm, and ~15 cm, respectively. Equation (5) predicts a radius fraction of ~4%, in general agreement with the observed ~2.5% difference between r_M and r_o for thresholding at the background. The discrepancy probably arises because the reflected intensity is added to the bubble intensity.

This simple model (Figure II-11) shows how off-axis rays can obscure the bubble edge, but the calculated bias assumes thresholding at the background. If a simple threshold is chosen to size the bubbles, then the bias will be greater, perhaps significantly, unless the illumination screen angle (ϕ) is small. When bubble distributions are strongly r dependent (e.g. oceanic bubble distributions vary as r^{-3} - (De Leeuw and Cohen, 1994; Dietz 1979), even small biases in r will produce large biases in parameters such as total bubble surface area and volume.

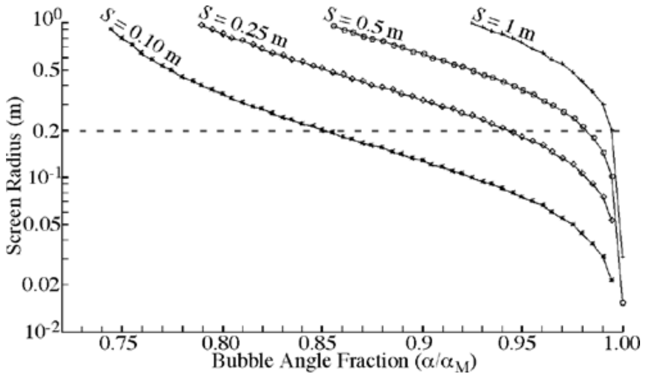

Figure II-11. Calculated screen distance of origin, L, versus fractional apparent bubble angle (α/α_M) for several screen distances, S. See text for details.

II-3. Methodology - Gas Geochemistry

Bubble dissolution depends upon the equivalent gas concentration difference between the bubble and the surrounding water. Thus for predicting the dissolution rate (gas outflow rate) of a bubble, the dissolved gas concentration in the bubble plume must be measured, as well as the partial pressure of the different gas components in the bubbles. Although methane, nitrogen, and oxygen are the most significant gases in the system, trace gas measurement are useful for model validation.

Dissolved gases were collected in glass syringes at the seabed and sea surface. To get the dissolved gas composition in the bubble stream, divers blocked the rising bubbles with their bodies by leaning backwards, and collected the samples from in front of their chests. Several approaches were used to collect bubble gas samples. In one method, Zip Lock bags were filled with gas and 50-ml glass syringes used to remove ~15 ml of gas (so that syringes would not overflow at the surface). Another method used evacuated Teflon bags connected to a funnel that were filled with seep gas, and finally, small BOD bottles were used, inverted over a small funnel placed over a bubble stream. In this method, the bottle was flushed with several volumes of gas before sealing with a septa cork, and crimping.

The Teflon bag method allows gas to be collected with minimal contact with water; however, it was only able to function where the flow of gas was large enough to “inflate” the bag, thus the preferred method for small seeps is the BOD bottles. However, this method was only implemented starting in 2003, and thus all data reported here is for either Teflon bag collection, or syringe extraction from Ziploc bag.

Water collection was using glass syringes. The syringes were held onto a flat piece of plastic which allowed water collection without removing the syringe from the plastic support plate. The plate was marked with the sample location (e.g., 10 m, 20 m, surface, etc.) and thus prevented confusion in where samples were collected. Syringes were drawn slowly so that there was no cavitation.

In the laboratory, gas samples were transferred directly to vacutainers in a container filled with argon. Gas in the water samples was extracted by the headspace method (Dietz 1979). Basically, the headspace gas, argon, was injected into the syringe and the syringe shaken to allow dissolved gas to reach equilibrium with gas in the headspace. Headspace gas is then transferred into vacutainers. Argon rather than nitrogen was used to allow GC determination of the nitrogen. Gas samples were analyzed using standard gas chromatography techniques at Zymax Forensics (San Luis Obispo, Ca).

II-4. Methodology – Fluid Motions

Numerical studies also show a strong sensitivity to the upwelling flow, the principle exploited by the turbine-seep tent to measure gas flux. This flow is important because bubbles are assumed entrained within the flow (Woolf and Thorpe 1991), rising at their buoyancy velocity, V_B, relative to the flow. Thus the upwelling flow reduces the transit time of the water column. Another effect is the upwelling of methane rich water (McDougal 1978; Leifer and Judd 2002).

Both effects increase the methane flux to the atmosphere. The upwelling flow was inferred from the BMS-derived V(r), but required assumptions about the bubble cleanliness and oiliness. Alternatively, dye tracer studies allow direct measurements of the upwelling flow. Fluorescein dye (commonly used in oceanographic studies and available from marine suppliers as rescue marker dye) was introduced into the bubble stream and the time to reach the surface measured. First, the dye was dissolved in seawater in a clear, 10-cm diameter plastic tube. The tube bottom was capped by a large rubber stopper held in place with an elastic cord, while the tube top has a sheet of aluminum foil held loosely in place by electrical tape and secured by another large rubber stopper. At the seabed and adjacent to a major vent, the diver removed the top and bottom stoppers while maintaining the tube in a vertical orientation. The tube was then moved laterally over the vent and the rising bubbles immediately popped off the loosely held aluminum foil, dragging the dye out of the tube. Before moving the tube over the bubble stream, the diver gave a countdown over the acoustic diver communication system to scientists onboard the boat who timed the dye arrival at the sea surface. Previous attempts to inject the dye into the stream from syringes, etc., often missed or significantly disturbed the bubble stream, resulting in a significant delay of several seconds before the dye was entrained in the upwelling flow.

III. RESULTS

III-1. Results - Seabed Morphology

When first visited in November 2000, Shane Seep was characterized by two East-West HC volcanoes sharing a center ridge, each ~3-m diameter and nearly circular. The location of the central ridge is shown as a dashed line in Figure III-1a, although precise measurements were not taken at the time. At the sea surface, there were two distinct plumes that formed two outwelling flows with a strong convergence zone between. Over the following three years numerous changes occurred (see Figure III-1) including the appearance of four new major volcanoes along an East-West line, while the original vents dwindled in importance. Although video surveys were conducted before November 2001, Figure III-1a shows results from the first survey with measuring tapes.

During 2000, the seabed morphology changed very little, until the appearance of volcano #3 during a three-week period (between two video surveys) in October 2001. Volcano #3 was discovered during a dive to place a chain link transect chain on the seabed (Figure III-1a). During this time period there was a (potentially coincidental) magnitude 2.4 earthquake at 10-km depth and within 500 m of Shane Seep, on October 17, 2000 at 2300, PST. However, given the absence of direct observations, a causal tectonic mechanism remains hypothetical. At this time, the walls of volcano #3 rose ~25 cm above the surrounding seabed and were extremely circular, centered on the main vent. Many large tar blocks (up to 1-m diameter and 30-cm high) were observed in its interior. Significant changes also were observed for volcanoes #1 and #2, whose walls were generally lower and their central dividing ridge completely gone. Volcano #2 was also deeper and larger. Two weeks later (Figure III-1B), all vents had increased in extents and wall heights, and volcano #3's caldera was rocky, although tar blocks were still observed. The location of vent #2 had shifted almost 1-meter North within its caldera.

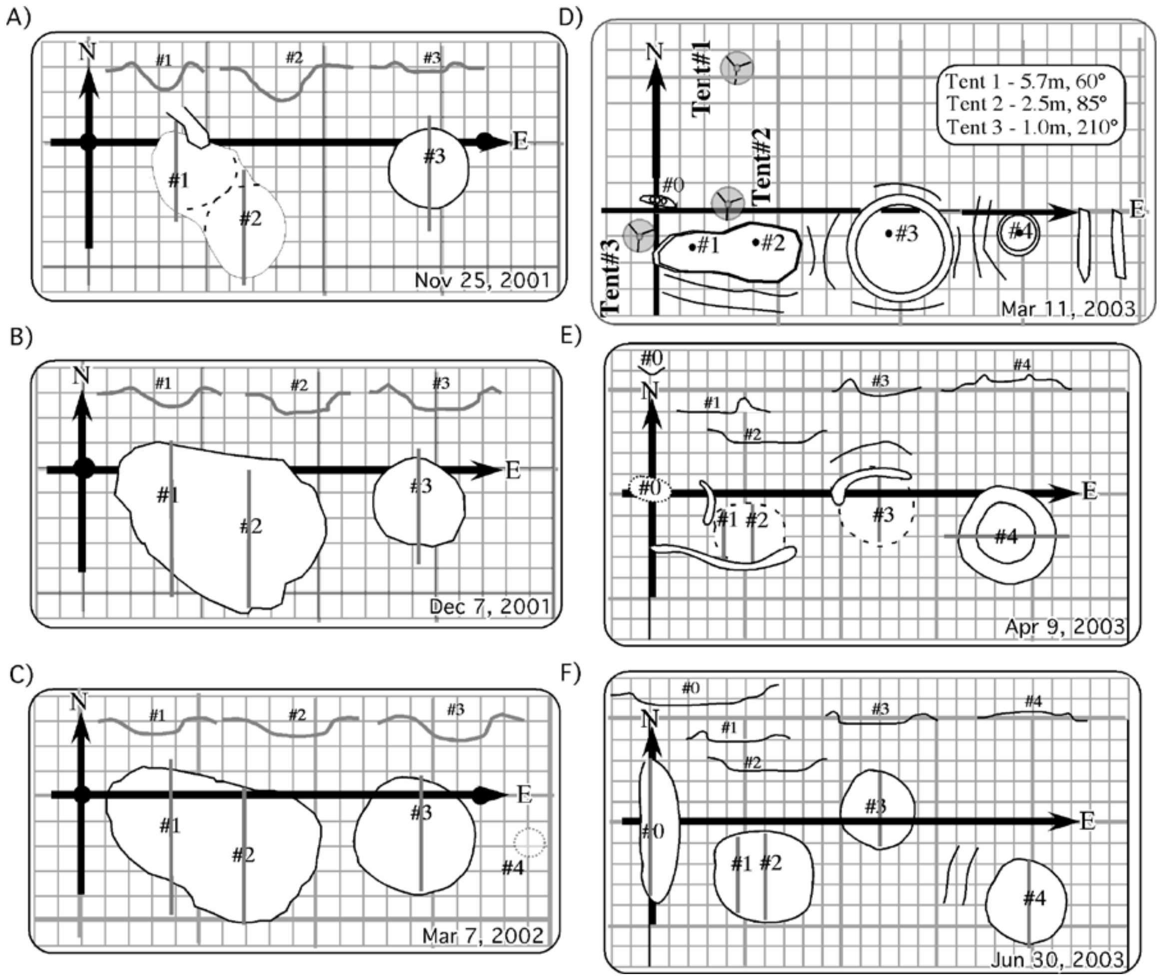

Figure III-1. Shane Seep seabed surveys from 2000-2003. Dates shown on panels, small grid is 1 meter, large grid is 5 meters. Profile vertical heights are to scale. and indicated by vertical lines. For each hydrocarbon (HC) volcano, vent numbers (#) show locations of main vents. Lines indicate direction of increasing slope towards HC volcanoes. Snake-like shapes are tar ridges. See text for details.

The next measurement survey was March 7, 2002 (Figure III-1C), and showed additional changes in seabed morphology. The extents of volcanoes #1 & #2 had decreased and the walls were shorter and less steep, possibly due to sand scouring by winter storms during the previous months. The walls of volcano #3 also were less steep, but its extent had increased significantly. Most significantly, the transect chain now disappeared into the walls of volcano #3, although not the other volcanoes. Beyond volcano #3 a circular mini-caldera, ~1-m wide and 2-cm high was videoed from which a few sporadic bubbles would appear from time to time (shown at approximate location by dotted circle in Figure III-1C). Its significance was not appreciated at the time, and thus measurements were not taken.

Almost a year passed before the next mapping survey in March 11, 2003, during which feature locations were mapped, but profiles were not measured. A new area of very active seepage had appeared during the previous two months near the mooring point (volcano #0), and the major vent locations had moved. Rebar stakes marking vents #1 and #2 were found toppled over and relocated to the new vent locations. The transect chain still penetrated the walls of volcano #3, which now was on a slightly raised plateau. Also, vent #4 had developed into a major feature. Vent #4 now contained many minor vents producing bubble streams (although no clear major vent) and was located on a roughly circular, raised plateau. Its walls were also higher and its caldera descended below the plateau level by a ~10 cm. Also noted in this survey were North-South aligned tar ridges about 1-m high and 5-m long further east than volcano #4. Minor vents were more common on top of the ridges than in the surrounding area. It is unclear when the ridges appeared as previous video and measurement surveys generally did not extend further than Vent #3. Note, on this dive visibility was a relatively clear 2.6 m, thus features a few meters beyond the survey extent easily could remain unobserved. Also shown on Figure III-1D are the locations where the turbine-seep tents were deployed. Significant changes were observed by the next survey, April 9, 2003 (Figure III-1E). In particular, sand had been deposited throughout Shane Seep and obscured (although they may also have been eroded) many of the features. The rebar stake for Vent #2 was found sticking 15 cm out of the sandy sediment, instead of the 50 cm when it was relocated during the previous survey mission. Volcano walls were largely gone, their previous location shown by dashed lines. In their place, ridges were observed, with the transect chain passed through the walls of both ridges in its path. These ridges may have been portions of the now buried volcano walls. However, where the South walls for volcanoes #1 and #2 wall had been, a 41-cm high ridge that extended to the N-S transect chain was observed. The south wall of #3 had disappeared, but the area North of the ridge was elevated above the seafloor to the East and West. In all previous surveys (video and mapping) this area was nearly flat. Furthermore, the major vent for #3 had moved ~3 meters east, with the observed ridge centered about this new main vent location. Vent #4 had grown significantly, was still circular, and now was centered almost two meters further west. Finally, an area of very active seepage had appeared at the mooring point, including a small depression (~30 cm from the video surveys). At the time it was unclear that this would develop into a major feature and precise measurements were not made.

In the most recent survey, June 30, 2003 (Figure III-1F), the dominant seepage feature was vent #0, which had become oblong. Its southern wall was two step, with a raised plateau ~20 cm wide, halfway up the wall. The location of vents #1 and #2 had shifted southward and emitted a fraction of the gas they had several years earlier. Volcano walls had reappeared, although partially this may be explained by the observation that the area no longer appeared buried in sand. Vent #3 had relocated north of the transect chain at the same distance from the mooring point, while vent #4 had moved further south and east. Volcano #4 still was raised relative to the surrounding seabed, but less so than before. However, the seabed now sloped upwards nearly a meter between volcanoes #3 and #4. Furthermore, the profile of volcano #4 had changed, it now resembled more a mound than an elevated volcano on a plateau. A final change observed but not measured was the appearance of volcano #5, not shown, ~3 m west of the mooring point. Divers estimated it was 0.75 m across and with walls than 5 cm tall, but very active in terms of gas emissions. Given the absence of walls, it is unlikely to have been in existence during previous surveys. It was discovered after it was noted that Shane Seep's sea-surface expression suggested five upwelling plumes, a feature not noted during previous visits to Shane Seep. Also, the total seepage at Shane Seep had increased significantly from previous surveys, the area of active seepage (defined as more than 3 or 4 vents m^{-2}), which previously had extended about 7-m from the East-West transect chain, now extended to almost 13 meters to the South. The area immediately surrounding volcano #3 also was far more active.

III-2. Seabed Morphology Significance

The seabed surveys demonstrate that seepage features at Shane Seep are both semi-permanent and “plastic.” The sediment overburden is Late Quaternary, and for the outer COP seep trends is thin, < 1 m. At Shane Seep, the overburden is thicker, 2-3 meters (Fischer 1978), consisting primarily of very fine sand, and has modern total organic carbon of 1 - 2% (Fischer 1978). The sand overlies fractured Monterey formation basement. The upper 30 cm of sand is cemented by tar (La Montagne *et al.* 2004) and highly cohesive. The seabed near Shane Seep is also heavily coated with bacterial mats, and large tar balls can be found within the hydrocarbon (HC) or tar volcanoes. These volcanoes are termed hydrocarbon volcanoes rather than mud volcanoes because of their high tar content, which provides the necessary cohesion to form the volcano walls, and fixed vent locations.

That the walls represent a depositional process was dramatically demonstrated by the burying of the transect chain after it was draped across the newly formed volcano #3. Since elsewhere the chain, even two years later, lay on top of the sandy bottom, only a depositional process could explain the manner that the chain disappeared into the caldera's walls. Furthermore, the appearance of stones in the bottom of volcano #3 suggests that not only tar, but also sand was lofted during these events, leaving behind the rocks.

There are several processes evidenced in the changes in seabed morphology over the years. These include deposition of tar from ejections along with the removal of seabed material during large ejection events, feature erosion and burial by storms, and the plastic deformation of the seabed. Vent locations remain fixed for a period of years but then re-express themselves nearby. While ejection events build up caldera walls they also destroy them. Together these changes provide strong evidence of the dynamic nature of hydrocarbon seeps.

During the formation of volcano #3, 100,000 kg of sediment was displaced. This most likely was due to either a single or a series of "explosive" events as indicated by highly circular caldera shape. And in general, when volcano walls grew higher, they also grew circularly (except for Vent #0). Meanwhile, much smaller ejections (but larger than that observed by the turbine tents) caught on video did not evidence any significant displacement of seabed sediment. Clearly the formation of volcano #3 was a large event (or series of events). The source of the event that precipitated the formation of volcano #3 could have occurred deep or shallow. If we assume shallow blockage responsible, it still must have been deep enough to stop the flow through both existing volcanoes #1 and #2. Otherwise pressure could not have built up behind them to then cause destruction of the ridge. Pressure behind the blockage would have increased until the blow through destroying the ridge separating the two vents. But this raises the question: How does an event that could destroy the ridge between volcanoes #1 and #2, despite their being highly active (i.e., open) vents, overcome the significantly greater resistance represented by the sediment displaced in the formation of volcano #3? Thus it is far more plausible that a deep event was responsible. In this case, a massive pulse of gas suddenly was released and traveled rapidly upwards through the fractures. At the seabed, the two existing vents were inadequate to flux the great volume of gas, and thus represented a bottle-neck behind which the pressure increased until it created a new pathway, volcano #3. The giant tar blocks found on volcano #3's caldera floor must have been squeezed out through the fractures immediately under volcano #3, since similar tar blocks were not found in volcanoes #1 and #2. It is unclear from the observations whether the deep event was the clearance of a blockage in the fracture system or sudden access to the fracture system by a previously unconnected gas reservoir.

Tar does not necessarily migrate in punctuated transient events, for example there are beach tar oozes and forms mounds at the south edge of the Carpinteria State Park, CA. This tar seep is a long-term feature, having been used in boat making by indigenous peoples for centuries or longer (Galloway 1998). Given sufficient pressure, tar migrates. And such pressure may explain the appearance of elevated seabed features such as the elevated plateau under volcano #4, or the ridges further to the east. Here, some of the fractures may be completely clogged with tar, implying an enormous pressure buildup to cause a blow through, which is unlikely (i.e., rare) to happen while gas can flow (and pressure be relieved) through other vents. In this case, the elevated pressure forces the tar to slowly ooze forwards, gradually lifting the sediment layer. Water flow may also be involved. And certainly the very gradual (over a year) formation of volcano #4 suggests a gradual process in sharp contrast to the sudden appearance of volcano #3.

The difference between volcanoes #3 and #4 was that volcano #4 formed gradually and included a raised mound. Not only did the plateau height gradually increase with time, but also the gas flux through the volcano #4's vents and the size and height of its caldera walls. When first identified, volcano #4 was only a few centimeters tall with a few bubble streams. By 2003, the caldera was meters across, the walls were half a meter high, and there were many active vents. This is consistent with the tar slowly being forced from the fractures during the initial stages until the gas flux was sufficiently great (i.e., fractures were sufficiently opened) to allow the blow through mechanism to begin depositing the caldera walls.

In fact, the decrease in relative flux, and then impermanence of volcano #3 seen after March 2003, may relate to a large tar and or fluid flow clogging the vent. This is supported by the lifted seabed North of volcano #3 observed in April 2003, prior to the volcano's relocation to this area. Similarly, the expansion of volcano #4 between April and June, 2003, was preceded by a large (50 cm) increase in plateau height, noted in March 2003.

The survey mapping showed that Shane Seep has undergone significant changes in seepage on a monthly time scale. Seabed changes were linked to large transient seepage events that are most probably related to tar blockage. These transient events must occur with some frequency, and thus demonstrate that not only do hydrocarbon seeps provide a model of a steady state leakage from an undersea pipeline or well, but that they also (transiently) provide an opportunity to study more violent leakage processes, such as blow outs.

III-3. Results - Bubble Observations

III-3-1. Seabed vent bubble observations

<u>Seep Vent Classification Scheme</u>

Within the active seepage area defined as Shane Seep, there are literally thousands of vents spanning a wide range of fluxes and distributions. Survey video suggests that vent bubble plumes can be classified into four categories, major, minor, elastic, and obstructed, examples of which are shown in Figure III-2.

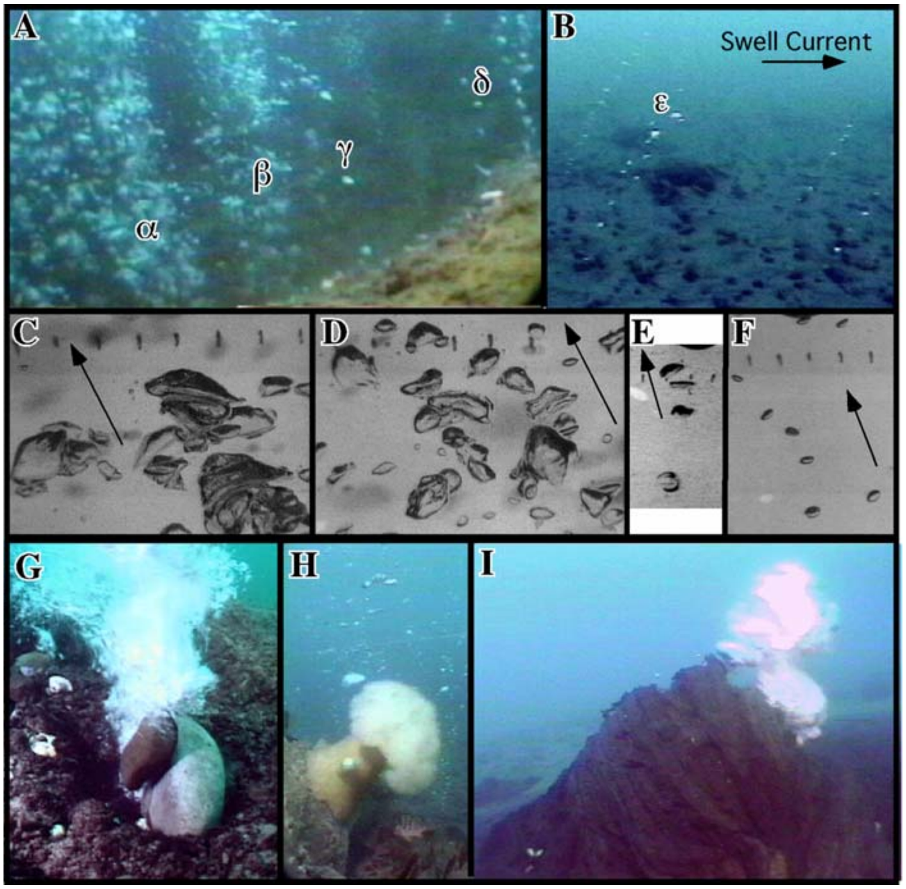

Figure III-2. Seep bubble images showing different vent types. A) is for volcano #1 (2000) B) shows North-East quadrant, ~10 m from mooring point. C) - F) are bubble measurement system images. Arrow shows vertical direction, ticks are 1 cm apart. Bubble streams α and β are from major vents, while γ, δ, and ε are from minor vents. C) and D) show a major vent, E) shows a large bubble minor vent - e.g., γ, while F) shows a small bubble minor vent - e.g., δ and ε.

Figure III-2A shows volcano #1's caldera and walls from which both minor and major vents are emitting bubble streams. Outlying areas contained only minor vents, an example of which is shown in Figure III-2B for ~10 m northwest of volcano #1. Minor vents are characterized by a stream of bubbles rising in trains, and have narrow, sharply peaked size distributions, generally large bubbles with r>2000 μm. Here large bubbles are defined as r>700 μm, since smaller bubbles do not oscillate and behave dirty, while larger bubbles oscillate and behave hydrodynamically clean, even in seawater (Patro *et al*. 2002).

Major vents have much higher emission rates and produce bubbles spanning a broad size range from small to giant (up to several centimeters in diameter). Both minor and major vents can be simulated in the laboratory by blowing air through a capillary tube. At low flow rates, the bubble size is determined by the capillary mouth size and is insensitive to flow rate (Blanchard and Syzdek 1977). However, at high flow rates, the bubbles begin to coalesce before they can separate from the capillary mouth, forming larger bubbles. With increasing flow, turbulent intensities increase, and smaller bubbles begin to appear. Finally, at very high flow rates, a broad spectrum of bubbles is produced (Slauenwhite and Johnson 1999; Tsuge *et al*. 1981).

Elastic vents occur where the seabed behaves like an elastic material, such as tar. In this case the bubble flux depends upon tensile failure of the seabed, which occurs when the buoyancy force becomes greater than the seabed material's tensile strength. Thus the vertical flux is described by punctuated vertical motions at points and times of structural failure followed by static periods of gas accumulation until the next structural failure event. As a result, the time and location of the emission of bubbles is random, or quasi random (Johnson *et al*. 2002). Furthermore, the bubbles are typically emitted in "packets" that can include very large bubbles. An extreme example is shown in Figure III-2I for Ira Seep, located a few hundred meters east of Shane Seep (see Figure III-1) also at 20-m depth. Here, every few minutes the seabed distorts and expands until it ruptures and produces enormous (to 10s of centimeters) bubbles. The tar mound was ~75-cm diameter and ~30-cm high at the time of this image.

The final vent type, obstructed, is a catch-all class that covers vents not easily classified in the other categories. Obstructed vents occur when a physical feature of or above the vent mouth, for example, rocks or kelp fronds, either causes bubble breakup or coalescence into streams of very large bubbles. Two obstructed vents are shown in Figures III-2G & III-2H. In Figure III-2G, rocks in the vent mouth break the bubbles. For this vent, the gas flow was large enough to lift one of the rocks (~5-cm long), in Figure III-2H a log caused coalescence of bubbles from vents under its surface, but upon rising around the log they were broken up while passing through a sea anemonae (*Metridium giganteum*). A sarcastic fringehead (*Neoclinus blanchrdi*) is visible in the image.

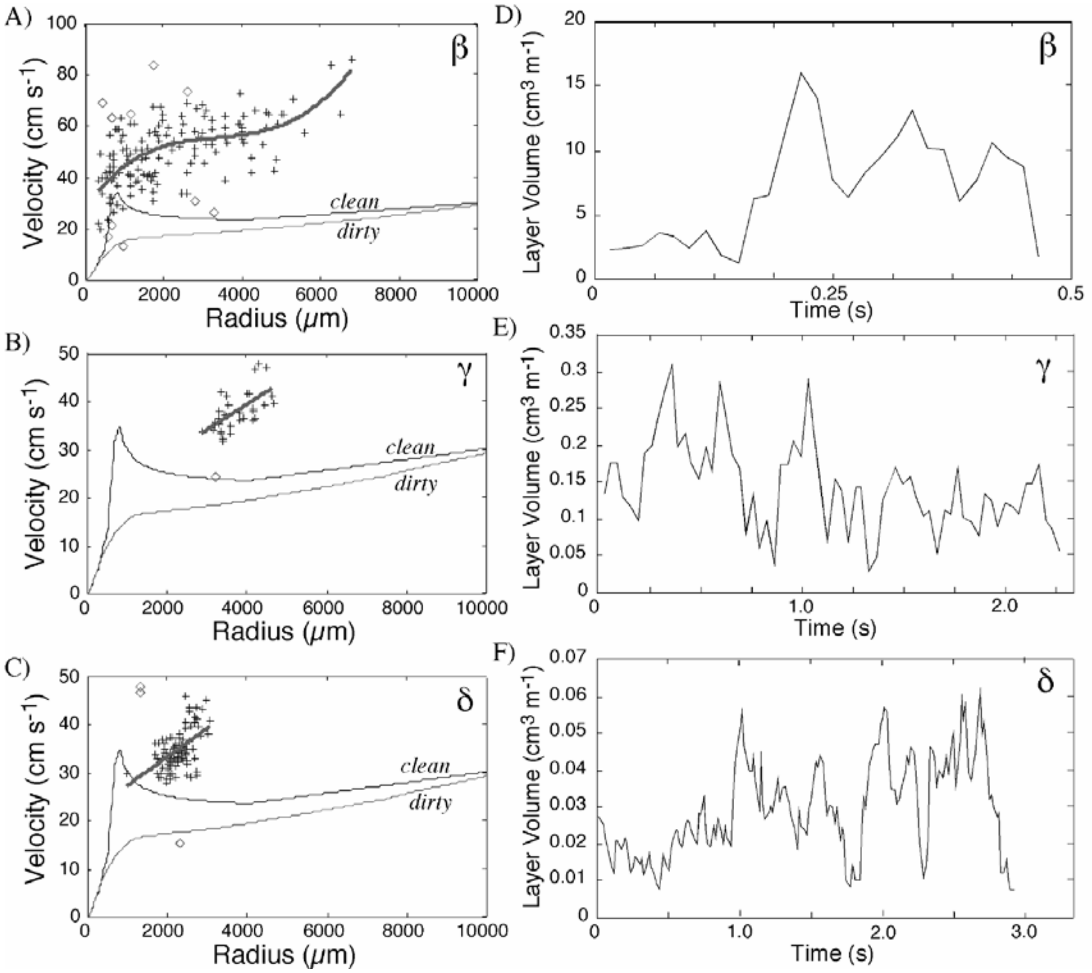

Figure III-3. A) - C) Vertical velocities for vents β, γ, and δ shown in Figure III-2, respectively. Also shown are the clean and dirty bubble rise velocity parameterizations in stagnant water, and polynomial, least-squares fit to the data. Polynomial fits are provided in Table III-1. Diamonds are outliers. Data key on upper panel. D)-F) shows the total layer volume as a function of time for vents β, γ, and δ, respectively.

Table III-1. Summary of bubble plume characteristics.

Plume	β	γ	δ	Anemone
Type	Major	Minor	Minor	Obstructed
Mass Flux (mMol s^{-1})	4.76	0.48	0.22	4.39
Vol Flux (cm^3 s^{-1})	16.8	3.5	1.63	32.2
Vol Layer (cm^3 m^{-1})	35.0	9.7	5.27	50.25
Peak r (μm)	700	3500	2200	30000
$\int\Phi\ \tilde{\xi}$(μm)	6000	3800	2400	15000
V_{up} (cm s^{-1})	40	18	10	30
V_{z1} (cm s^{-1})	36.7	17.9	21.1	49.5
V_{z2} (μm s^{-1})	69.0	53	59.5	10.1
V_{z3} (μm s^{-1})	-0.003	-	-	-

V_{up} is upwelling flow, V_Z is a polynomial of form $V_Z = V_{Z1} + rV_{Z2}$ with r, bubble radius, in cm. $\int\Phi\ \underset{\cdot}{\tilde{5}}$ is the radius at which the integrated mass flux accounts for 50% of the plume mass. Volume flux and layer volume were corrected to STP.

Seabed observations of Major and Minor Vents

As discussed in the methods section, calculation of Φ requires both the vertical velocity and Ψ. The vertical velocities for the vents shown in Figure III-2, labeled β, γ, and δ are shown in Figure III-3A-C. The flux from the major vent (b) consisted of pulses of very large bubbles emitted every ~0.1 s, that rose very fast, entraining other bubbles and generating significant turbulence. As a result, the standard deviation in the velocities is very large. Also shown in the figure are the clean and dirty parameterizations (Clift *et al.* 1978) for stagnant water. The difference in velocity between these parameterizations and the data is due to the upwelling flow. A third-order polynomial fit to the data also is shown and largely follows the dirty curve for *r*<5000 µm, strongly suggesting that oil contamination has caused bubbles to behave hydrodynamically dirty for *r*<5000 µm. The sharp increase for *r*>5000-µm bubbles is due to the much higher upwelling flow associated with the pulses of the largest bubbles, although these largest bubbles were not in the field of view sufficiently long to measure their velocity.

The mean upwelling flow can be estimated from the difference between the dirty parameterization curve and the fit, and was ~30 cm s^{-1}. During the bubble pulses, though, it increased to more than 80 cm s^{-1}. Given the smaller flux, it is not surprising that smaller upwelling flows were observed for the minor vents. Assuming bubbles from these smaller vents are as oily as the main vent, the estimated upwelling flows for γ and δ, were 15 and 20 cm s^{-1}, respectively.

Ψ was calculated for each distribution for each frame, and integrated over r to calculate the total layer bubble volume (cm^3 per vertical meter) as a function of time, and is shown in Figures III-3D - F. The volume flux for the major vent is dominated by the largest bubbles that escape each ~0.15 s, and causes peaks in Figure III-3D. The minor vent bubble streams also show evidence of temporal variability, or pulsing. Note that volume fluxes for the major vent are ~20 to 30 times greater than for the minor vents.

The Φ distributions for the three vents shown in Figure III-2 are shown in Figure III-4. The major vent had a very broad distribution including bubbles as small as 275-µm radius (near the lower resolution limit). Very large bubbles also were observed, with the largest ~1.5-cm radius, one of which is visible in Figure III-2C. In contrast, the two minor vents produced narrow bubble distributions, with peaks at 2200 µm and 3500 µm for vents δ and γ, respectively. Also, note that the peak in $\underset{\cdot}{\Phi}$ for the minor vents was greater than for the major vent at the same radius; thus the much larger flux from the major vent is accounted for by the broadness and presence of very large bubbles.

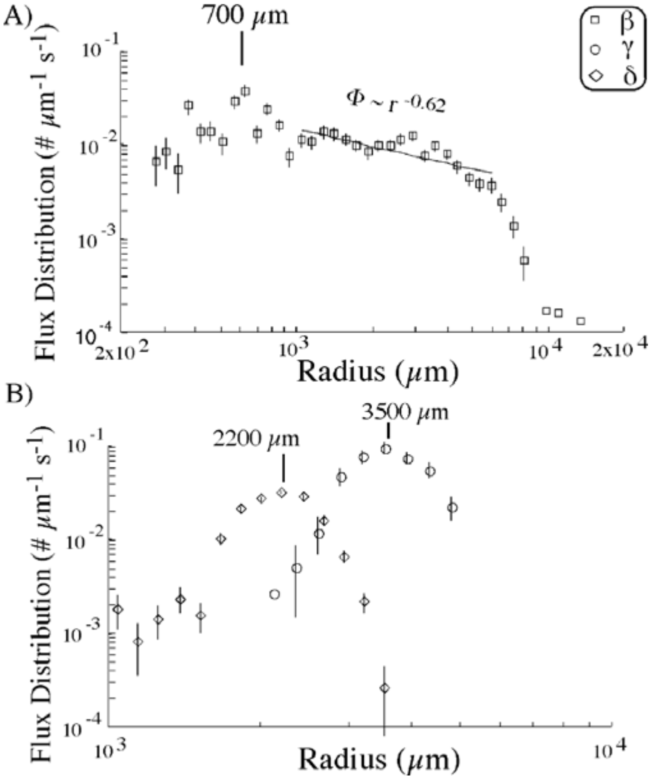

Figure III-4. Bubble emission flux distributions for A) Major and B) Minor vents. Distributions are for BMS images in Figures III-2C- F. Data key on upper panel. Also shown is fit to Major vent data. Error bars are 1 standard deviation.

To identify which bubbles are most important to the mass flux, the normalized cumulative (i.e., integrated) mass flux for the three vents in Figure III-4 was calculated and is shown in Figure III-5. The dashed lines show the e^{-1}, 0.5, and $1-e^{-1}$ levels. The width between e^{-1} and $1-e^{-1}$ indicates the narrowness of the mass dominating bubbles and was comparable for both minor vents (~700 μm), while the major vent spanned a much broader range (~2000 μm). For both minor peaks, the 50% level was reached at r only slightly larger than the peak Φr, indicating the peaks were narrow and symmetric. The major vent; however, had 50% of its mass contained in bubbles larger than 6000 μm, while its peak in Φ was at 700 μm. Thus the mass distribution was highly skewed, with bubbles at the peak in Φ (700 μm) contributing negligibly to the total mass flux.

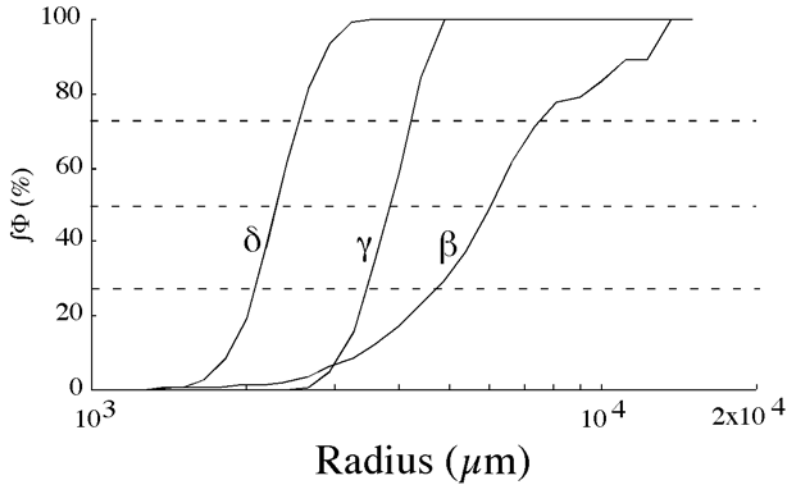

Figure III-5. Integrated cumulative emission flux distributions, ∫Φ, for vents in Figure III-4. Vents labeled on figure.

Seabed Observations of Obstructed and Elastic Vents

It is difficult to generalize to obstructed vents, as they are highly dependent upon the obstruction's geometry. An example is shown in Figure III-3H where a log caused coalescence into very large bubbles, that upon rising hit a sea anemonae that causes bubble break-up in some bubbles. This vent was located ~3-m North of the mooring point and was videoed in 2001. The function V(r) is shown in Figure III-6A, along with the clean and dirty parameterizations and a linear fit to V(r). For bubbles with r>1 cm, surface contamination has negligible effect on bubble rise and the clean and dirty parameterizations converge. The values of V(r) show a consistent offset of ~30 cm s^{-1}. Since the bubbles were 30 - 50 cm apart, the upwelling velocity probably represents that of the general area from all the rising bubbles at a height of ~1.5 m above the seabed - other V(r) were measured 30 cm above the seabed). The upwelling velocity agrees well with dye release measurements of the upwelling flow, where it took approximately 50 seconds for the dye to travel the 22 m to the sea surface during two separate dye release experiments (Clark *et al.* 2003). This upwelling flow implies a significant vertical water flux, as evidenced by the observation that it only took a few minutes for the water at the seabed to become clear of excess green dye, despite very weak currents at the seabed. Also, on days where the swell has stirred up the seabed, bubble plumes at the sea surface are observed as brown due to turbidity (apparent in BMS video) compared with the surrounding water.

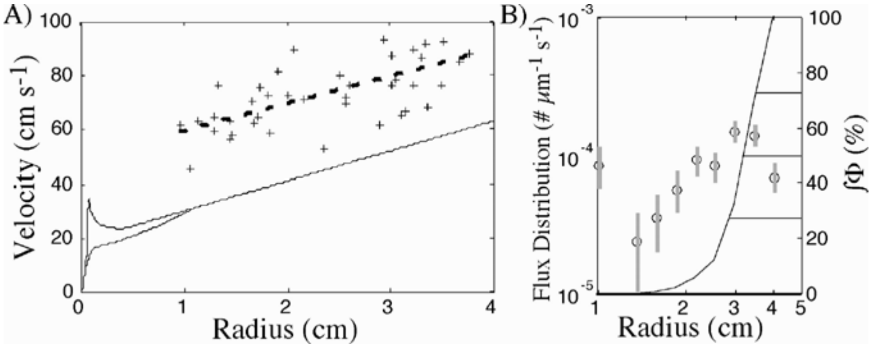

Figure III-6. A) Vertical velocity as a function of radius for the obstructed vent shown in Figure III-2H. B) Shows emission flux distribution, and integrated cumulative emission flux distributions, ∫Φ.

The emitted bubbles were ~3 cm radius, but smaller bubbles were formed when these bubbles fragmented. Bubbles with r<1 cm probably were formed, but were below the minimum size resolution. These very large bubbles are unstable during rise and break-up during ascent (Clift *et al.*, 1978). Divers followed some of these large bubbles during their rise and observed trails of smaller bubbles breaking off the giant bubbles' trailing edges. These smaller bubbles rise slower than the giant bubbles, forming trailing bubble chains, similar in appearance to jellyfish tentacles. By 10 meters above the seabed giant bubbles were largely absent. Distributions from elastic vents were not available; however, surface observations at Ira Seep showed bubbles 10 - 30 cm reaching the surface followed by a cloud of smaller bubbles. The key to the survival of the enormous elastic vent bubbles at Ira Seep through 20 m of water may be that they were not rising in a turbulent bubble plume, and their hydrostatic growth was comparable to loss due to fragmentation and dissolution.

III-3-2. Sea Surface Bubble Observations

As bubbles rise, they grow due to the decreasing hydrostatic pressure, shrink due to dissolution (the outflow of methane and other gas), and grow due to the inflow of dissolved atmospheric gases. Thus, the change in bubble size depends upon the vertical velocity (buoyant rise plus upwelling flow) and the gas exchange coefficient for the bubble, kbub. Both kBub and VB depend upon parameters such as bubble size, temperature, bubble cleanliness, and oil, among other parameters. Thus, measurements of the bubble distribution at the sea surface play an important role in model validation. The model is initialized with the seabed emission size distribution and the predicted bubble size distribution is compared with the measured bubble size distribution at the sea surface.

As with the bubbles at the seabed, bubbles at the sea surface exhibit considerable spatial variability, due in part to the seabed variability, and to the trajectory of the bubbles through the water column and the effect of currents, upwelling flow, and other fluid motions. Thus bubble video was obtained in transects across the seep surface expression. Latitude and longitude are recorded every few seconds, as well as the visual appearance of the bubbles plumes.

Near surface images from Shane Seep (see Figure III-7a) were digitized and analyzed to determine the size distribution, Φ (Figure III-7b), defined as the number of bubbles per size increment (1 μm) in the entire measurement field. Φ shows a relatively broad peak centered at

2500 µm. Minimum resolution for this optical setting was circa 1500 µm. A power law was fit to Φ for r > 3000 µm, where r is bubble radius, and showed a steep decrease with $\Phi \sim r^{-3.1}$. Total seep gas in this image is ~7 cm^3. Φ can be converted to a mass flux by determining the vertical velocity, $V_Z(r)$, which is the sum of the upwelling flow and bubble buoyancy and scaling to the plume cross section. This method was used by Leifer and MacDonald (2003) to estimate seep bubble flux in the Gulf of Mexico.

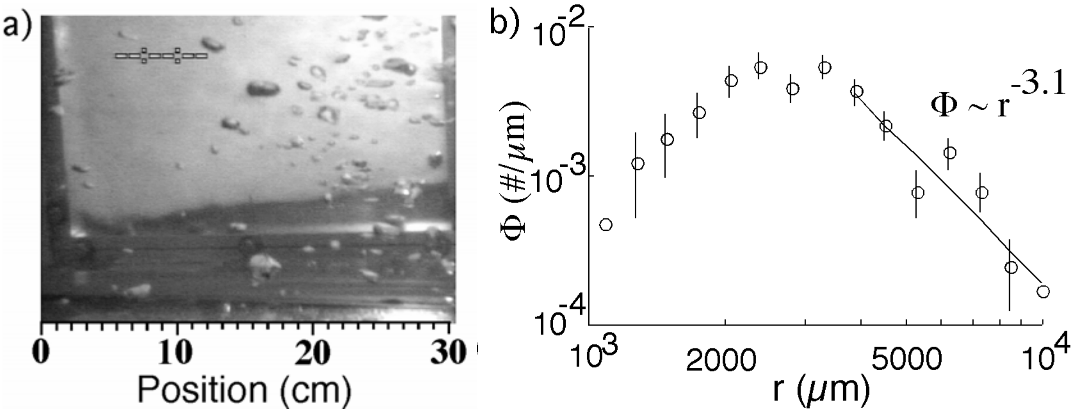

Figure III-7. Image of bubbles from Shane Seep (a) and bubble size distribution, Φ, as a function of radius, r.(b).

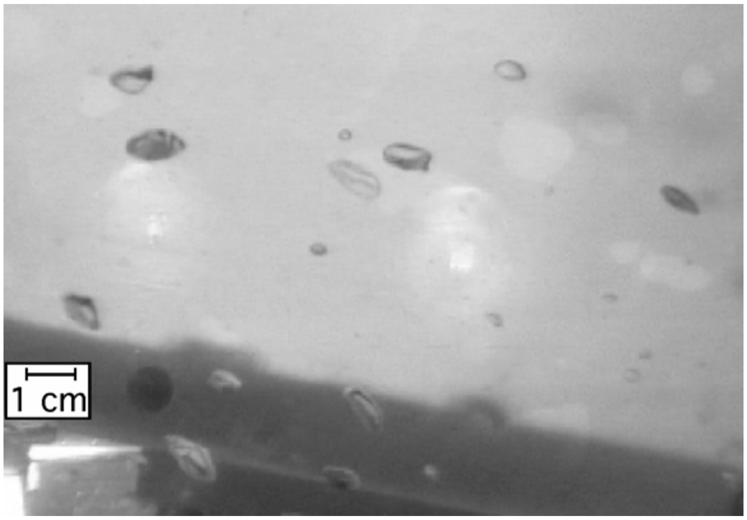

Figure III-8. Image of bubbles from Shane Seep using the closed BMS.

III-4. Results - Bubble and Aqueous Gas Measurements

The fate of the bubble also depends upon the gas composition at the seabed, and also the dissolved aqueous composition through the water column. As an extreme example, if the bubbles were pure carbon dioxide, a much more soluble gas than methane, they would dissolve much faster than if they were pure methane. And if the water was saturated with methane due to the gas outflow from the seep bubbles, the bubble dissolution rate would be significantly decreased, and some bubbles might even effervesce, or grow as methane from the water flows back into the bubble. Thus saturation of the water column can have a significant impact on bubble survivability and the transport of methane to the atmosphere.

III-4-1. Dissolved Methane and Higher Alkanes

In addition to measuring the major atmospheric and seep gases, we also measured trace gases, such as ethane, butane, etc., at the seabed and sea surface. Since each of these gases has different diffusivity and solubility, their concentration will evolve differently with time. As a result, they provide a good constraint on numerical model predictions.

To characterize the seep environment, dissolved gases, bubble gas composition, and fluid motions were measured at three seeps of different sizes and depths, La Goleta Seep (LGS), Thor CP Seep (TCS), and Seep Tent Seep (STS). Attributes and locations, major gas observations, and trace gas observations are presented in Tables III-1, III-2, and III-3. At each seep, water and bubble gas samples were collected in the fluid and in the rising bubble plume at the surface. These samples were analyzed for carbon dioxide (CO_2), oxygen (O_2), nitrogen, (N_2), CH_4, and higher n-alkanes to $n = 5$ (Table III-2). The sea floor gas composition was estimated from measurements collected between 1982 and 1996 at the Seep Tents. For a discussion of the Seep Tents see *Rintoul* (1982); Boles *et al.* (2001).

Table III-2. Natural hydrocarbon seeps visited. Locations are at 119°W, 34°N. TCS - Thor CP, LGS - La Goleta Seep, STS - Seep Tent Seep.

Name	Location (Lat. , Lon.)	Depth (m)	Area (m^2)	V_{up} m s^{-1}	Relative Activity
TCS	52.442', 23.650'	20	2	-	Low
LGS	51.183', 22.500'	70	25	0.3	Active
STS	53.350', 23.050'	70	700	>1	Extreme

V_{up} is the upwelling velocity.

Table III-3. Summary of major gases bubble partial pressures and dissolved concentrations. STS_2 is STS corrected to 2 m for comparison with other seeps. STS_B is STS at the seabed.

Seep	z (m)	$P(O_2)$ mbar	$P(N_2)$ mbar	$P(CH_4)$ mbar	C_{MET} µMol/l	HC_{MET} mbar
STS	1	85	251	691	1000	860
STS_2	*2*	*93*	*274*	*754*	-	-
LGS	2	105	339	700	1200	810
TCS	2	75	203	758	260	190
		%		%	%	
STS	1	7.69	22.8	62.8	1000	860
STS_B	70	0.14	0.79	87.5	-	-

z is sample depth, P is partial pressure, C is concentration, MET is CH_4, and H is the Henry's Law Constant for 12°C.

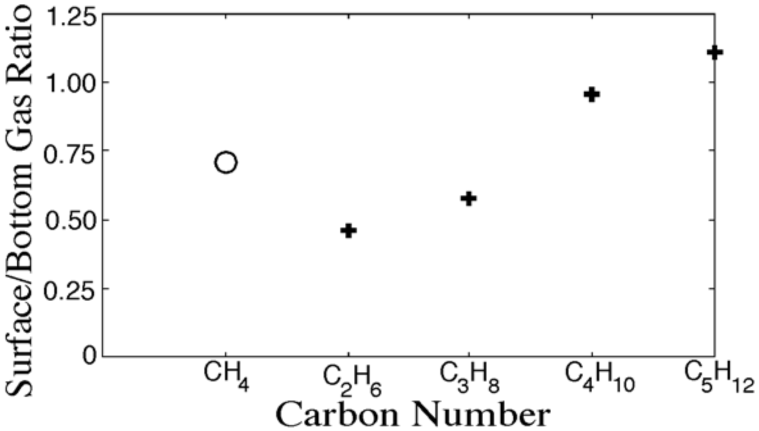

Figure III-9. Alkane ratio from sea floor to sea surface for Seep Tent seep (34° 53.35' N, 119° 23.05' W) bubble gas.

Aqueous methane, CH_4, concentrations near the surface in the bubble plumes have been found to be substantially greater (>10^8 times) than atmospheric equilibrium values. At three of the four seeps sampled, CH_4 near the surface was slightly supersaturated with respect to the bubble's partial pressure (Leifer *et al.*, 2000a). Thus the rate limiting step for CH_4 dissolution into the water column was not bubble gas transfer, but rather mixing (by advection and diffusion) between the saturated bubble plume water and the bulk ocean.

Partial pressures for the alkane series to pentane (Table III-4) were also determined for the bubbles (dissolved n-alkane concentrations were not determined). In all cases n-alkane partial pressure decreased with n-alkane number, *n*. At STS a comparison between seafloor and surface bubble composition showed that the lighter n-alkanes (ethane and butane) decreased by about 50% and that the higher alkanes decreased significantly less. Overall, during their rise, bubbles became enriched in the heavier n-alkanes relative to the lighter n-alkanes. This observation can be understood with respect to the process of bubble-mediated gas exchange. As a seep gas bubble rises, it exchanges gas with the surrounding water (seep gases outflow and atmospheric gases inflow). Since this is a diffusive process, the heavier alkanes with lower diffusivity, **D**, exchange slower, and as a result, bubbles become enriched with these gases.

Table III-4. Summary of trace gas bubble observations at sample depths listed in Table III-3. For STS units are % mole fraction.

Seep	$P(C_2H_6)$	$P(C_3H_8)$	$P(C_4H_{10})$	$P(C_5H_{12})$
	mbar	mbar	mbar	mbar
STS	25.6	19.6	4.54	2.93
STS_2	*27.9*	*21.4*	*4.95*	*3.19*
LGS	20.6	16.3	5.14	2.98
TCS	14.6	17.7	5.95	4.54
	%		%	%
STS	2.33	1.78	0.41	0.27
STS_B	5.09	3.07	0.43	0.24

P is partial pressure.

At the sea floor, bubbles are about 90% CH_4 and 10% higher hydrocarbons while at the surface of the deeper seeps (65 m) they are about 60% CH_4, 30% air, and 10% higher hydrocarbons. The decrease in CH_4 at a shallow seep (20 m) was much less; the surface composition was about 70% CH_4, 15% air, and 15% higher hydrocarbons. For alkanes heavier than CH_4 (i.e., crosses on Figure 1), the ratio of the surface to sea floor mole fraction showed a linear enhancement (see Figure 1) with increasing alkane number. CH_4 behaved differently because the water column was saturated with CH_4.

III-4-2. Dissolved Oil

Preliminary investigations have shown that spectrofluorometry can be used to investigate oil dissolution from the bubble plume. Water samples were obtained in a horizontal transect under the seep surface expression at a depth of 1 m for fluorometric and gas chromatographic (GC) analysis. The features of the surface expression of the seep are shown in Figure III-10a. The current was towards the north, while the transect line was cross current (east to west). Within this surface expression, there were three different regions, the central upwelling area where most bubbles surfaced, an outwelling region where flow from the central region dominated, and an outer region where oil slicks were visible.

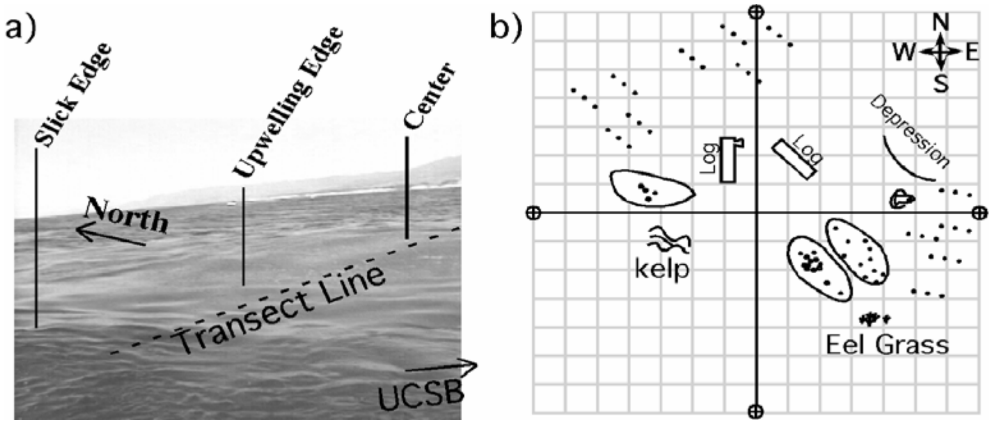

Figure III-10. Shane Seep (34°24.37’ N, 119° 53.41’ W) surface expression showing features and sampling transect (a), and sea floor map at 20 m depth (b). Squares in (b) are is 1 m by 1 m and dots represent seafloor vents.

Transitions between these regions are marked on Figure III-10a. There were two strong bubble plumes in the central region, presumably one for each of the large sea floor vents - located in mud volcanoes. A sea floor map of the major Shane Seep features is shown in Figure III-10B, corresponding to Figure III-10A, before formal survey measurements were conducted. Spectrofluorometry results are shown in Figure III-11A. Excitation was at 337 nm, emission was integrated over 350 - 600 nm, and values are normalized to quinine sulfate. Spectra showed clear oil signatures. The transect (shown in Figure III-10A) was cross current, and the surface slick features corresponding to Figure III-10A are indicated on Figure III-11A. The 0-m coordinate is centered in one of the bubble plumes. Between the two bubble plumes was a surface convergence zone (+2 m) that showed local fluorescence maxima. The highest fluorescence was located under the visible surface slick (-10 m), while the lowest was in the center (+3 m). This trend was also observed at 15 m (Figure III-11B), and is consistent with advection by the strong outward surface flow of dissolved from the bubble plume. Moreover, within the plume, it is likely that the high number of bubbles effectively collects, or sparges, oil from the water column.

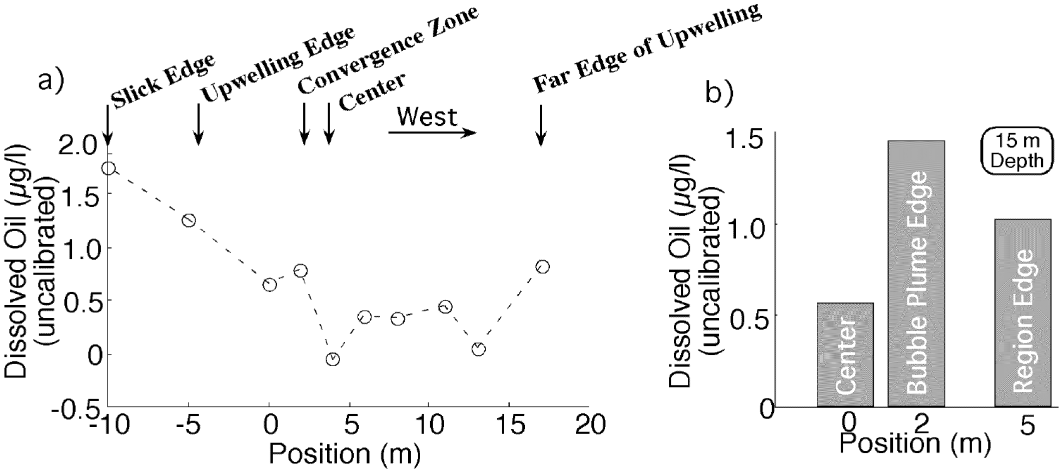

Figure III-11. Plot of excitation-emission fluorescence, normalized to quinine sulfate with background subtracted, for 1 m depth (a) and 15 m depth (b) for Shane Seep.

III-4-3. Fluid Motions and Plume/Ocean Interactions

Strong upwelling velocities were observed at larger seeps and all showed surface divergence. Dye released at La Goleta Seep rose at circa 30 cm/s, while at both Shane Seep and the Seep Tent Seep, vertical rise was in excess of 1 m/s, and very unsteady. Our present research is addressing not only bubble plume dynamics and geochemistry but also ocean-bubble plume interactions. For example, saturation of the bubble plume water is very important to the bubble dissolution rate (i.e., survivability). Thus, the exchange rate between the bubble plume and the bulk ocean (that is significantly undersaturated with respect to the bubbles) is critical for determining the fraction that dissolves during transit. Dye was released at the bottom of Shane Seep and rose through the 22-m water column in 54 s, or 41 cm/s. During the dye release, the dye initially spread out into a cloud ten meters or so in diameter; however, over the subsequent minute, all of the dye was entrained and arrived at the surface.

III-4-4. Atmospheric Methane Emission Plumes

Overview

Subsurface measurements present a time sequence of the gas emissions from a single vent, or for a flux buoy (Washburn *et al.*, 2005) a small fraction of a plume. Sonar has greater potential as the time necessary to map a plume is less; however, the inversion problem presents numerous challenges (Hornafius *et al.*, 1999). From the time-spatial sequences, a map of the emission flux can be derived, based on the assumption that emission is constant with time, or that the sampling at each location is statistically-significant and normally distributed with time. Unfortunately, variations in seep emission occur on all time scales, from the sub-second to swell time-scales (Leifer and Boles, 2005a), to tidal (Boles *et al.*, 2001) and longer. These variations occur due to external forcing, such as swell and tides, and internal processes, such as oil-gas interactions and changes in the resistance due to tar accumulation and advection.

Clearly, the ability to obtain an integrated emission flux from a seep area would be invaluable. Efforts were made to use in-situ atmospheric methane measurements to measure the total integrated emission from a seep area. These efforts were aimed at interpreting fortuitous observations of a blowout.

Methane and non-methane hydrocarbons in the Santa Barbara County

The 1999 reactive organic gas, ROG, emissions inventory for Santa Barbara County was 80.37 tons dy^{-1}, excluding vegetation sources. Vehicles (cars, trucks, airplanes, etc.) were the dominant human emission source (25.9 tons dy^{-1}). Off-shore activities (petroleum production, distribution, and shipping) contributed a small fraction (2.84 tons dy^{-1}). Stationary sources include power generation, and industrial activities like surface coating (*SBCAPCD* 2001). Marine hydrocarbon seeps in the Santa Barbara Channel are among the largest in the world, significantly affecting air quality in Santa Barbara County. From sonar survey estimates, the seeps release 10^5 m^3 day^{-1} of gas and 100 bbl day^{-1} oil (Quigley *et al.* 1999). Assuming a 30% volatile component in the oil, marine seeps contribute 35±7 tons ROG day^{-1}, or 43% of the county ROG, and thus are a very significant ROG pollution source. This ROG reacts with NOx to form ozone thereby lowering air quality standards.

On-shore observations of seep emissions

The map of the seep field shown in Figure III-12 shows the location of the West Campus Air Pollution Station (WCS), which is owned and operated by Venoco, Inc. for the Santa Barbara County Air Pollution Control District (SBCAPCD). With respect to Shane Seep, WCS is in the onshore direction (47°) and 1.49 km distant and approximately 700 m inshore. Wind-veering can be considered negligible given the proximity of WCS to the shoreline and lack of significant topographic features in the vicinity – WCS is 6 m above sea level.

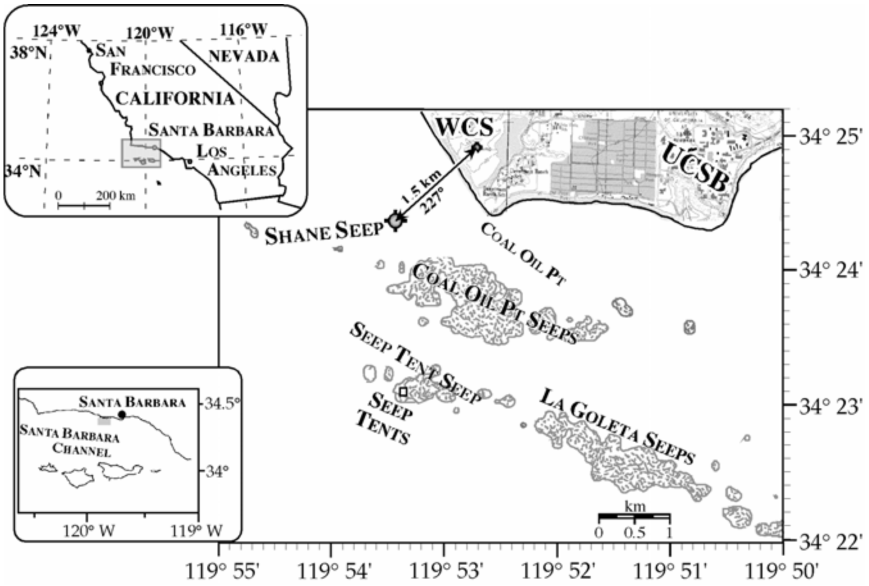

Figure III-12. The Coal Oil Point seep field, Santa Barbara Channel, California. Upper left panel shows location in California, lower left panel shows Santa Barbara Channel. Gray areas in main panel indicate regions of high bubble density determined from sonar returns (*Hornafius et al.* 1999). Inshore seeps were too shallow for the sonar survey. WCS is West Campus air pollution station (34° 24.915' N, 119° 52.716' W), UCSB is University of California, Santa Barbara.

The significance of the seeps is shown in the THC data from WCS. Figure III-13 shows that winds at WCS in 2001 primarily were dominated by the onshore breeze and less so by the offshore (night) breeze, although there was also a strong prevailing wind component (westerly). Figure III-13A shows the total number of hours the wind blew in each direction bin. Average total hydrocarbon, THC, concentrations as a function of wind direction were calculated by first segregating all 2001 wind direction measurements into 2° direction bins. Then, all THC measurements in each (2° direction) bin were averaged (Figure III-13B). The averaged THC data shows the primary THC pollution source for WCS is the Coal Oil Point Seeps. High THC values clearly correlate with winds from azimuths to the seeps, with the greatest values due south, i.e., from the Coal Oil Point Seeps and the Seep Tent Seep, but also from Shane Seep. In contrast, land sources produce lower THC concentrations at WCS. This is partially because the sources are farther away, but primarily since the main land based THC source (rush hour) only lasts a few hours its average is lower than for the continuous seep emissions.

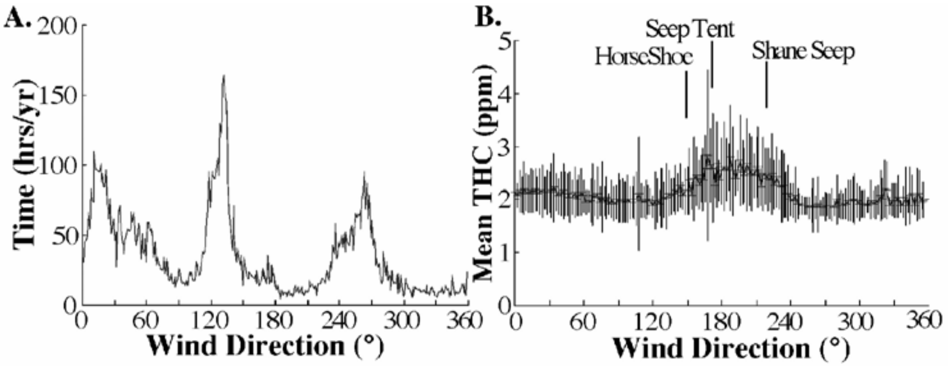

Figure III-13. A) Hours per year wind direction in 2° bins for WCS in 2001 from hourly readings. **B)** Total hydrocarbon concentration (THC) at WCS for 2001 from hourly measurements as a function of wind direction in 2° bins. Direction to various seeps labeled on figure.

Source strength (i.e., total emissions along the wind path can be estimated from back trajectory calculations for an atmospheric plume.

For a Gaussian plume, the ground concentration downwind, *C*, is (Hanna *et al.* 1982):

$$C(x,y) = k(x,y)Q \tag{1}$$

where *x* and *y* are the downwind and transverse distances from the source, respectively, *Q* is the source strength, and *k* describes how *Q* decreases with distance. If *k* is expanded (1) can be rewritten as:

$$C(x,y) = 2\pi\sigma_z(x)\sigma_y(x)Qu\ e^{-\frac{1}{2}\left(\frac{Y}{\sigma_y(x)}\right)^2} e^{-\frac{1}{2}\left(\frac{Z+h}{\sigma_z(x)}\right)^2} \tag{2}$$

where *z* is height, σ_y and σ_z are the horizontal and vertical diffusion coefficients, respectively *u* is the wind speed, and *h* is the emission height. The value of *h* can be assumed zero, since even though methane is lighter than air it is still a small fraction of the total air gases. Both σ_y and σ_z are described by functions of *x* that depends upon atmospheric stability, which depends upon solar insulation, surface roughness, and *u*, or can be determined directly from wind measurements. For example, for slightly unstable conditions that occur for light sun and $3 < u < 4$ m s^{-1}, or for moderate sun and $2 < u < 3$ m s^{-1}, and surface roughness typical of the ocean at 3 m s^{-1}, Briggs turbulence yields:

$$\sigma_y = 0.11x\big/\sqrt{1+10^{-4}x}\,;\ \ \sigma_z = 0.08x\sqrt{1+2x10^{-4}x} \tag{3}$$

Thus for *C* measured at a known distance from the source, *k* can be calculated from (1) and *Q* estimated. There is some uncertainty in the validity of equations for σ_y and σ_z for coastal conditions since the parameterizations for σ_y and σ_z as in (3) were from land studies.

On-water observations of seep emissions

Greater detail about the seep emissions and fluxes to the atmosphere can be measured from in-situ THC measurements. A Flame Ion Detector (OVA-88, Foxboro) was used to measure methane in-situ and was recorded with a multichannel data logger (OMP-MODL, Omega Corp, CT). Although seep gas at the seabed contains significant CO2 (12%), and ethane (3%), with trace air and higher n-alkanes, by the time the bubbles reach the sea surface, the more soluble components have been stripped out. Air samples collected above Shane Seep in 1-L Teflon bags (SKC, PA) were analyzed by the Southern California Gas Company, Engineering Analysis Center (Table III-5). Atmospheric composition was 1.91% methane, with combined n-alkanes comprising <0.02%. Thus, although non-methane seep gas components do enter the atmosphere, hydrocarbons were more than 95% methane.

Table III-5. Atmospheric gas composition above Shane Seep.

Gas	Seabed (%)	1-m Depth (%)	Atmosphere (%)
CH4	84.0	79.4	1.91
C2H6	1.2	0.80	N/A
C3H8	1.1	0.79	0.0033
C4H10	.55	0.46	0.0026
C5H12	.18	0.18	0.0015
C6+	N/A	N/A	0.0156

Methane is emitted in highly discrete locations due to the rising bubbles. These atmospheric plumes rapidly mix, forming a large plume that is advected and diffuse laterally and vertically downwind. To create a spatial plume map, the plume was repeatedly transected. A transect lasted two to three minutes and was easily resolved the CH_4 plume. A sample transect is shown in Figure III-14 for August 13, 2003. This transect was very near to Shane Seep and methane levels were as high as 12 ppm. The background level represents elevated methane levels in this portion of the seep field. In August 2003, Shane Seep was characterized by three main plumes, within a larger area of a dispersed bubble emissions, plus a second area of seepage ~50 m to the west (W. Shane Seep). Plume structure is clearly visible and arises from variability in temporal and spatial emissions and turbulence. Thus, some of the heterogeneity is due to resolving the multiple sources of methane. A second source of variability is likely due to swell. Leifer and Boles (2005b) showed that seepage at Shane Seep responds at swell frequencies. Their study was for the peripheral vent area of the Shane Seep area; however, visual observations reveal strong pulsing of the main plume at circa the swell frequency. Thus, some of the variability likely is due to swell induced modulation. The dashed line represents a column height of methane that is one half the atmospheric column height of methane.

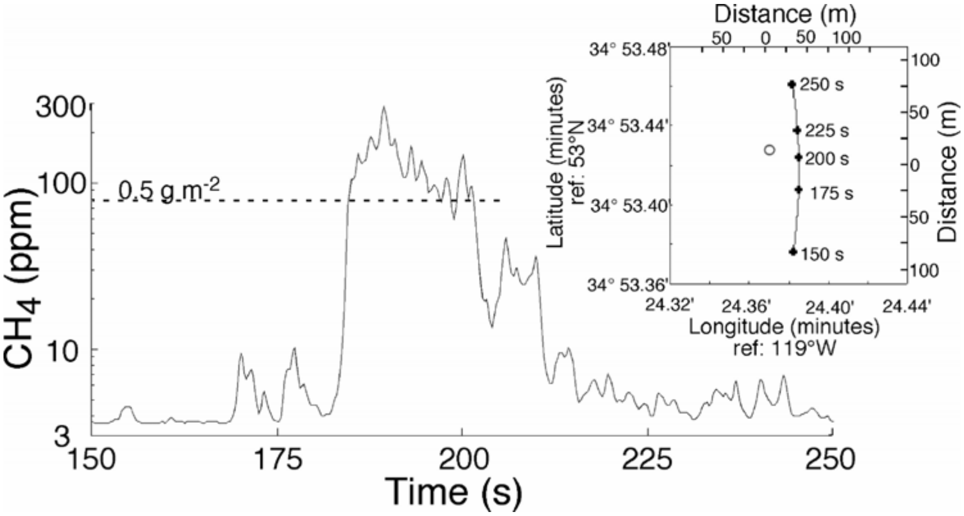

Figure III-14 Transect through the Shane Seep plume ~50 m downwind for Aug 15, 2003. Dashed line roughly corresponds to a 0.5 g column height of methane. times background CH_4. Inset shows location and distance scale of transect and is referenced to 119°W, 34°N; circle shows location of Shane Seep.

A contour map from the same survey is shown in Figure III-15. Two sources are clearly identifiable, one due to bubbles entering the atmosphere (the roughly East-West trend) and one due to air-sea exchange from the dissolved CH_4 plume (34° 24.40'N, 119° 53.40'W). The wind-driven plume was heading offshore and trails off towards the South.

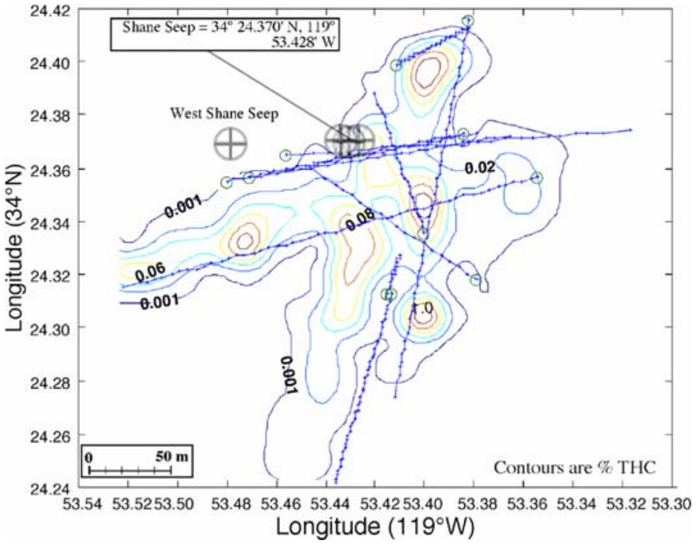

Figure III-15. Contour map of Shane Seep atmospheric THC concentration (%). Lines show boat tracks, with ticks indicating measurement points and circles show starting points. Location of Shane Seep and West Shane Seep indicated by targets. Distance scale shown on figure. Measurements were gridded to 0.01° latitude-longitude bins and measurements in each bin averaged. Winds were light (2 m s^{-1} to 2.8 m s^{-1}) from WNW. Currents were to the north at ~0.5 m s^{-1}.

The contour map is only a two dimensional representation of methane concentrations near the sea surface of a three-dimensional plume; however, all the methane in the plume must be considered for flux estimates. A three-dimensional Gaussian plume was matched to the surface data (Figure III-16) to estimate the methane column-height and the emission flux or source strength, Q.

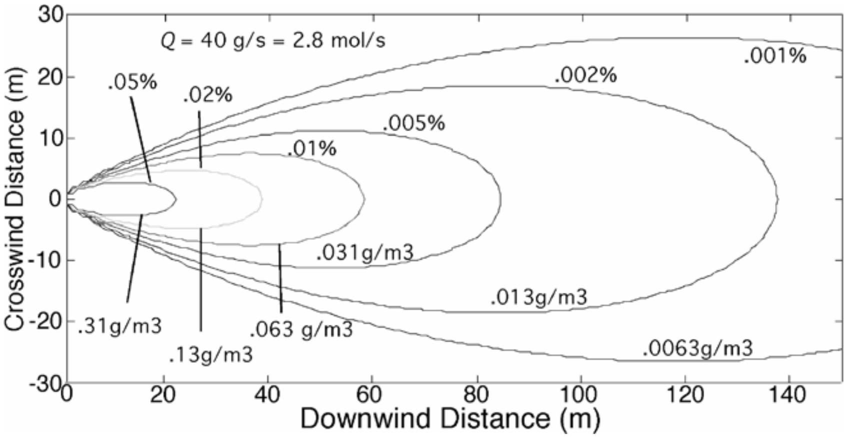

Figure III-16. Contour plot of Gaussian plume model for sea surface CH4 (%). *Q* is source strength.

A rough fit to the sea surface data by adjusting the Gaussian plume parameters is shown in Figure III-16. Briggs turbulence for moderate sun and moderately stable conditions and 2.9 m/s wind speed was used. Using the plume formulation (2), the vertical column of CH_4 per square meter was calculated and is shown in Figure III-17. For a Gaussian plume and for the first few hundred meters from the source, over 99% of the methane is found in the lowest 100 m of the atmosphere.

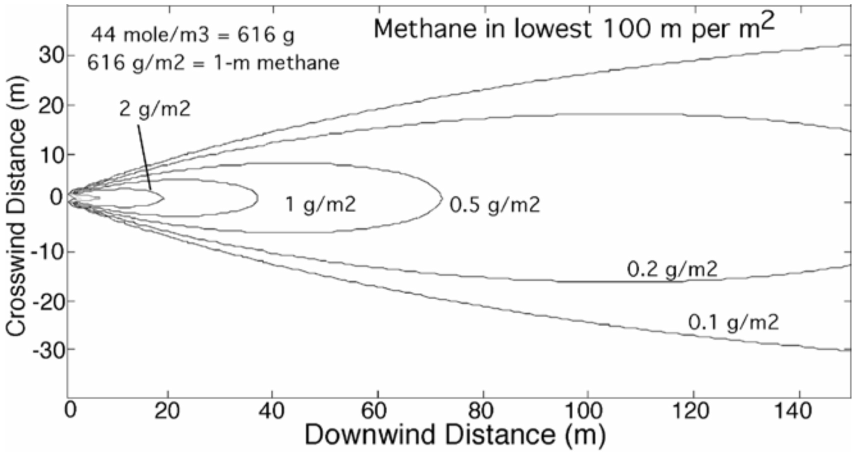

Figure III-17. Contour plot of vertical integration of Gaussian plume. Figure III-16 shows the sea level expression.

III-4-5. Extreme Emission Events – BLOWOUT!

The techniques described and ground truthed in section IV-4-4 were used to study a fortuitous observation of a large transient emission from Shane Seep, a blowout. Much of the following text is adapted from a manuscript for submission.

Introduction

Atmospheric methane, CH_4, is an important greenhouse gas at least 20 times more potent than carbon dioxide (Khalil and Rasmussen 1995) whose mixing ratio has more than doubled during the last century (Rowland 1985). CH_4 has both anthropogenic (375 Tg) and natural sources (160 Tg) of either biologic or geologic origin (Prather *et al.* 1995). Natural geologic sources include marine seepage associated with hydrate dissociation and leakage from deeper hydrocarbon reservoirs. The contribution of these seafloor sources to atmospheric CH_4 is uncertain due to the likelihood that some or all of the emitted CH_4 dissolves into the ocean during transit from the seabed to the sea surface (Clark *et al.* 2003; Heeschen *et al.* 2003; Leifer and Judd 2002). Global estimates from marine seeps (neglecting hydrates) are ~20 Tg yr^{-1} (Kvenvolden *et al.* 2001), or ~13% of natural emissions. Although seeps are found on all continental shelves (Hovland *et al.* 2003), few quantitative emission rates exist. Furthermore, while marine sediments preserve widespread evidence of large transient CH_4 releases, the magnitude and frequency of these transient events remains unknown. Thus, the seep contribution based on gentle bubble emanations typical of steady-state seepage likely is an underestimate since it neglects the contribution from large transient events.

CH_4 hydrate dissociation has been proposed to play an important role in atmospheric CH_4 budgets and climate change – e.g., The Clathrate Gun Hypothesis - (Kennett *et al.* 2003; Katz *et al.* 1999; Severinghaus *et al.* 1998; Dickens *et al.* 1995). For tropical to mid-latitude oceans, CH_4 hydrate deposits are at depths where water-column transit may represent a formidable barrier.

Herein, we present the first quantitative observations of a large transient seepage emission, and numerical model results based on the observations indicating that these events allow significant CH_4 to reach the atmosphere even from the deep sea. Given the vast estimated CH_4 hydrate reserves – $5x10^6$ Tg, any process that enhances the marine geologic CH_4 contribution to the atmosphere is important. This is particularly relevant since global warming and increased ocean temperature likely will increase hydrate dissociation (Hatzikiriakos and Englezos 1993).

Observations

Observations were at a highly active, shallow (22 m) marine seep area (unofficially named Shane Seep; 34° 24.370’N, 119° 53.428’W), in the Coal Oil Point (COP) seep field, near the University of California, Santa Barbara (Figure III-12). The Shane Seep area is located at the intersection of crossing E-W and NE-SW fault trends (Mark Kammerling, Venoco Inc. pers. com., 2004).

Intense seepage at Shane Seep escapes from vents centered in several pockmark-like hydrocarbon (HC) volcanoes (Leifer *et al.* 2004). On November 7, 2002, two heavy iron chains were lain down along N-S and E-W lines, which transected HC volcano #3 that had formed a few weeks earlier. Several months later, video surveys showed the chain on the seabed except where it penetrated the volcano walls, demonstrating a depositional process for the formation of HC volcano walls. Observations described below suggest chain burial likely occurred from multiple blowout events.

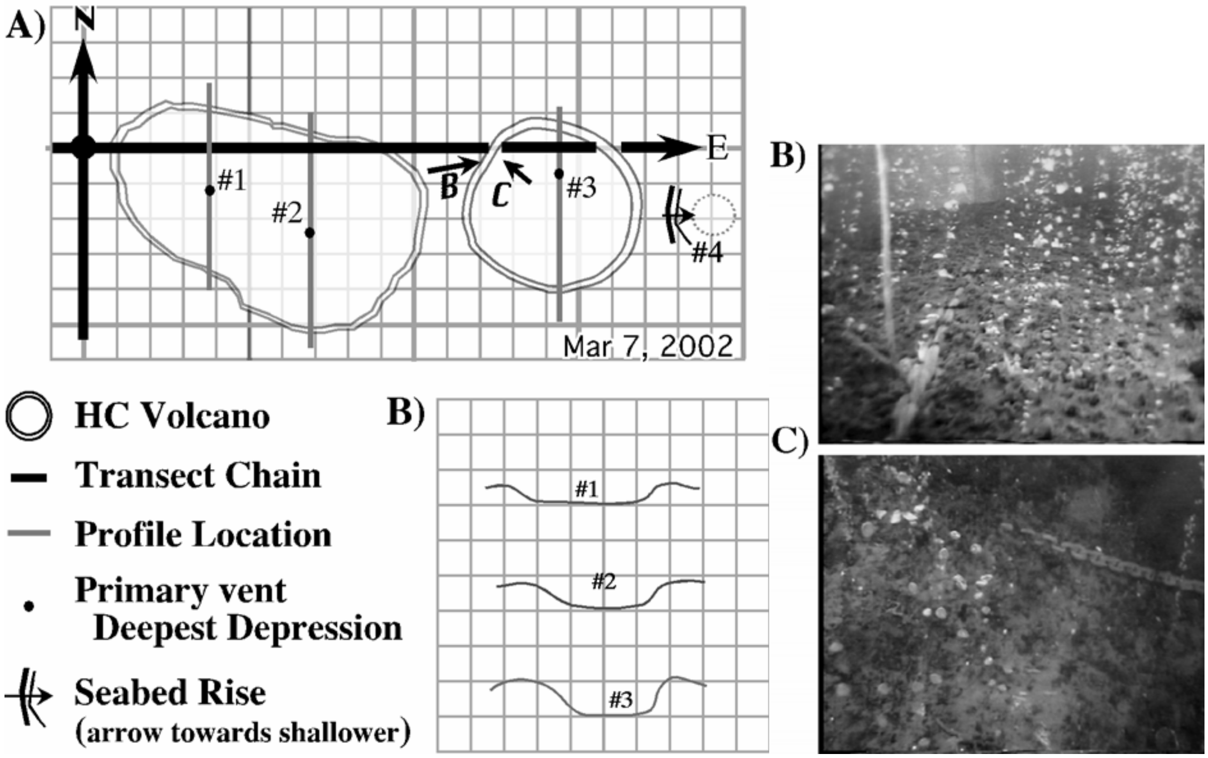

Figure III-18. Seabed map of central zone of Shane Seep area from survey Mar. 7, 2002. Symbols key below **A.** **B.** Hydrocarbon volcano profiles. Grid on **A.** and **B.** is one meter square. **C.** and **D.** Video captures from Mar. 8, 2002 survey showing penetration of transect chain into hydrocarbon (HC) volcano walls. Positions and view angles of **C.** and **D.** shown by labeled arrows on **A**. **A** is from *Leifer et al.* (2004).

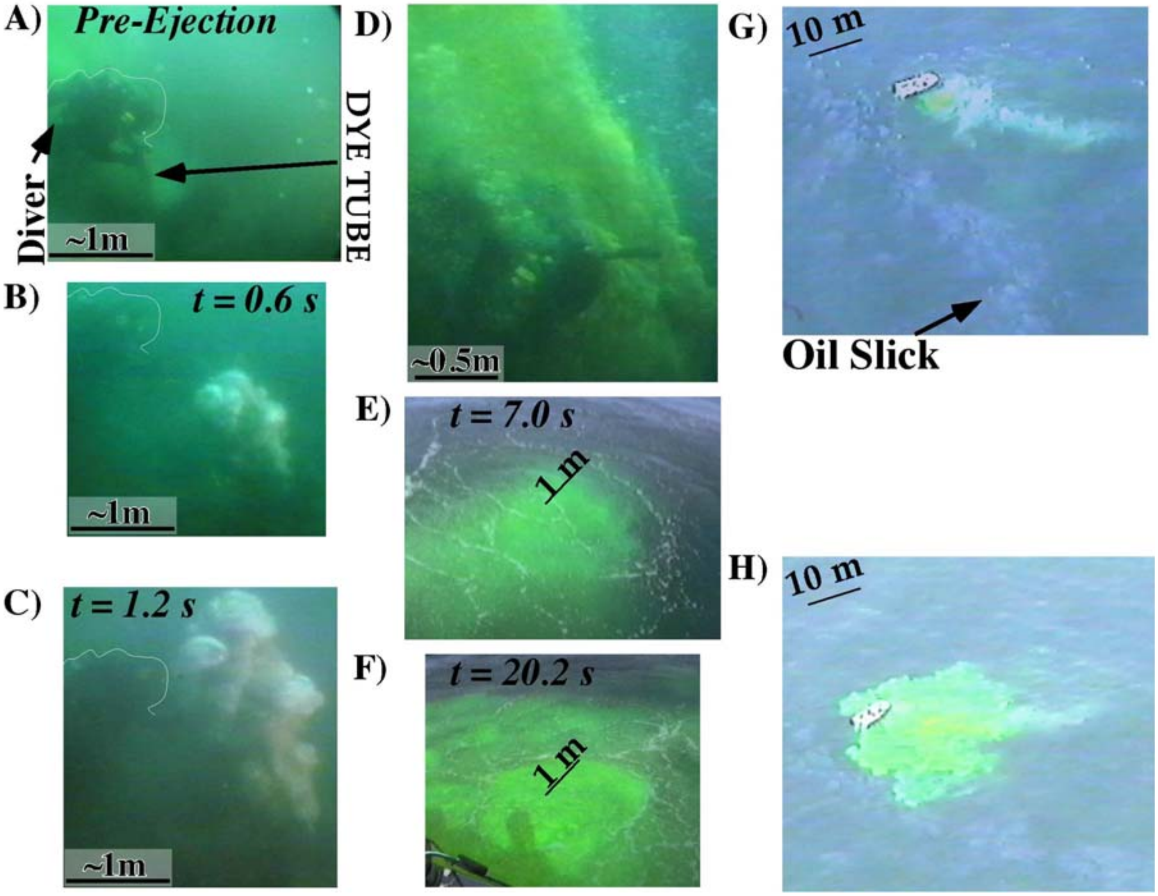

Figure III-19. Video captures of large gas ejection at Shane Seep during a dye injection experiment. Before the ejection **(A)** seepage was quiescent. Blowout **(B)** bubble streams rose and grew rapidly **(C)**. Seconds later the diver (outlined in white) injected dye (**D**) which first reached the sea surface 7 s later. Most of the dye arrived slightly later **(E).** Overflight images show initial arrival **(G)** and after tens of seconds. Times relative to blowout and size scale on figure**.**

On March 8, 2002, SCUBA divers and videographers were at Shane Seep to measure the bubble plume's upwelling flow by introducing fluorescein dye into the bubble stream at the seabed. A diver communication system allows onboard scientists to record the dye arrival time at the sea surface and thus the fluid upwelling velocity, V_{up}. Video cameras were at the seabed, 5 m above the seabed, shipboard, and in an airplane. A test dye release at 0845 Local Time (LT), yielded a 50-s transit time – V_{up}~45 cm s^{-1}, comparable to previous values Clark *et al.*, (2003). Ten minutes before the airplane's arrival, divers reported that seabed seepage at the main HC volcano had virtually ceased (Figure III-19A). At 0936 LT a large gas ejection occurred at the seabed (Figures III-19B & III-19C). Suddenly, three separate gas streams arose from the seabed, described by the divers as sounding like a freight train (Shane Anderson, UCSB, pers. comm., 2002). The leading bubbles expanded very rapidly so that by 5 m above the seabed the bubbles were several meters in diameter. Dye introduced into the bubble flow at the seabed a few seconds after the blowout (Figure III-19D) first was observed at the sea surface 7 s later (Figure III-19E) – peak V_{up} ~ 300 cm s^{-1}, although the main mass of dye arrived 10 s after dye injection – V_{up} ~ 200 cm s^{-1}. Bubble plumes lift deeper, cooler water, which at the seasurface formed a divergent surface outwelling flow. This outwelling flow which is cooler and thus denser then sinks. The outwelling flow is a perennial feature of Shane Seep; however, after the blow-out, the area of outwelling flow rapidly expanded during the ejection (Figure III-19G & III-19H). Overflight images clearly show the dyed bubble stream throughout the water column, tilted by the currents (Figures III-19I & III-19J). Meanwhile at the seabed, tar pieces “rained” down between the videographer and vents, i.e., in the area of the volcano walls. Meanwhile at the seabed, tar pieces settled between the divers and vents in the area of the volcano walls. After several minutes, the flux slowly decreased until seabed video showed a return to approximately normal, both for the main vents and the surrounding smaller vents.

The wind direction was on-shore and towards WCS during the period of the ejection and the CH_4 plume from the ejection was detected at WCS at precisely the time predicted based on the wind speed. Total hydrocarbon (THC) levels were elevated an average 1.05 ppm above background for 6 minutes before returning to normal.

The mean wind speed, u_{10}, from 0930 to 0950 LT was 1.57±0.15 m s^{-1}, yielding an advection time of 15.8±1.6 min, for predicted arrival at 0952 LT. The recorded total hydrocarbon (THC) (Figure III-20) shows a THC pulse arriving at 0952 LT. THC levels were elevated an average 1.05 ppm above background for 6 minutes. Background was defined as the mean THC from 0935 to 0945 LT and was 2.28 ppm. At 1000 LT, the wind began shifting southwards. From 1010 to 1020 LT, a plume from the Seep Tent Seep area (195° - 3.6 km) was advected over WCS. Although more distant, normal emissions from the Seep Tent seep area (at 195°, 3.6 km from WCS), and THC levels at WCS in the plume, are an order of magnitude greater than from Shane Seep.

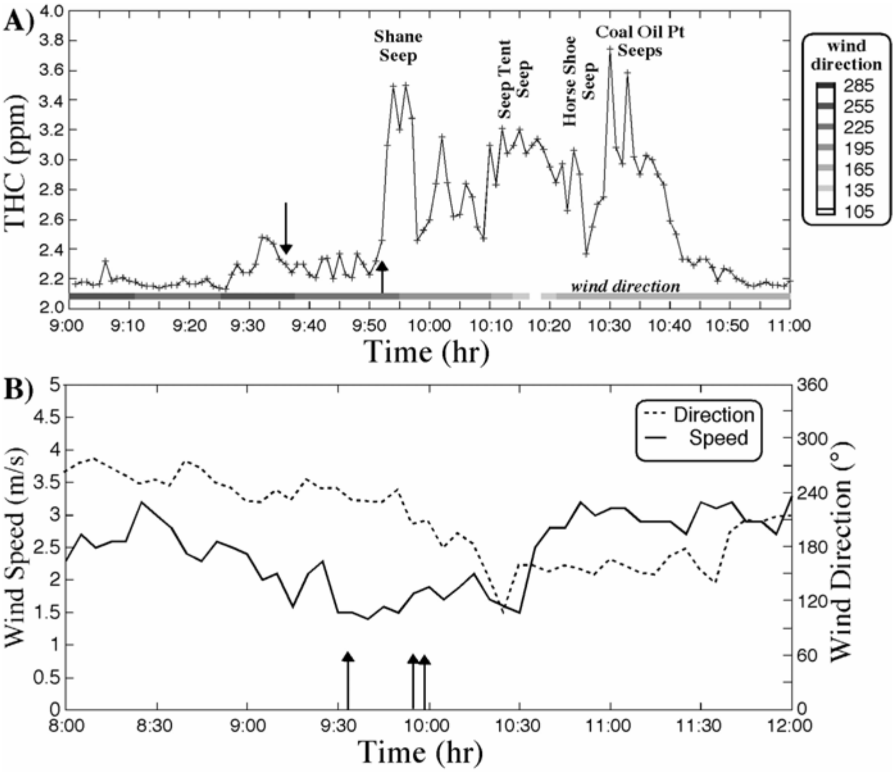

Figure III-20. West campus air pollution station (WCS) measurements of total hydrocarbon (THC) for Mar. 8, 2002 and **B),** WCS wind direction data for same day. Grayscale bar on **A)** shows wind direction.

Source strength, Q (m^3 s^{-1}), was back-calculated from the WCS THC data using a Gaussian plume model (*Hanna et al.*, 1982). We assumed the 10-m wind speed, u_{10}, wind direction, θ, and atmospheric stability were constant between Shane Seep and WCS and that wind-veering was negligible given the proximity of WCS to the shoreline and lack of significant topographic features in the vicinity – WCS is 6 m above sea level. For this clear morning, two atmospheric stability cases were simulated, “Briggs Turbulence” for slightly unstable conditions with $2 < u_{10} < 3$ m s^{-1} and surface roughness typical of the ocean at these wind speeds for light sun (Case 1) or for moderate sun (Case 2).

For Case 1 and elevation of THC levels by 1.05 ppm above background at WCS, $Q = 0.52$ m^3 s^{-1} (Figure III-20). Sensitivity to θ was tested by calculating Q for $\theta = 226, 232°$ with variability based on the ±3° accuracy of anemometer (Model 020C, Met One Instr., OR). For $\theta = 226°$ and 232°, Q was 0.56 and 0.52 m^3 s^{-1}, respectively. Sensitivity is small because the wind was almost directly towards WCS. For Case 2, $Q = 0.235$ m^3 s^{-1}, with a similar small sensitivity to θ. Sensitivity to u for a Gaussian plume is linear (for constant stability class), thus uncertainty in Q from u was ~10%. The main uncertainty was associated with stability class – i.e., Case 1 versus Case 2. For the entire blowout event, the total emission, Q_{tot}, was ~160 m^3 or ~70 m^3, for Cases 1 and 2, respectively. In this study, the average Q from the two cases ($Q = 0.4$ m^3 s^{-1} ±25%, or ~120 m^3 for the entire event) is used.

This Q is comparable to the output of the entire seep field, $Q = 1.15$ m^3 s^{-1} (Hornafius *et al.* 1999) and was 10 to 15 times the normal Shane Seep Q of 0.038 m^3 s^{-1} (Washburn *et al.* 2005). Thus, for the entire event, ~120 m^3 of methane escaped at the sea surface. Due to bubble dissolution, Q (in moles) at the seabed must have been larger than at the sea surface. While large, compared to the field, the emission rate was not significant. However, a numerical study described in Section V showed greatly reduced gas loss to the water column for the blowout due to plume processes, specifically. Thus, the model study showed that the true significance of the event was that plume processes enhanced enormously CH_4 transport to the sea surface.

For hydrocarbon seeps, blowouts likely are caused by tar blockage of seep vents (Leifer and Boles, 2005a); Hovland, 2002). A tar block at the main vent would explain the decrease and then absence of seepage prior to the ejection. We propose that for this event, the ejection resulted from an increase in pressure behind the blockage until the passage was blown free. For this mechanism, the ejection size (for the same vent and tar blockage) would be similar at greater depths since it is a differential pressure across the blockage that creates the ejection (Leifer *et al.*, 2005a). During this event, a small amount of tar pieces were observed raining down onto the HC volcano walls, suggesting that burial of the chain here is explained by multiple blowout events. Seafloor pockmarks, or a concave crater-like depression that commonly occurs on muddy seabeds are common seepage-related features on all continental shelves. Pockmarks are proposed to result from an explosive formation process (Hovland, 2002), although likely due to other factors than tar. If the proposed pockmark-formation mechanism is similar to our observations, – blowout emissions and deposition – then blowout seepage may be common and a potentially important seepage process. Blowout seepage has greater potential to contribute to atmospheric budgets than low flux seepage due to bubble-plume processes, discussed below. These processes can significantly enhance the efficiency of bubble-mediated transport across the water column.

IV. NUMERICAL BUBBLE STUDIES

An existing bubble propagation model described in Leifer and Patro (2002) and Leifer and Judd (2002) was applied to the hydrocarbon seeps in the Santa Barbara Channel. This model has been used for sensitivity studies on data collected in the Santa Barbara Channel, as well as seep bubbles in the Gulf of Mexico (Leifer and MacDonald, 2003; MacDonald *et al.*, 2002) and North Channel (Leifer and Judd, 2002).

IV-1. Theoretical Description of a Bubble

The model solves the differential equations describing bubble behavior. The bubble dissolution rate is equivalent to a mass flux (F_M) and is

$$F_M = \frac{\partial n}{\partial t} = Ak_B \Delta C = 4\pi r^2 k_B(r, \mathbf{D}(T))(C - P_B / H(T)) \qquad (4)$$

where n is the number of moles in the bubble, t is time, A is the bubble surface area, r is the bubble equivalent spherical radius, k_B is the bubble gas transfer rate, C is the aqueous concentration, ΔC is the concentration difference between the gas and liquid phases, **D** is the gas diffusivity, P_B is the bubble pressure which is primarily the hydrostatic pressure, P_H, with a small contribution from surface tension ($2\sigma/r$). k_B is a function of r and **D**. H is the Henry's Law constant (mol cm^{-3} Atm^{-1}) that describes the equilibrium between the dissolved and gaseous phases (Sanders, 2005). Both H and **D** are temperature, T, dependent. Note, H is now defined as the inverse of Leifer and Patro (2002) and Leifer and Judd (2002).

From (4), ΔC is the driving force behind bubble gas outflow and depends upon the gas solubility as expressed by H. Thus, changes in solubility from temperature have a direct effect on the bubble dissolution rate.

As the bubble dissolves, it shrinks, although as it rises, it grows from the decreasing hydrostatic pressure. The size change of the bubble, is described by,

$$\frac{\partial r}{\partial t} = \left\{ \mathbf{R}T\frac{\partial N}{\partial t} - \frac{4\pi r^3}{3}\rho_W g \frac{\partial z}{\partial t} \right\} \left\{ 4\pi r^2 \left(P_A + \rho_W g z + \frac{2\sigma}{r}\right) - \frac{4\pi r^3}{3}\frac{2\sigma}{r^2} \right\}^{-1} \tag{5}$$

where **R** is the universal gas constant, ρ_W is the density of water, g is the gravitational constant, and z is depth. If a factor q is defined from the ideal gas law that converts moles into atmospheres, where $q = \mathbf{R}T/V$, where V is volume, (5) can be rearranged to yield:

$$\frac{\partial r}{\partial t} = r\left\{ q\frac{\partial N}{\partial t} - \rho_W g \frac{\partial z}{\partial t} \right\} \left\{ 3(P_A + \rho_W g z) + 4\sigma / r \right\}^{-1} \tag{6}$$

Whether a bubble grows or shrinks depends upon the numerator of (6). Also needed is the differential equation describing the change in pressure within the bubble,

$$\frac{\partial P_B}{\partial t} = -\frac{3P_B}{r}\frac{\partial r}{\partial t} + q\frac{\partial n}{\partial t} \tag{7}$$

As the bubble rises, P_H decreases, ΔC decreases and the mass flux from the bubble decreases. Bubbles rise at their stagnant rise velocity, V_B, relative to the surrounding fluid, which in a bubble plume is typically moving upwards due to drag from the rising bubbles with an upwelling flow, V_{UP},. Thus, the bubble depth, z, is described by:

$$\frac{\partial z}{\partial t} = -V_B + V_F \tag{8}$$

The upwelling flow decreases the time for bubbles to reach the surface, as well as increasing $\partial P_H / \partial t$. For most seep bubbles (r~1000 to 3000 μm), V_B is 20 - 30 cm s^{-1}. Upwelling flows have been documented in various seepage systems from large plumes spanning up to tens of meters (Leifer *et al.*, 2000; Clark *et al.*, 2003) to bubble streams arising from a single vent (Leifer and MacDonald, 2003; Leifer and Boles, 2005a).

Although both k_B and V_B are parameterized in terms of r, in reality they are determined by the detailed hydrodynamic flow around the bubble. This flow is strongly affected by bubble buoyancy, i.e., r. However, anything that affects the bubble surface state, such as surface active substances, surfactants, affects the hydrodynamics and thus k_B and V_B. Contaminated bubbles have immobile surfaces and which cause them to exchange gas slower and rise slower than clean bubbles, which have mobile interfaces. Outside the laboratory, bubbles always have some contamination, which is pushed towards the downstream hemisphere by the flow, thus bubbles typically have partially immobilized surfaces. However, unless the immobile portion of the bubble's interface extends far enough from the bubble's downstream pole – 45° (Sadhal and Johnson, 1983) – it has negligible effect on the bubble's behavior and the bubble behaves clean. The result is that for a given contamination, bubbles larger than a transition radius behave clean, while smaller bubbles behave dirty with a transition between the two cases. Patro *et al.* (2002) found this transition occurred at approximately $r \sim 500 - 700$ µm.

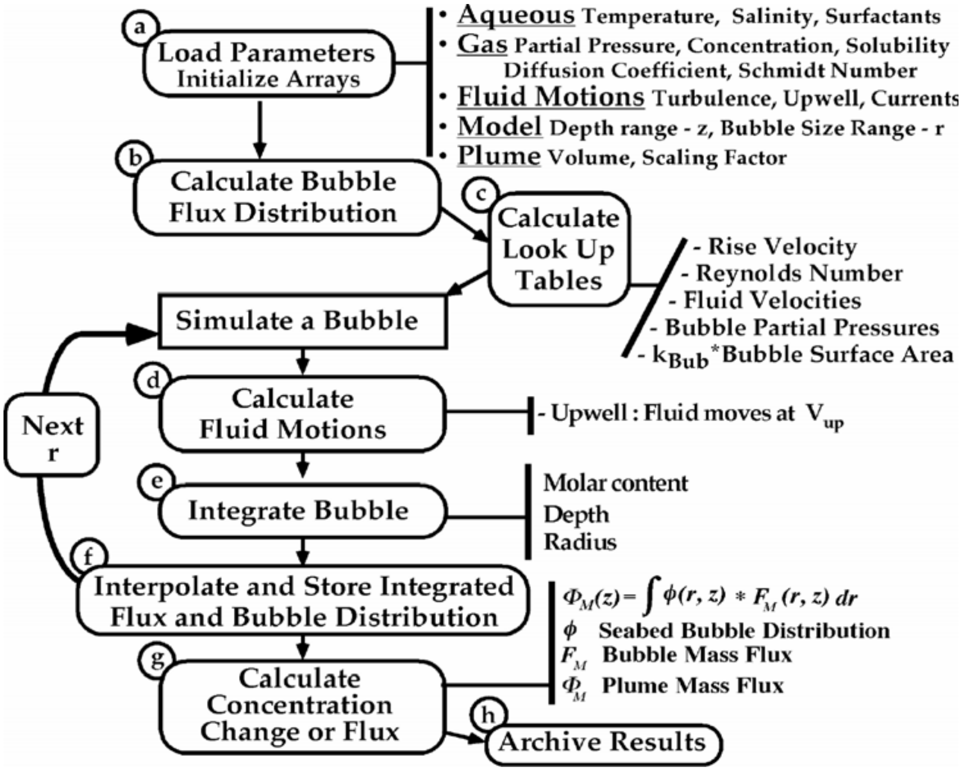

Figure IV-1. Flowchart of the numerical bubble model. From (Leifer and Judd, 2002)

IV-2. Numerical Bubble Model Overview

A model flowchart is shown in Figure IV-1. Initially, physical, fluid dynamical, plume, and chemical parameters are loaded. Next, the seabed bubble emission flux distribution, $\phi(r)$, is calculated from the observed $V_B(r)$ and the bubble emission size distribution - i.e., Figure III-5. Where feasible, look-up tables are used for computational speed, including parameterizations for k_{Bub} and V_B, and upwelling profiles. Bubbles in each size class are simulated including an imposed upwelling flow, V_{up}. Each bubble size class is initialized at the sea floor with observed partial pressures and allowed to rise due to buoyancy and upwelling flows. The model solves the coupled differential equations describing the change in moles gas, n, r, bubble pressure, P_B, and depth, z, as a bubble rises, exchanges gases, and changes in size due to gas exchange and decreasing P_H. Numerical integration is by a third-fourth order Runge-Kutta routine with variable step size and is terminated when the bubble reaches the surface or dissolves to 5-µm radius. Then the output for each size class is interpolated to a smooth depth grid. The gas flux (methane, alkanes) for the plume into the water column and vertically in the bubbles at each depth is calculated from the mass flux integrated over the bubble emission flux at each depth. Each bubbles size class is individually simulated and is combined with the size flux distribution (i.e., the number of bubbles of each size emitted per second) to calculate total flux of each gas. Gas in the bubbles at the sea-surface is the flux to the atmosphere.

Bubble model predictions are strongly influenced by the rise speed, V_B, and gas transfer, k_{Bub}, parameterizations, which are strongly dependent upon bubble size, oiliness, and water temperature. Parameterizations are based upon a combination of field observations, laboratory experiments, and best estimates from the literature. Gas kinetics (solubilities and diffusivities) are based on the literature (e.g., Waninkhof, 1992; Sander, 2000), although several are unreported and thus estimated values are used (based on theoretical calculations – Sander, 2000).

Regarding fluid motions, the model allows specification of a 2D flow field which can include complex motion generated by the rising bubbles (upwelling flow), waves orbital motions, turbulence, and Langmuir cells. Currently, the model is not fully 2D; bubbles are assumed to originate from a single source, and can move in 2D due to the flow field; however, the 2D position and gas fluxes are not stored; model output consists of only the overall gas fluxes at each depth.

A bubble tends to grow due to air inflow and changes in hydrostatic pressure while it tends to dissolve due to outflow of CH_4 and other hydrocarbons. Whether the bubble dissolves or not depends upon the balance between these two processes. Because oil collects at the bubbles' gas-water interface and is entrained in the upwelling flow, the model can calculate the oil flux and whether or not the oil is “deposited” in subsurface layers.

IV-2-1. Single Bubble Studies

Simulations were run for surfactant-contaminated bubbles rising from 22 m (e.g., Shane Seep), and 13°C using the gas composition for the Seep Tent at the seabed (Table III-3) where all trace n-alkanes are simulated at ethane (11.6 %), thus the air gases are trace. For the first simulations, bubbles were clean, dissolved methane was trace (~1/250 saturation) and there was no upwelling flow.

Simulation output for a clean r = 5000 µm bubble is shown in Figure IV-2. As the bubble rises, methane escapes while atmospheric gases enter, so that by the surface, approximately 86% of the methane has been lost, although this bubble is still ~40% methane (Figure IV-2A).

Thus the change in bubble composition at the sea-surface as compared with at the seabed does not indicate how much methane has been lost, because the bubble size also changes. This can be understood by a simple conceptual model in which we assume that in our system there is only methane. In this case, the bubble would have lost most of its methane to the surrounding ocean, but we would still be pure methane (since there is no air to enter the bubble). Also note that ethane, representative of the trace n-alkane gases, becomes enhanced in the bubble relative to methane due to its lower diffusivity.

For the first 60 seconds of its rise (~10 m), the bubble shrinks (Figure IV-2D) due to the rapid outflow of methane faster than its growth due to hydrostatic pressure (Figure IV-2B). For the rest of its rise, it grows as the air inflow and hydrostatic pressure become more significant than the (slowing) outflow of methane. At ~100 seconds (Figure IV-2D) the bubble arrives at the sea surface, only slightly smaller than when it left the seabed (Figure IV-2C).

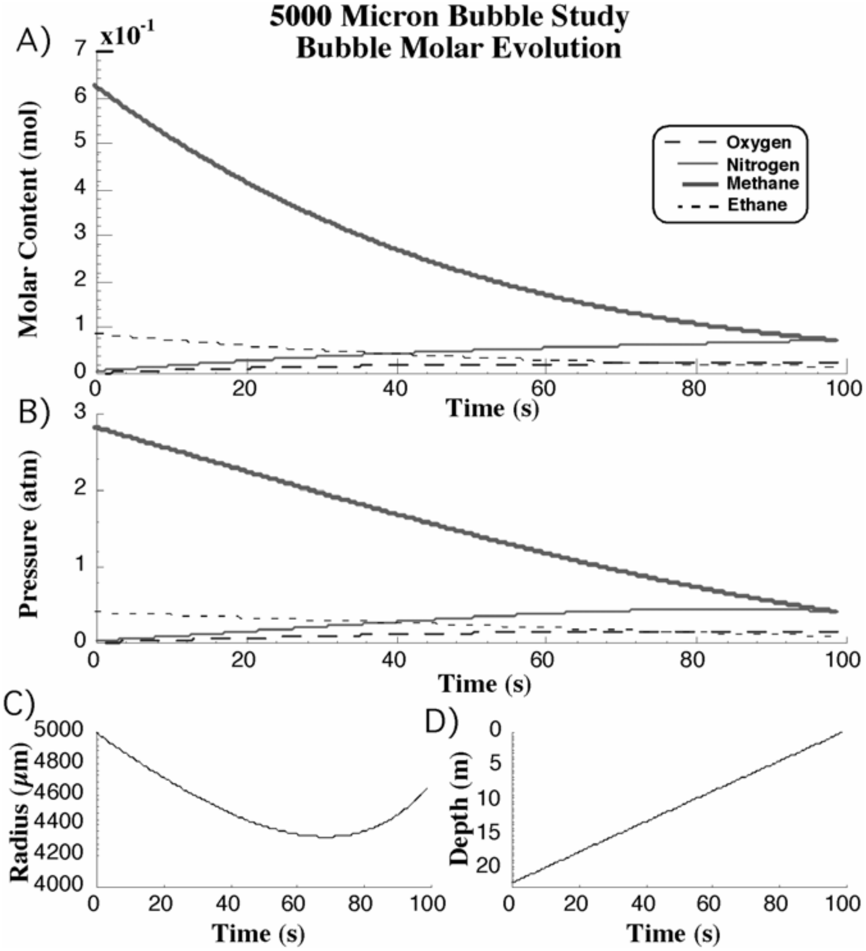

Figure IV-2. Numerical simulation of a clean, r = 5000 μm bubble in 13°C water with trace dissolved methane and no upwelling flow. A) shows molar evolution, B) shows partial pressure evolution, C) shows radius evolution, and D) shows depth evolution.

Unlike the 5000 μm, which makes it to the surface with most of its methane intact, a 500-μm radius bubble, shown in Figure IV-3, dissolves after rising only a few meters (Figure IV-3D).

While the methane and ethane outflow the bubble, air gases inflow, becoming the dominant gases at ~7 s (Figure IV-3B). As a result, the dissolution rate (i.e., decrease in radius with time) slows down (Figure IV-3C). Methane continues to outflow until it becomes a trace gas at ~12 s; thereafter, it no linger affects bubble size. Meanwhile the inflow of air gases has also nearly ceased (12 s), since they are roughly in equilibrium with dissolved gases in the surrounding water. However, since the bubble is now less than 100 µm, surface tension begins to play a role, causing all gases to outflow. The effect of surface tension becomes apparent towards the end of the bubble's life, when the bubble pressure begins to rise (Figure IV-3B). The simulation was terminated at 28 s since the bubble does not significantly rise any further.

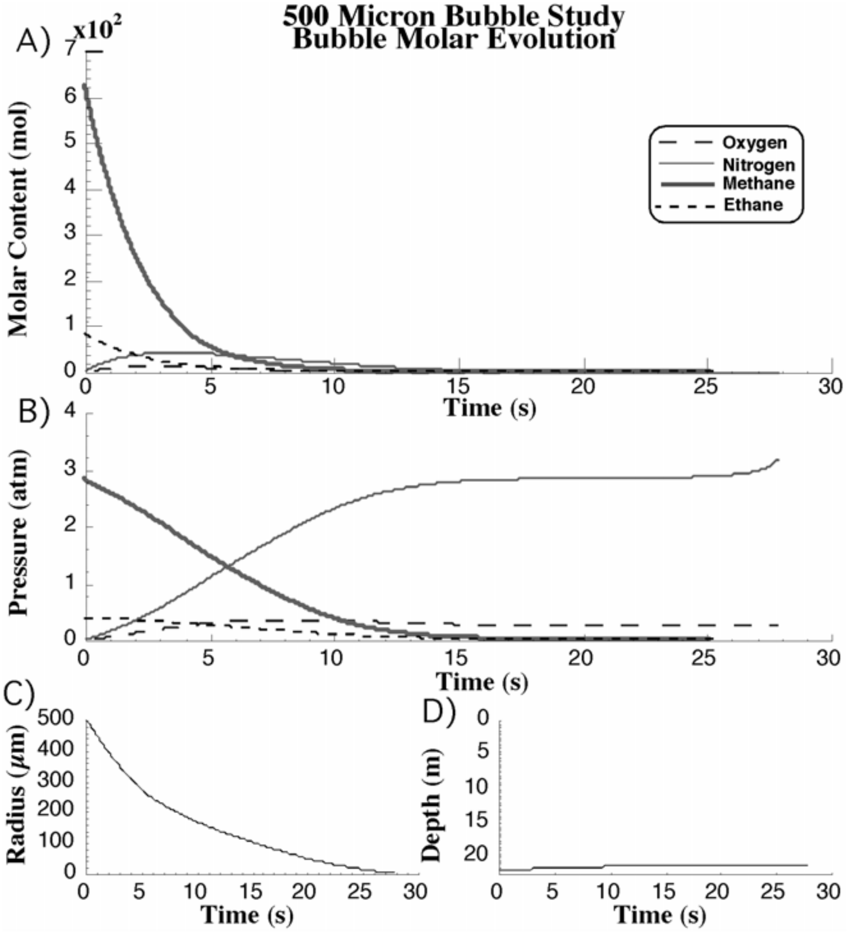

Figure IV-3. Numerical simulation of a clean, r = 500 µm bubble in 13°C water with trace dissolved methane and no upwelling flow. A) shows molar evolution, B) shows partial pressure evolution, C) shows radius evolution, and D) shows depth evolution.

IV-2-2. Contamination

Smaller bubbles dissolve even faster; however, given that these bubbles are oil coated and in the ocean, it is likely that bubbles are contaminated to some extent by surface-active substances - surfactants. Patro *et al*. (2002) showed that for seawater, large bubbles behaved clean, while small bubbles behaved dirty. In seawater, the transition was at 500 µm and was sharp, in lagoon water, the transition was broad, with bubbles 2200 µm and larger behaving clean.

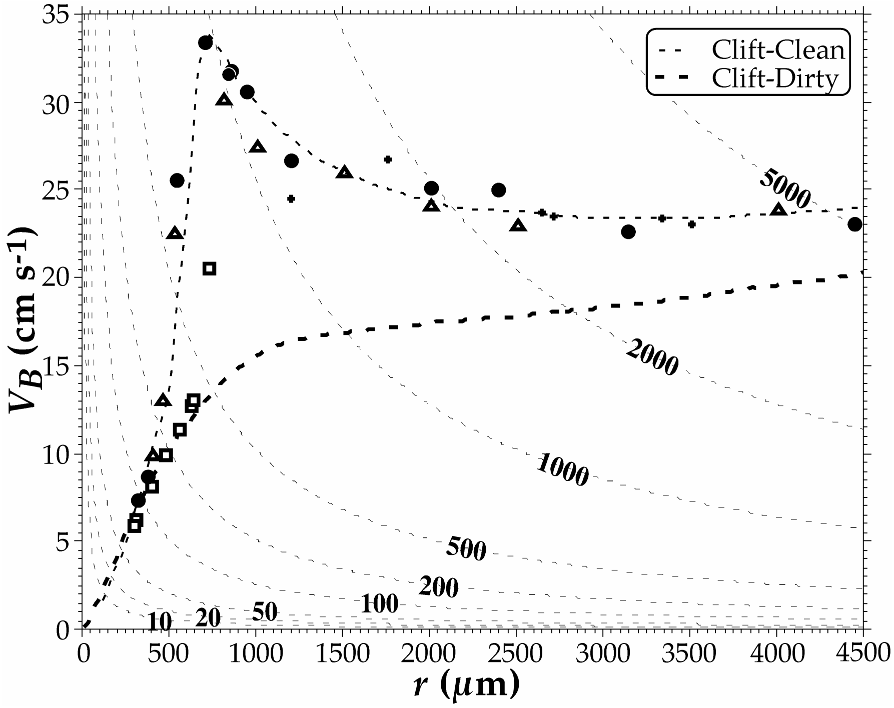

Figure IV-4. Rise velocity, V_B, parameterizations for clean and dirty bubbles as a function or radius, r. Also shown are some experimental laboratory data, and contours of Reynolds number. From Leifer and Patro (2002).

Whether bubbles are clean or dirty can be significant, as shown in the parameterization for clean and dirty bubbles in Figure IV-4. For example, if the same 500-µm radius bubble simulated in Figure IV-3 was dirty, it would reach the surface. Although surfactants decrease bubble rise speed, and thus increase the time to transit the water column, they have an even larger effect on gas exchange. The bubble still reaches the surface with trace methane, but it does reach the surface. For comparison, the clean simulation results (Figure IV-3) are shown by dashed lines in Figures IV-5b and IV-5c. By 250 s, the bubble begins growing again due to decreasing hydrostatic pressure, since the air gases are close to equilibrium.

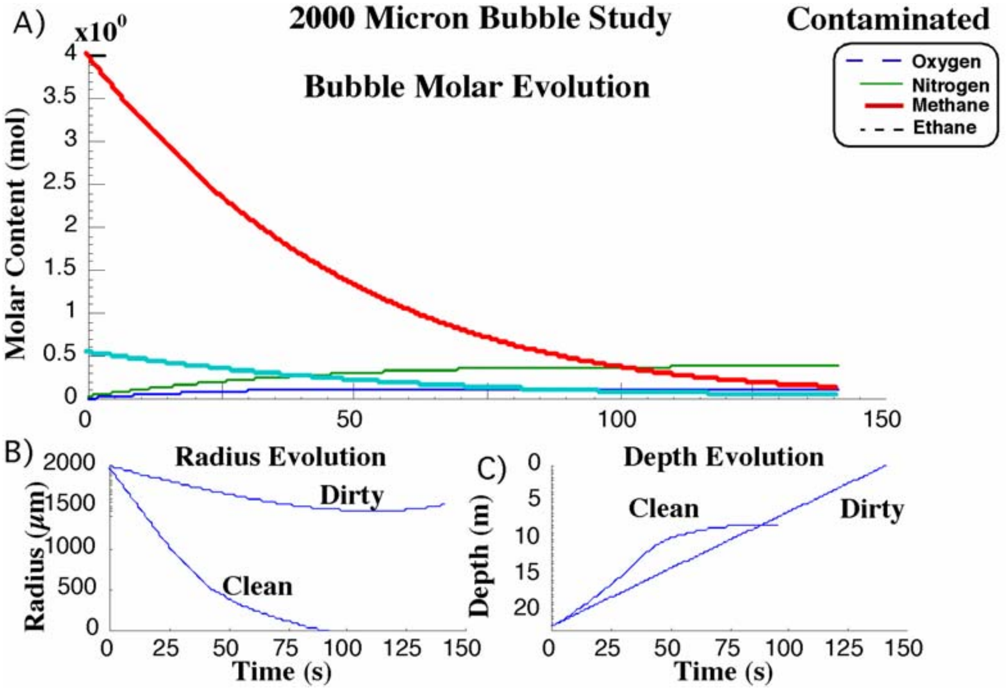

Figure IV-5. Numerical simulation of a dirty, r = 2000-μm bubble in 13°C water with trace dissolved methane and no upwelling flow. A) shows molar evolution, B) shows partial pressure evolution, C) shows radius evolutions for dirty and clean, and D) shows dirty and clean depth evolutions. Data key on figure.

Clearly, correctly describing surface state is important. Unfortunately, published descriptions of the effect of oil on bubble behavior are unavailable. Bubbles at Shane Seep have trace oil coatings and appear to in general, follow the dirty parameterization, with occasional very oily droplets that rise much slower and may have significantly lower gas transfer rates. Their fate likely will be very different from similar-sized bubbles. While it is clear that small bubbles behave contaminated, and it is likely that the largest bubbles behave clean, the transition is uncertain. For the remaining simulations, we assume (conservatively) that trace oil contamination has no effect beyond that of seawater surfactants (largely algal exudates) with a transition at r ~ 700 μm as suggested in Patro *et al.* (2002).

IV-2-3. Upwelling Flow

When bubbles are in a plume, they modify their environment including creating an upwelling flow (Leifer *et al*., 2000a). This flow enhances bubble-mediated gas transport by decreasing the transit time to the sea surface, but also by increasing the rate that the hydrostatic pressure decreases. It is the concentration difference that drives gas transfer, thus a more rapid process in the hydrostatic pressure means the bubble reaches shallower depths where mass loss is slower with more of its original gases.

IV-3. Sensitivity studies

Using this model, sensitivity of bubble-mediated CH_4 transport to ambient conditions was studied. Strong sensitivities to aqueous CH_4 saturation, upwelling flows (Leifer and Patro

2002), and oil contamination were identified. Field data collected as part of the current MMS project discovered and quantified these parameters (Leifer *et al.* 2000a; Leifer and Clark 2002; Clark *et al.* 2003).

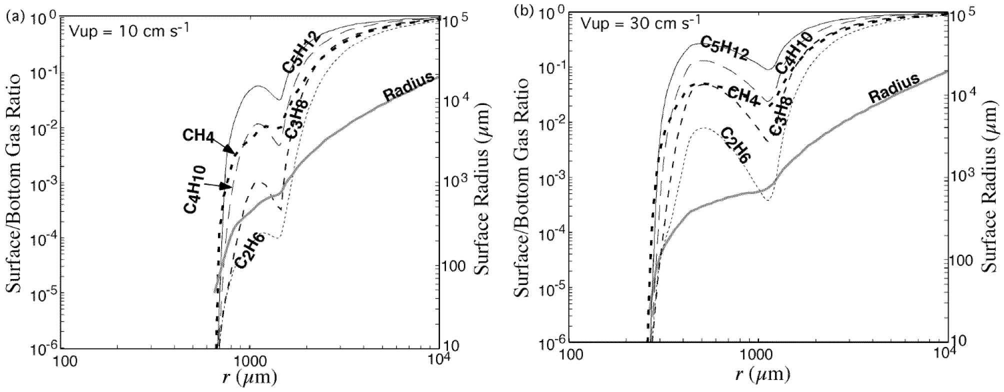

Figure IV-6. Sensitivity results showing predicted ratio of bubble alkane molar content at surface to sea floor versus initial bubble radius, *r* for (a) upwelling flow, V_{up}, of 10 cm s^{-1}, and (b) 30 cm s^{-1}. Also shown is the surface *r* on the right vertical axis. Data key on plot.

The model investigated alkane transport to the surface for La Goleta Seep (34° 52.44' N, 119° 23.65' W), for two upwelling flows, V_{up} = 10 and 30 cm/s. Dissolved CH_4 was 0.9 Atm, small bubbles were assumed contaminated, large bubbles clean. The predicted surface *r* is shown in Figure IV-6. For V_{up} = 10 cm s^{-1} (Figure IV-6a), a 2000-μm bubble reaches the surface with *r* ~ 2000 μm, while a 900-μm bubble reaches the surface with *r* ~ 300 μm. Stronger upwelling (Figure IV-6b) causes less bubble dissolution (bubbles are subsurface for a shorter time). These two sensitivity studies show a strong sensitivity of bubble survivability to V_{up}. In one scenario a 500-μm bubble dissolves, depositing its oil subsurface. In the other, it doesn't.

Also shown in Figure IV-6 is the surface to bottom ratios for alkanes to pentane. For all bubbles, the ratio increases with alkane number, except for CH_4, which behaves differently due to its saturation of the water column. The relative enhancement of heavier versus lighter alkanes is greatest for bubbles that dissolved slightly, and least for the largest bubbles (which grow). For the largest bubbles this results from the large volume, i.e., during their ascent to the surface, gas exchange changes the bubble's total mass little. In contrast, when a bubble dissolves, as indicated by a large decrease in CH_4 (e.g., $r<800$ μm), all gases are equally forced from the bubble, and thus there is little enhancement of heavier alkanes. As a result, only a narrow size range can explain observed alkane enhancements (i.e., minor vent bubble plumes). In fact, circa 3000-μm bubbles produce a relative enhancement of 2 for pentane versus ethane. For these conditions, bubbles with initial *r* ~ 3000 μm must be responsible for most of the gas transport in the plume. Since these bubbles grow only slightly, this agrees with observed surface bubble distribution for La Goleta Seep.

IV-4. Plume Simulations

Given the emission size distribution of bubbles in a plume, the numerical model can simulate the mass flux for all the bubble size classes in the plume and calculate for each gas, the mass outflow as a function of depth and the vertical mass transport (i.e., bubble content) as a function of depth. Simulations were also used to address the impact of blow-out emissions. Simulations were conducted for three plumes, a minor, a major, and a blow-out plume, shown in Figure IV-7.

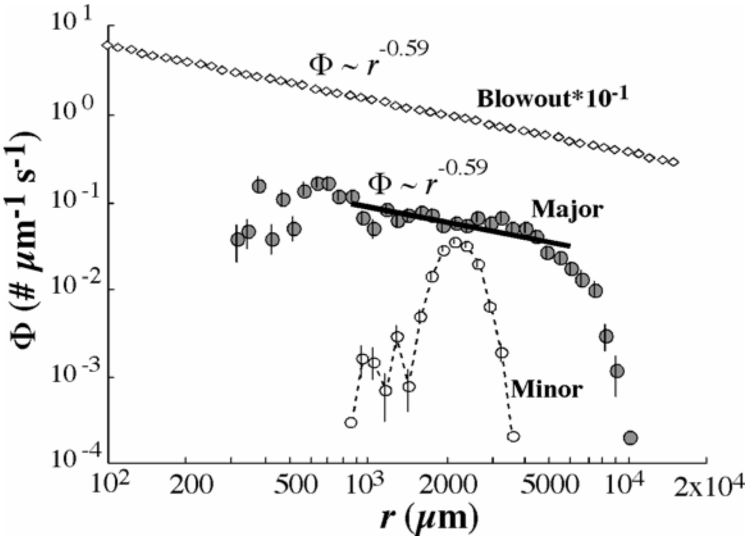

Figure IV-7. Bubble emission size-distributions, Φ, versus bubble radius, *r*, used in numerical simulations, for different seepage types. Case 1 is a minor plume (open circle), Case 2 is a major plume (filled circle), and Case 3 is for the blowout (diamond) with calculated values based on fit to Case 2 (diamond). Also shown is least squares fit to major plume over range of fit. Cases 1 and 2 from Leifer and Boles (2005).

Bubble plumes were a minor vent, a major vent, and a blowout vent (Figure IV-7; Table IV-1). Minor produce single streams of bubbles and have a narrow, peaked emission size-distribution, Φ. Φ is the number of bubbles in each size class (μm^{-1}) emitted per second in the entire plume. Laboratory (Blanchard and Syzdek 1977; Tsuge *et al.* 1981) and field (Leifer and MacDonald 2003; Leifer and Boles 2005a) observations indicate that low gas flux vents produced narrow, sharply peaked Φ, while high gas flux vents produce a broad and weakly size-dependent Φ, that extends to both very small and very large bubbles. The difference arises because at low flow, bubble size depends solely upon vent mouth geometry (Blanchard & Syzdek 1977) whereas at high flux, bubble fragmentation at the vent mouth creates the broad size distribution (Slauenwhite and Johnson 1999). Thus, for the blowout (Case 3), the functional dependency of Φ for the major vent was used for the blowout, $\Phi = A\, r^{-0.59}$, but the range of bubbles described by this power law was assumed to extend to a wider range, from 100 to 15000 μm. The value of *A* was chosen so that the total seabed volume flux was 0.5 m^{3} s^{-1} (at STP). The upper radius cut-off was based on qualitative observations of bubbles from the seabed video and assumes that bubbles larger than $r \sim 1.5$ cm, which were not seen at the sea surface, rapidly broke up and formed bubbles with $\Phi \sim r^{-0.59}$.

Bubbles were simulated as having a size-varying contamination (Patro *et al.*, 2002). For minor vent plumes, V_{up} was ~10 cm s^{-1} (Leifer and Boles, 2005a) while the main vent at Shane Seep was simulated for normal conditions with $V_{up} \sim 45$ cm s^{-1}. For the blowout simulation, the measured V_{up} of 200 cm s^{-1} was used.

At the seabed, the model was initialized with seep gas with a composition that was mostly CH_4 (84%) and CO_2 (12%), with trace air (2.21%), and n-alkanes decreasing from 3% ethane. N-alkanes larger than CH_4 were simulated as ethane with a mole fraction of 3%. Aqueous CH_4 was elevated several orders of magnitude above seep-field background and was only weakly depth dependent - 51.5 and 49.8 mMol L^{-1} at seabed and sea surface, respectively (Clark *et al.*, 2003). Simulations used an aqueous CH_4 value of 0.05 mMol L^{-1}. The water temperature was 14°C. To address the lack of water samples during the unanticipated event, a fourth case simulated a blowout with elevated plume CH_4 based on CH_4 dissolution from Case 3.

Table IV-1. Model-predicted bubble gas mole-fraction at the sea surface (1-m depth) and gas observations for Shane Seep main plume. Remaining bubble composition was higher n-alkanes.

Case	Bubble	CH_4 Flux (mmol s^{-1})	O_2 (%)	N_2 (%)	CH_4 (%)	CO_2 (%)	CH_4 loss (%)
1	Minor	0.19[a]	5.9	14.9	76.0	0.04	51.6
2	Major	9.3[a]	1.3	3.9	89.6	1.6	10.4
3	Blowout	2.1×10^4 [b]	0.44	2.1	84.8	9.4	1.108
4	Blowout-II	2.1×10^4 [b]	0.44	2.1	84.8	9.4	1.096
Sample gas at seabed			0.34	1.87	83	12	
Sampled gas at surface			**5.3**	**14**	**78**	**0.6**	

---

[a] measurements from (Leifer and Boles, 2005a); [b] derived from calculated *Q* for blowout.

As bubbles rise due to buoyancy and the upwelling flow, seep gases exchange with dissolved air in the water. For normal conditions, bubbles at the sea surface were observed to have CH_4 (78%), air (19.3%), and trace CO_2 (0.6%) and n-alkanes. Although CO_2 loss increases the CH_4 mole fraction, air inflow decreases the CH_4 mole fraction.

For the minor (Case 1) and major (Case 2) vent bubble plumes, the bubbles were 5% and 22% air at the sea surface, respectively (Table IV-1). CO_2 outflow was very fast, decreasing to just 0.04% and 1.6% at the sea surface, for the minor and major plumes, respectively. Mole fractions for the major and minor plumes “bracket” the observed sea-surface bubble-mole fractions. This is in agreement with the sea-surface gas collection method, which included bubbles from both the major vents and the numerous minor vents in the immediate vicinity of the main caldera. The major plume simulation better approximated the sea-surface CO2 -mole fractions than the minor plume simulation. This is to be expected, since bubble-mediated transport of soluble gases increases with size (Leifer and Patro, 2002) and the largest bubbles were exclusively found in the major plume. The minor plumes, though appear to be most important to overall gas transfer, in agreement with the results from Leifer and Clark (2003). Leifer and Clark (2003) ran simulations absent seabed gas composition and seabed bubble size-distributions. For the simulations, seep-tent gas composition was used. It was found that the ratio of n-alkanes in sea surface gas could only be explained if most of the gas was being transported by bubbles 2000 μm to 3000 μm radius, i.e., the minor bubble plumes.

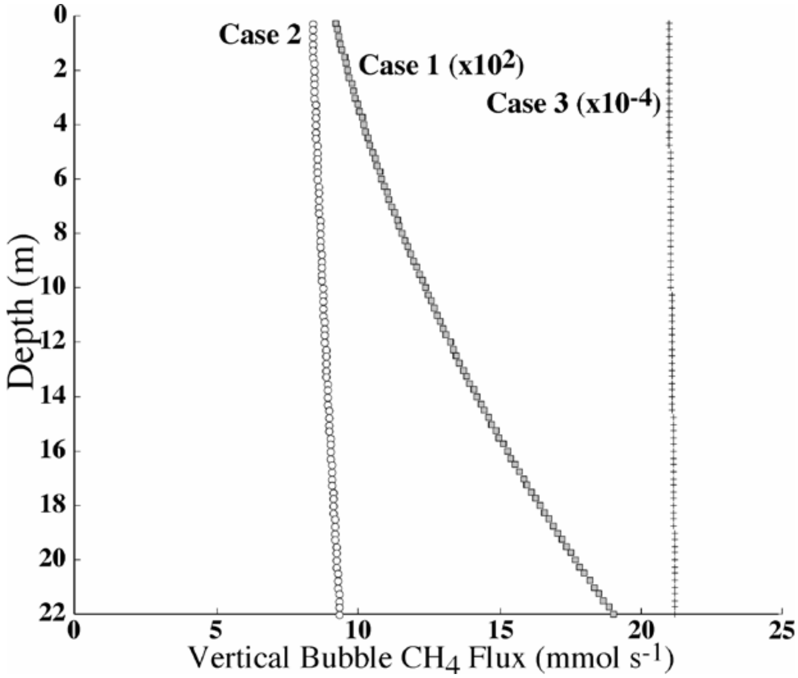

Figure IV-8. Predicted vertical CH_4 transport (in bubbles) for the three simulations. See Table 1 and text for details. Note, Cases 1 and 3 are multiplied by 10^2 and 10^{-4}, respectively

For the blowout simulation (Case 3), the predicted mole fraction of methane at the sea surface was less than for the major plume (Case 2). This is explained by the slower CO_2 outflow, i.e., the bubble retained more of its original CO_2 and thus the methane mole fraction was reduced. For the minor and major vents, 51.6% and 10.4%, respectively, of the original CH_4 dissolved (Figure IV-8), while for the blowout, CH_4 loss was just 1.108% or 0.23 mol s^{-1}. Air mole fractions were reduced due to the greater CO_2 and methane in the bubble and reduced air inflow into the bubbles.

The importance of elevated plume concentrations to bubble-mediated CH_4 transport was tested by using the dissolution flux for Case 3 to estimate dissolved plume CH_4. For the ~10 second transit of the water-column during the blowout, ~2.3 moles of CH_4 were predicted to have dissolved into the plume water. Based on the aerial overflight images, a conical blowout plume was assumed, 1-m diameter at the sea-surface (Figure III-19E) and 22-m tall - i.e., 23 m^3. If this plume remained unmixed with the surrounding bulk ocean, i.e., a conservative assumption, then plume CH_4 concentrations would have been elevated 0.1 mmol L^{-1} above normal plume concentrations. This estimate is conservative as it neglects plume loss to the bulk ocean. Using this elevated plume concentration, a simulation was run for a blowout and a plume CH_4 of 0.15 mmol L^{-1} (Case 4). All other conditions were as in Case 3. This simulation showed a very slight decrease in CH_4 loss to the water-column, 1.096% versus 1.108% for Case 3. The effect was small because 0.15 mmol L^{-1} CH_4 is ~5% of CH_4 saturation at 10 m

For a blowout from this very shallow seep, the primary factor enhancing CH_4 transport to the atmosphere was the rapid upwelling flow. There simply was insufficient time for the plume water to become significantly saturated. **For the blowout vent, a 10 cm s^{-1} Vup yielded CH4 loss of 6.8%, ~seven times the loss for Vup = 200 cm s^{-1}**. The presence of very large bubbles with their greater volume contributed significantly to methane transport, with bubbles larger than 5000 µm carrying **75%** of the methane. For deeper seeps, the CH_4 dissolution increases. Simulating the same blowout gas volume from 250-m depth - including compressibility- (Case 3) showed greater, but still small CH_4 loss, ~**8.6**% of the initial CH_4. Thus, if a seep blowout of comparable magnitude occurred at greater depths and generated similarly strong upwelling flows, potentially a significant fraction of its CH_4 can reach the atmosphere. For comparison, the major vent plume at 250 m (Case 2) lost ~69% of its original CH_4.

The model was highly illustrative that for blowout seepage, vertical methane transport efficiency is enhanced enormously. As a result, almost all of the methane from a shallow seep reaches the atmosphere. Furthermore, the model suggested that given sufficient ejection size and resultant upwelling flow and large bubble size, efficient transport of methane from the seabed to the sea surface is feasible from depths of many hundreds of meters.

V. DISCUSSION

V-1. Seabed Morphology Discussion

The seabed surveys demonstrate that seepage features at Shane Seep are both semi-permanent and “plastic.” The sediment overburden is Late Quaternary, and for the outer COP seep trends is thin, < 1 m. At Shane Seep the overburden is thicker, 2-3 meters (Fischer 1978), consisting primarily of very fine sand, and has modern total organic carbon of 1 - 2% (Fisher 1978). The sand overlies fractured Monterey formation basement. The upper 30 cm of sand is cemented by tar (La Montagne *et al.* 2003) and highly cohesive. The seabed near Shane Seep is also heavily coated with bacterial mats, and large tar balls can be found within the hydrocarbon (HC) or tar volcanoes. These volcanoes are termed hydrocarbon volcanoes rather than mud volcanoes because of their high tar content, which provides the necessary cohesion to form the volcano walls, and fixed vent locations.

That the walls represent a depositional process was dramatically demonstrated by the burying of the transect chain after it was draped across the newly formed volcano #3. Since elsewhere the chain, even two years later, lay on top of the sandy bottom, only a depositional process could explain the manner that the chain disappeared into the caldera's walls. Furthermore, the appearance of stones in the bottom of volcano #3 suggests that not only tar, but also sand was lofted during these events, leaving behind the rocks.

V-1-1. Seep Seabed Plasticity

There are several processes evidenced in the changes in seabed morphology over the years. These include deposition of tar from ejections along with the removal of seabed material during large ejection events, feature erosion and burial by storms, and the plastic deformation of the seabed. Vent locations remain fixed for a period of years but then re-express themselves nearby. While ejection events build up caldera walls they also destroy them. Together these changes provide strong evidence of the dynamic nature of hydrocarbon seeps.

During the formation of volcano #3, 100,000 kg of sediment was displaced. This most likely was due to either a single or a series of "explosive" events as indicated by highly circular caldera shape. And in general, when volcano walls grew higher, they also grew circularly (except for Vent #0). Meanwhile, much smaller ejections (but larger than that observed by the turbine tents) caught on video did not evidence any significant displacement of seabed sediment. Clearly the formation of volcano #3 was a large event (or series of events). The source of the event that precipitated the formation of volcano #3 could have occurred deep or shallow. If we assume shallow blockage responsible, it still must have been deep enough to stop the flow through both existing volcanoes #1 and #2. Otherwise pressure could not have built up behind them to then cause destruction of the ridge. Pressure behind the blockage would have increased until the blow through destroying the ridge separating the two vents. But this raises the question: How does an event that could destroy the ridge between volcanoes #1 and #2, despite their being highly active (i.e., open) vents, overcome the significantly greater resistance represented by the sediment displaced in the formation of volcano #3? Thus it is far more plausible that a deep event was responsible. In this case, a massive pulse of gas suddenly was released and traveled rapidly upwards through the fractures. At the seabed, the two existing vents were inadequate to flux the great volume of gas, and thus represented a bottle-neck behind which the pressure increased until it created a new pathway, volcano #3. The giant tar blocks found on volcano #3’s caldera floor must have been squeezed out through the fractures immediately under volcano #3, since similar tar blocks were not found in volcanoes #1 and #2. It is unclear from the observations whether the deep event was the clearance of a blockage in the fracture system or sudden access to the fracture system by a previously unconnected gas reservoir.

Tar does not necessarily migrate in punctuated transient events, for example there are beach tar oozes and forms mounds at the south edge of the Carpinteria State Park, CA. This tar seep is a long-term feature, having been used in boat making by indigenous peoples for centuries or longer (Earth Island Institute, 2003). Given sufficient pressure, tar migrates. And such pressure may explain the appearance of elevated seabed features such as the elevated plateau under volcano #4, or the ridges further to the east. Here, some of the fractures may be completely clogged with tar, implying an enormous pressure buildup to cause a blow through, which is unlikely (i.e., rare) to happen while gas can flow (and pressure be relieved) through other vents. In this case, the elevated pressure forces the tar to slowly ooze forwards, gradually lifting the sediment layer. Water flow may also be involved. And certainly the very gradual (over a year) formation of volcano #4 suggests a gradual process in sharp contrast to the sudden appearance of volcano #3.

The difference between volcanoes #3 and #4 was that volcano #4 formed gradually and included a raised mound. Not only did the plateau height gradually increase with time, but also the gas flux through the volcano #4’s vents and the size and height of its caldera walls. When first identified, volcano #4 was only a few centimeters tall with a few bubble streams. By 2003, the caldera was meters across, the walls were half a meter high, and there were many active vents. This is consistent with the tar slowly being forced from the fractures during the initial stages until the gas flux was sufficiently great (i.e., fractures were sufficiently opened) to allow the blow through mechanism to begin depositing the caldera walls.

In fact, the decrease in relative flux, and then impermanence of volcano #3 seen after March 2003, may relate to a large tar and or fluid flow clogging the vent. This is supported by the lifted seabed North of volcano #3 observed in April 2003, prior to the volcano's relocation to this area. Similarly, the expansion of volcano #4 between April and June, 2003, was preceded by a large (50 cm) increase in plateau height, noted in March 2003.

VI. BIBLIOGRAPHY

Allen, A.A., R.S. Schlueter, and P.G. Mikolaj, 1970. Natural oil seepage at Coal Oil Point, Santa Barbara, California. Science, **170**: 974-977

Asher, W.E., and P.J. Farley, 1995: Phase-Doppler anemometer measurement of bubble concentrations in laboratory-simulated breaking waves, *J. Geophys. Res.*, **100C**, 7045-7056

Baldy, S., and M. Bourgüel, 1987: Bubbles between the wave trough and wave crest levels. *J. Geophys. Res.*, **92C1**: 2919-2929

Blanchard D.C., Syzdek L.D. (1977). Production of air bubbles of a specified size. *Chem. Eng. Sci.*, **32**: 1109-1112

Boles JR, Clark JF, Leifer I, Washburn L (2001) Temporal variation in natural methane seep rate due to tides, Coal Oil Point area, California. *J. Geophys. Res.*, **106C11**, 27077-27086

Bowyer, P., 1992: The rise of bubbles in a glass tube and the spectrum of bubbles produced by a splash. *J. Mar. Res.*, **50:** 521-543

Clark, J.F., I. **Leifer**, L. Washburn, and B.P. Luyendyk, 2003. Compositional changes in natural gas bubble plumes: observations from the Coal Oil Point marine hydrocarbon seep field. *Geo. Mar Lett.* **23:** 187-193

Clark, J.F., Washburn L, Hornafius JS, Luyendyk BP, 2000. Dissolved hydrocarbon flux from natural marine seeps to the southern California Bight. *J. Geophys. Res.*, **105C5**, 11509-11522

Clester, S.M., J.S. Hornafius, J. Scepan, and J.E. Estes, 1996. Quantification of the relationship between natural gas seepage rates and surface oil volume in the Santa Barbara Channel, (abstract), *EOS (American Geophysical Union Transactions)* **77 (46):** F419

Clift, R., Grace, J. R. & Weber, M. E., 1978. Bubbles Drops and Particles. Academic Press, New York/New York.

De Leeuw, G., and L.H. Cohen, 1994: Measurements of oceanic bubble size distributions. OCEANS94, 13-16 September 1994, Brest, France, Proc. Vol. II, 694-699

Deane, G.B., and M.D. Stokes, 1999: Air entrainment processes and bubble size distributions in the surf zone. *J. Phys. Ocean.*, **29**, 1393-1403

Dickens, G.R., J.R. O'Niel, D.K. Rea, R.M. Owen, 1995, Dissociation of oceanic methane hydrate as a cause of the carbon isotope excursion at the end of the Paleocene, *Paleoceanography* **10**, 965-.

Dietz Jr., F.A. and K.F. Singley. 1979. Determination of Chlorinated hydrocarbons in water by headspace gas chromatography. *Analytical Chemistry* **51(11):** 1809-1814

Fischer, P. J., 1978. Oil and tar seeps, Santa Barbara basin, California, in: California Offshore Gas, Oil, and Tar seeps, California State Lands Commission, Sacramento, CA, p. 1-62

Fischer, P.J. and A.J. Stevenson, 1973. Natural hydrocarbon seeps, Santa Barbara basin, California, in Santa Barbara Channel Area revisited field trip guidebook, **Vol. 3**, edited by P.J. Fischer, pp. 17-28, Am. Assoc. Petrol Geol., Tulsa, Okla.

Galloway J., 1998. Chronology of petroleum exploration and development in the Santa Barbara Channel area, offshore southern California. *Structure and Petroleum Geology of Santa Barbara Channel, CA.* Pacific Section E.T.AAPG Miscellaneous Pub. **MP-46**, pp 1-12

Haines, M.A., and B.D. Johnson, 1995: Injected bubble populations in seawater and fresh water measured by a photographic method. *J. Geophys. Res.,* **100C4**, 7057-7068

Hanna, S.R., G.A. Briggs, and R.P. Hosker Jr., 1982. Handbook on Atmospheric Diffusion. ed. Jean Smith, Technical Information Center, U.S. Department of Energy. pp. 101

Hatzikiriakos, S.G. and P. Englezos. 1993. The relationship between global warming and methane gas hydraes in the earth. *Chem. Eng. Sci.* **48(23):** 3963-3969

Heeschen, K.U., A.M. Tréhu, R.W. Collier, E. Suess, G. Rehder. 2003. Distribution and height of methane bubble plumes on the Cascadia Margin characterized by acoustic imaging, *Geoophs. Res. Lett*., doi:10.1029/2003GL016974.

Hornafius, J. S, D. Quigley, and B. P. Luyendyk, 1999. The world’s most spectacular marine hydrocarbon seeps (Coal Oil Point, Santa Barbara Channel, California): Quantification of emissions, *J. Geophys. Res.*, **104:** 20703-20711

Hovland M., A.J. Judd, and R.A. Burke. 1993. The global flux of methane from shallow submarine sediments. Chemospheres **26:** 559-578

Hovland, M., 2002. On the self-sealing nature of marine seeps. *Continental Shelf Res.* **22(16):** 2387-2394

Hwang P.A., Y.-H.L., Hsu, and J. Wu, 1990: Air bubbles produced by breaking wind waves: A laboratory study.

Jähne, B., and P. Geiβler, 1994: An imaging optical technique for bubble measurements. "Sea Surface Sound '94. Proceedings of the III International Meeting on Natural Physical Processes Related to Sea Surface Sound," M. J. Buckingham and J.R. Potter, Eds., 290-303

Johnson, B.D., B.P. Boudreau, B.S. Gardiner, and R. Maass. 2002. Mechanical response of sediments to bubble growth. *Mar. Geol.* **187:** 347-363

Johnson, B.D. and R.C. Cooke. 1979. Bubble populations and spectra in coastal waters: A photographic approach. *J. Geophys. Res.*, **92C2**, 3761-3766

Katz M.E., D.K. Pak, G.R. Dickens, and K.G. Miller. 1999. The source and fate of massive carbon input during the latest Paleocene thermal maximum. *Science* **286**: 1531-1533

Kennett J.P., Cannariato K.G., Hendy I.L., Behl R.J., 2003. Methane hydrates in Quaternary climate change: The clathrate gun hypothesis. AGU Washington, Vol. **54**, 216 pp.

Kvenvolden KA, Reeburgh WS, Lorenson TD, 2001. Naturally occurring methane seepage—Workshop report. EOS **82:** 457

Kvenvolden, K.A., 1999. Potential effects of gas hydrate on human welfare. *Ann. Nat. Acad. Of Sci.*, **96(7)**, 3420-3426

La Montagne, G., I. Leifer, S. Bergmann, L.C. Van De Werfhorst, and P.A. Holden, 2004. Bacterial diversity in marine hydrocarbon-seep sediments. *Environ. Microbiol.* **6(8)**, 799-808

Leifer I., and R. Patro, 2002. The bubble mechanism for transport of methane from the shallow sea bed to the surface : A review and sensitivity study. *Cont. Shelf Res.* **22**, 2409-2428

Leifer I., Patro, R., and P. Bowyer, 2000b. A study on the temperature variation of rise velocity for large clean bubbles. *J. Atm. and Ocean. Tech.* **17(10)**, 1392-1402

Leifer, I., and I. MacDonald, 2003. Dynamics of the gas flux from shallow gas hydrate deposits: Interaction between oily hydrate bubbles and the oceanic environment. *Earth Plan. Sci. Lett.* **210(3/4)**, 411-424

Leifer, I., and J. Boles, 2005a. Measurement of marine hydrocarbon seep flow through fractured rock and unconsolidated sediment. *Marine Petroleum Geol.*, **22(4)**, 551-568

Leifer, I., and J. Boles, 2005b. Turbine seep-tent measurements of marine hydrocarbon seep forcing on sub-hourly time scales, *J. Geophys. Res* 110 C1, C01007, DOI 10.1029/2003JC002207.

Leifer, I., and J. Clark, 2002. Modeling trace gases in hydrocarbon seep bubbles. Application to marine hydrocarbon seeps in the Santa Barbara Channel, *Russian Geology and Geophysics* {Original - *Geologiya I Geofizika*} **43(7)**, 613-621

Leifer, I., G. De Leeuw, and L.H. Cohen, 2003b. Optical measurement of bubbles: System, design and application. *J. Atm. Ocean. Tech.* **20(9)**, 1317-1332

Leifer, I., G. De Leeuw, G. Kunz, and L. Cohen, 2003a. Calibrating optical bubble size by the displaced mass method. *Chem. Eng. Sci.* **58(23/24)**, 5211-5216

Leifer, I., J. Boles, J.F. Clark, and B.P. Luyendyk, 2004. The dynamic nature of marine hydrocarbon seepage. *Env. Geol.*, **46(8)**, 1038-1052

Leifer, I., J. Clark, and R. Chen, 2000a. Modifications of the local environment by a natural marine hydrocarbon seep, *Geophys. Res. Lett.* **27(22)**, 3711-3714

Leifer, I., J.F. Clark, and B. Luyendyk, 2005b. Seep blowouts and the transport of seep gas out of the deep sea to the atmosphere. *Global Biogeochemical Cycles*, (in progress).

Leifer, I.**,** T. Del Sontro, B. Luyendyk, and K. Broderick, 2005b. Time evolution of beach tar, oil slicks, and seeps in the Coal Oil Point seep field, Santa Barbara Channel, California. *Proc. Internat. Oil Spill Conf., May 15-19, 2005, Miami, FL*, EIS Digital Publishing, 14718A.

M.A.K. Khalil, R.A. Rasmussen, 1995. The changing composition of the Earth's atmosphere. In: H.B. Singh (Ed.), Composition, Chemistry, and Climate of the Atmosphere, Van Nostrand Reinhold, New York, pp. 50-97

McDougal, T.J., 1978, Bubble plumes in stratified environments. J .Fluid Mech. **4:** 655-672

Medwin, H., and N.D. Breitz, 1989: Ambient and transient bubble spectral densities in quiescent seas and under spilling breakers. *J. Geophys. Res.*, **94C**, 12,571-12,759

Mikolaj, P.G. and Ampaya, J.P. 1973. Tidal effects on the activity of natural submarine oil seeps. *Mar. Tech. Soc. J.* **7**: 25 - 28

Monahan, E.C., Q. Wang, X. Wang, and M.B. Wilson, 1994: Air entrainment by breaking waves: A laboratory assessment. "Proceedings of International Symposium Aeration Technology," R.E.A. Arndt and A. Prosperetti, Eds., *ASME NY,NY*, FED Vol **187:** 21-26

Patro R., Leifer I., Bowyer P. 2002. Better bubble process modeling: Improved bubble hydrodynamics parameterisation. In: *Gas Transfer and Water Surfaces*, Eds. M. Donelan, W. Drennan, E.S. Salzman, and R. Wanninkhof (pp. 315-320), AGU Monograph Volume 127.

Prather M, Derwent R, Ehhalt D, Fraser P, Sanhueza E, Zhou X. 1995. Other trace gases and atmospheric chemistry. In: Houghton JT, Meira Filho LG, Bruce J, Lee H, Callander BA, Haites E, Harris N, Maskell (eds) Climate change 1994: Radiative forcing of climate change and an evaluation of the IPCC IS92 emission scenarios. Cambridge University Press, Cambridge United Kingdom, pp 73–126

Quigley DC, Hornafius JS, Luyendyk BP, Francis RD, Clark J, Washburn L, 1999. Decrease in natural marine hydrocarbon seepage near Coal Oil Point, California, associated with offshore oil production. *Geol.*, **27**, 1047-1050

Rintoul, W., 1982. ARCO caps Santa Barbara Channel seep, Pac. Oil World **74:** 6-9

Rowland FS. 1985. Methane and chlorocarbons in the earth's atmosphere. *Origins of Life* **15:** 279-297

Sadhal S., Johnson, R.E., 1983. Stoke's flow past bubbles and drops partially coated with thin films. *Journal of Fluid Mechanics* **126:** 237-250

Sam A., C.O. Gomez, and J.A. Finch, 1996: Axial velocity profiles of single bubbles in water/froth. *Int. J. Min. Proc.* **47**: 177-196

Sander, R., 2000. Henry's Law Constants in NIST Chemistry WebBook, NIST Standard Reference Database, Number 69, Eds. W.G. Mallard and P.J. Linstrom, National Institute of Standards and Technology, Gaithersburg MD (http://webbook.nist.gov).

SBCAPCD, 2001. November 2001 Clean Air Plan, Santa Barbara County Air Pollution Control District.

Severinghaus, J.P., T. Sowers, E.J. Brook, R.B, Alley, M.L. Bender, 1998. Timing of abrupt climate change at the end of the Younger Dryas interval from thermally fractionated gases in polar ice. *Nature* **391:** 141-146, doi:10.1038/34346

Slauenwhite, D.E., Johnson, B.D., 1999. Bubble shattering: Differences in bubble formation in fresh water and seawater. *J. Geophys. Res.* **104:** 3265-3276

Thorpe, S.A., 1982: On the clouds of bubbles formed by breaking wind-waves in deep water and their role in air-sea gas transfer. *Phil. Trans. R. Soc. London*, **A304**: 155-210

Tsuge H., Hibino S., Nojima U. 1981. Volume of a bubble formed at a single submerged orifice in a flowing liquid. *Internat. Chem. Eng.*, **21:** 630-636

Vagle, S., and D.M. Farmer, 1998: A comparison of four methods for bubble size and void fraction measurements. *IEE J. Oceanic Engineering*, **23:** 211-222

Vigneault, C., B. Panneton, and G.S.V. Raghavan, 1992. Real time image digitization system for measurement of air bubbles. Cananadian Agricultural Engineering, **34:** 151-155

Walsh, A.L., and P.J. Mulhearn, 1987: Photographic measurements of bubble populations from breaking wind waves at sea. *J. Geophys. Res.* **92C13**, 14 553-14 565

Wang, Q., and E.C. Monahan, 1994: The influence of salinity on the spectra of bubbles formed in breaking wave simulations. Sea Surface Sound '94. Proceedings of the III International Meeting on Natural Physical Processes Related to Sea Surface Sound," M. J. Buckingham and J.R. Potter, Eds., 312-319

Wanninkhof, R., 1992. Relationship between wind speed and gas exchange over the ocean. *Journal of Geophysical Research* **97 C5:** 7373-7382

Washburn L Clark JF, Kyriakidis P, 2005. The spatial scales, distribution, and intensity of natural marine hydrocarbon seeps near Coal Oil Point, California. *J. Marine Petroleum Geology*, **22:** 569-578

Washburn L, Johnson L, Gotschalk CG, Egland ET, 2001. A gas-capture buoy for measuring bubbling gas flux in oceans and lakes. *J. Atmos. Ocean Tech.*, **18:** 1411-1420

Woolf, D.K., Thorpe, S.A.. 1991. Bubbles and the air-sea exchange of gases in near saturation conditions. Journal of Marine Research **49:** 435-466

The Department of the Interior Mission

MARCH 3, 1849

As the Nation's principal conservation agency, the Department of the Interior has responsibility for most of our nationally owned public lands and natural resources. This includes fostering sound use of our land and water resources; protecting our fish, wildlife, and biological diversity; preserving the environmental and cultural values of our national parks and historical places; and providing for the enjoyment of life through outdoor recreation. The Department assesses our energy and mineral resources and works to ensure that their development is in the best interests of all our people by encouraging stewardship and citizen participation in their care. The Department also has a major responsibility for American Indian reservation communities and for people who live in island territories under U.S. administration.

The Minerals Management Service Mission

As a bureau of the Department of the Interior, the Minerals Management Service's (MMS) primary responsibilities are to manage the mineral resources located on the Nation's Outer Continental Shelf (OCS), collect revenue from the Federal OCS and onshore Federal and Indian lands, and distribute those revenues.

Moreover, in working to meet its responsibilities, the **Offshore Minerals Management Program** administers the OCS competitive leasing program and oversees the safe and environmentally sound exploration and production of our Nation's offshore natural gas, oil and other mineral resources. The MMS **Royalty Management Program** meets its responsibilities by ensuring the efficient, timely and accurate collection and disbursement of revenue from mineral leasing and production due to Indian tribes and allottees, States and the U.S. Treasury.

The MMS strives to fulfill its responsibilities through the general guiding principles of: (1) being responsive to the public's concerns and interests by maintaining a dialogue with all potentially affected parties and (2) carrying out its programs with an emphasis on working to enhance the quality of life for all Americans by lending MMS assistance and expertise to economic development and environmental protection.